

Mechanistic Studies of Proton-Coupled Electron Transfer and Ligand
Substitution Reactions in Biologically Relevant Systems



Mechanistische Untersuchung von protonengekoppeltem
Elektronentransfer und den Substitutionsreaktionen biologisch
relevanter Systeme.

Der Naturwissenschaftlichen Fakultät der Friedrich-Alexander-Universität Erlangen-
Nürnberg zur Erlangung des Doktorgrades

vorgelegt von
David Sarauli
aus Tiflis, Georgien

Als Dissertation genehmigt von der naturwissenschaftlichen Fakultät der Friedrich-Alexander-Universität Erlangen-Nürnberg.

Tag der mündlichen Prüfung:	18.04.2008
Vorsitzender der Promotionskommission:	Prof. Dr. E. Bänsch
Erstberichterstatter:	Prof. Dr. Dr <i>h.c. mult.</i> Rudi van Eldik
Zweitberichterstatter:	Prof. Dr. Lutz Dahlenburg

„Wenn die Menschen nur über Dinge reden würden, von denen sie etwas verstehen - das Schweigen wäre bedrückend.“

Robert Lembke, deutscher Journalist (1913 – 1989)

Die vorliegende Arbeit entstand in der Zeit von Januar 2003 bis Januar 2008 am
Department Chemie und Pharmazie der Friedrich-Alexander-Universität Erlangen-
Nürnberg.

Danksagung

Prof. Dr. Dr. h.c. mult. Rudi van Eldik, der mir die Möglichkeit gegeben hat, in seiner Arbeitsgruppe die vorliegende Arbeit anzufertigen, danke ich für seine stets vorhandene Hilfsbereitschaft sowie die Sicherstellung meiner Finanzierung.

Für die Überlassung des herausfordernden und interessanten Themas, die zahlreichen wissenschaftlichen Anregungen, Ratschläge und Motivation, erstklassige Betreuung, ständige Hilfs- und Diskussionsbereitschaft, die maßgeblich zum Gelingen dieser Arbeit beitrugen, bedanke ich mich ganz herzlich bei Dr. Ivana Ivanović-Burmazović.

Prof. Dimitri E. Khoshtariya und Prof. Klaus Koch bin ich insbesondere zu Dank verpflichtet für die spannenden Diskussionen und hilfreiche Tipps. Dr. Tina D. Dolidze möchte ich für die Einführung in die Grundlagen der Elektrochemie danken.

Es wäre undenkbar, diese Arbeit ohne Hilfe und Kompetenz folgender Arbeitskollegen erfolgreich abzuschließen: Dr. Achim Zahl, Dr. Carlos Dücker-Benfer, Dr. Anton Neubrand, Dr. Roland Meier, Dr. Alicja Franke, Dr. Ralph Puchta, Ursula Niegratschka, Peter Illner, Katharina Dürr, Joachim Maigut, Sabine Rothbart, Stephanie Hochreuther, Anne Dees, Marie-Madeleine Walz, Gao-Feng Liu und Vesselina Popova sowie Herrn Uwe Reißer, Peter Igel und Manfred Weller für deren engagierten Einsatz bei apparativen Problemen. Danke!

An dieser Stelle gilt mein besonderer Dank den Bezugspersonen bzw. Freunden, die mein geistiges Gleichgewicht stetig stärken und mir immer zur Seite stehen: Dr. Nadine Summa, Dr. Hans Hanauer, Ariane Brausam, Hakan Ertürk, Natalya Hessenauer-Ilicheva und Christian Schickaneder.

Des Weiteren danke ich Olivia Lucia Brausam (Schönheit in Person) und Wolfgang Zwick (eine der beeindruckendsten Persönlichkeiten, die ich kennenlernen durfte).

Diesen persönlichen Erfolg verdanke ich größtenteils meiner Mutter, Doreta Sarauli, die mein ganzes Leben lang an mich glaubt, mich unterstützt und versteht, wie kein Anderer.

Der Deutschen Forschungsgemeinschaft danke ich für die finanzielle Unterstützung durch das *Graduiertenkolleg Homogener und Heterogener Elektronentransfer*.

Publications and Conference Contributions

Publications

1. **Sarauli, David**; Meier, Roland; Liu, Gao-Feng; Ivanović-Burmazović, Ivana; van Eldik, Rudi. *Effect of Pressure on Proton-Coupled Electron Transfer Reactions of Seven-Coordinate Iron Complexes in Aqueous Solutions*. *Inorganic Chemistry* (2005), 44(21), 7624-7633.
2. Khoshtariya, Dimitri E.; Dolidze, Tina D.; **Sarauli, David**; van Eldik, Rudi. *High-pressure probing of a changeover in the charge-transfer mechanism for intact cytochrome c at gold/self-assembled monolayer junctions*. *Angewandte Chemie, International Edition* (2006), 45(2), 277-281.
3. Khoshtariya, Dimitri E.; Dolidze, Tina D.; Seifert, Stefan; **Sarauli, David**; Lee, Geoffrey; van Eldik, Rudi. *Kinetic, thermodynamic, and mechanistic patterns for free (unbound) cytochrome c at Au/SAM junctions: impact of electronic coupling, hydrostatic pressure, and stabilizing/denaturing additives*. *Chemistry--A European Journal* (2006), 12(27), 7041-7056.
4. **Sarauli, David**; Popova, Vesselina; Zahl, Achim; Puchta, Ralph; Ivanović-Burmazović, Ivana. *Seven-Coordinate Iron Complex as a Ditopic Receptor for Lithium Salts: Study of Host-Guest Interactions and Substitution Behavior*. *Inorganic Chemistry* (2007), 46(19), 7848-7860.
5. **Sarauli, David**; van Eldik, Rudi; Ivanović-Burmazović, Ivana. *Evidence for Concerted Proton-Electron Transfer Mechanism in Seven-Coordinate Iron Superoxide Dismutase Mimetics*. *JACS* (2008), in preparation for submission.

Conference Contributions: Posters

1. *Electrochemical Studies on Seven-Coordinate 3d Metal Complexes*: 2004 Younger European Chemist's Conference, August 2004, Turin, Italy.
2. *Electrochemical Studies on Seven-Coordinate 3d Metal Complexes*: Inorganic Reaction Mechanism Group Meeting (IRMG-34), January 2005, Liverpool, UK.
3. *Studies of Proton-Coupled Electron Transfer and Secondary Interactions in Seven-Coordinate Iron Complexes*: International SFB Minisymposium "Redox-Active Metal Centres in Homogeneous and Heterogeneous Electron Transfer Systems", February 2005, Erlangen, Germany.
4. *Seven-Coordinate $[Fe(dapsox)(H_2O)_2]ClO_4$ Complex as a Receptor for Lithium Ions*: Inorganic Reaction Mechanism Group Meeting (IRMG-35), January 2006, Krakow, Poland.
5. *Seven-Coordinate Iron Complexes: Studies of Proton-Coupled Electron Transfer and Secondary Interactions with Lithium Salts*: International SFB Symposium "Redox-Active Metal Complexes-Control of Reactivity via Molecular Architecture", October 2006, Germany.

Conference Contributions: Oral Presentations

1. *Electrochemical Studies on Seven-Coordinate 3d Metal Complexes*: 2004 Younger European Chemist's Conference, August 2004, Turin, Italy.
2. *Studies of Proton-Coupled Electron Transfer and Secondary Interactions in Seven-Coordinate Iron Complexes*: International SFB Minisymposium "Redox-Active Metal Centres in Homogeneous and Heterogeneous Electron Transfer Systems", February 2005, Erlangen, Germany.

Contents

1. INTRODUCTION.....	11
1.1. SUPEROXIDE RADICAL.....	11
1.2. SUPEROXIDE DISMUTASES.....	12
1.2.1. Natural Enzymes.....	12
1.2.1.1. Proton-Coupled Electron Transfer.....	15
1.2.2. SOD Mimetics.....	16
1.3. GENERAL GOAL.....	19
2. PROTON-COUPLED ELECTRON TRANSFER REACTIONS OF SEVEN-COORDINATE IRON COMPLEXES IN AQUEOUS SOLUTIONS.....	20
2.1. EFFECT OF PRESSURE ON THERMODYNAMICS.....	20
2.1.1. General remark.....	20
2.1.2. Introduction.....	20
2.1.3. Experimental Section.....	24
2.1.3.1. Chemicals.....	24
2.1.3.2. Synthesis of Complexes.....	24
2.1.3.3. Spectrophotometric and potentiometric pH-titrations.....	26
2.1.3.4. Electrochemical Measurements.....	27
2.1.4. Results and Discussion.....	30
2.1.4.5. Determination of the pK_a values of the Fe complexes.....	30
2.1.4.6. Electrochemical behavior and pH dependence.....	37
2.1.4.7. Effect of Pressure on PCET.....	39
2.1.5. Conclusion.....	48
2.2. EVIDENCE FOR A CONCERTED PROTON-ELECTRON TRANSFER MECHANISM.....	50
2.2.1. General Remark.....	50
2.2.2. Introduction.....	50
2.2.3. Experimental Section.....	53
2.2.3.1. Chemicals.....	53
2.2.3.2. pH Potentiometric Titrations.....	53
2.2.3.3. Electrochemical Measurements.....	54

2.2.4.	Results.....	56
2.2.4.1.	Thermodynamics of Proton Transfer (PT) Reactions.....	56
2.2.4.2.	Effect of Temperature on Net Proton-Electron Transfer (PCET).....	58
2.2.4.3.	Effect of Temperature on Discrete Electron Transfer (ET) Steps.....	61
2.2.4.4.	Effect of Temperature on Kinetics of Net Proton-Electron Transfer (PCET) on the Electrode Surface.....	63
2.2.4.5.	Effect of Temperature on Kinetics of Discrete Electron Transfer (ET) Steps...	75
2.2.4.6.	Deuterium Kinetic Isotope Effect.....	77
2.2.5.	Overall Discussion.....	79
2.2.5.1.	AEFB Reaction Cycle: $1e^{-}2H^{+}$	81
2.2.5.2.	CEFD Reaction Cycle: $1e^{-}1H^{+}$	82
2.2.5.3.	EGF Reaction Cycle: $1e^{-}1H^{+}$	83
2.2.5.4.	Activation Parameters for $Fe^{II/III}$ dapsox and $Fe^{II/III}$ dapsc systems.....	83
2.2.6.	Conclusion.....	86

3. A SEVEN-COORDINATE IRON COMPLEX AS DITOPIC RECEPTOR FOR LITHIUM SALTS: STUDY OF HOST-GUEST INTERACTIONS AND SUBSTITUTION BEHAVIOR. 88

3.1.	GENERAL REMARK.....	88
3.2.	INTRODUCTION.....	88
3.3.	EXPERIMENTAL SECTION.....	91
3.3.1.	Materials.....	91
3.3.2.	Kinetic Measurements.....	91
3.3.3.	Spectrophotometric Titrations.....	92
3.3.4.	Electrochemical Measurements.....	92
3.3.5.	Nuclear Magnetic Resonance Spectrometry.....	94
3.3.6.	Quantum Chemical Methods.....	94
3.4.	RESULTS AND DISCUSSION.....	95
3.4.1.	Electrochemical Studies.....	95
3.4.2.	Solution Behavior in the Presence of $LiPF_6$	103
3.4.3.	7Li NMR Titrations.....	107
3.4.4.	Spectrophotometric Determination of K^{III}	112
3.4.5.	Reaction with SCN^{-} in CH_3CN	113
3.4.6.	Equilibrium Studies for Binding of SCN^{-}	119

3.4.7. Temperature-Dependent Kinetic Measurements	119
3.4.8. Lithium-Dependent Kinetic Measurements.....	122
3.4.9. Spectrophotometric Observations.....	123
3.4.10. DFT Calculations.....	127
3.5. CONCLUSION	129
4. SUMMARY	131
5. ZUSAMMENFASSUNG	136
6. REFERENCES	143

1. Introduction

1.1. Superoxide radical

Each time we breathe in oxygen, our body is transforming about 2 – 3% of it into free radicals, hence, in every cell, hundreds of thousands of free radicals are produced daily. The cell breathing occurs in mitochondria—the veritable powerhouses of the cell: most if not all oxygen metabolism takes place there. Taking oxygen-containing food and water and converting them into energy, mitochondria truly are the energy generating furnaces of our body. As such they are exposed to lots of oxygen. This burning of oxygen creates one of the most common free radicals: superoxide ($O_2^{\bullet-}$), a one-electron reduction product of dioxygen (O_2). Because 1 – 15% of the O_2 that is respired by mammals goes through this oxidation state, the biochemistry and reaction chemistry of superoxide are important to those processes concerned with oxygen toxicity, carcinogenesis, and aging.¹⁻³

Superoxide is one of the main causes of oxidative stress. Its role to act both as an oxidant and as a reductant gives rise to other dangerously reactive substances (Figure 1.1).¹⁻³ One of the mechanisms of biological toxicity of $O_2^{\bullet-}$ is based on its capacity to inactivate iron-sulfur clusters containing enzymes (which are critical in a wide variety of metabolic pathways), thereby liberating free iron into the cell, which can generate the highly reactive hydroxyl radical by reacting with hydrogen peroxide (H_2O_2).⁴ In its HO_2 form (hydroperoxyl radical, $pK_a=4.7$),¹ superoxide can also initiate lipid peroxidation of polyunsaturated fatty acids.⁵⁻⁷ It reacts with carbonyl compounds and halogenated carbons to create toxic peroxy radicals.⁸ Superoxide can react with nitric oxide (NO) to form a highly cytotoxic $ONOO^-$ species.⁹⁻¹¹ Severe neurological disorders such as Parkinson's^{12, 13} and Alzheimer's^{14, 15} diseases may as well be related to nerve cell damage caused by $O_2^{\bullet-}$. Additionally, some types of cancer are thought to arise from mutations induced by $O_2^{\bullet-}$ damage to DNA.^{16, 17} Therefore, an appropriate biochemical defense mechanism should be

developed to control the level of superoxide and its decomposition products, present under physiological conditions.

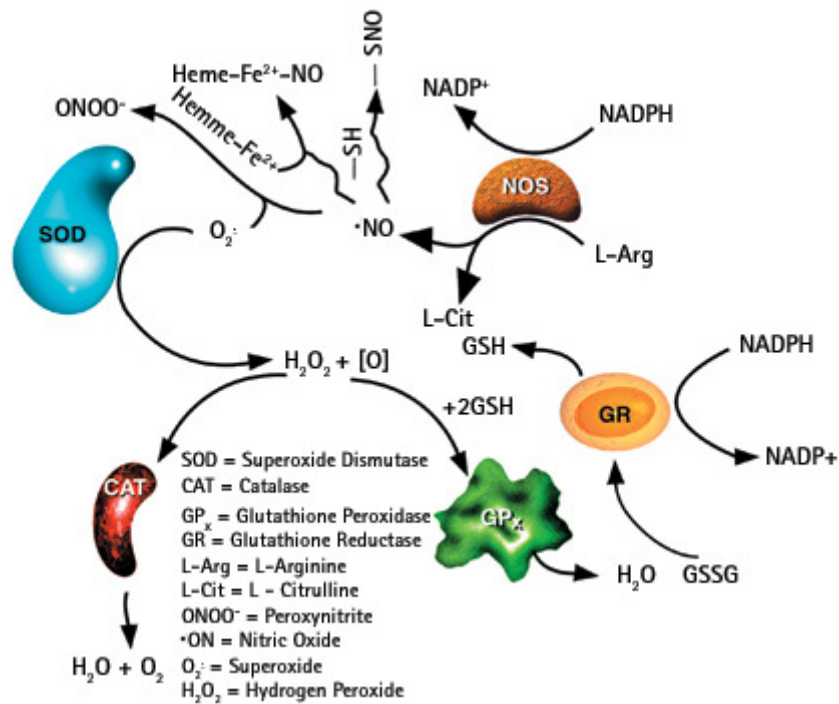


Figure 1.1. Chemical processes behind the oxidative stress.¹⁸

1.2. Superoxide Dismutases

1.2.1. Natural Enzymes

Organisms have evolved two known defenses for the detoxification of superoxide. In particular, two classes of enzymes have been identified whose function is the reduction and/or oxidation of superoxide: the superoxide dismutases (SODs) and the superoxide reductases (SORs).¹⁹⁻²⁴ The classical SODs disproportionate superoxide to hydrogen peroxide and dioxygen (Figure 1.2). In contrast, SORs selectively reduce superoxide to hydrogen peroxide in anaerobic organisms without the formation of dioxygen as a byproduct.

Bacterial SODs typically contain either nonheme iron or manganese at the active site (FeSOD or MnSOD) although copper–zinc (Cu, ZnSOD) and nickel (NiSOD) enzymes are also known.^{21, 25-28}

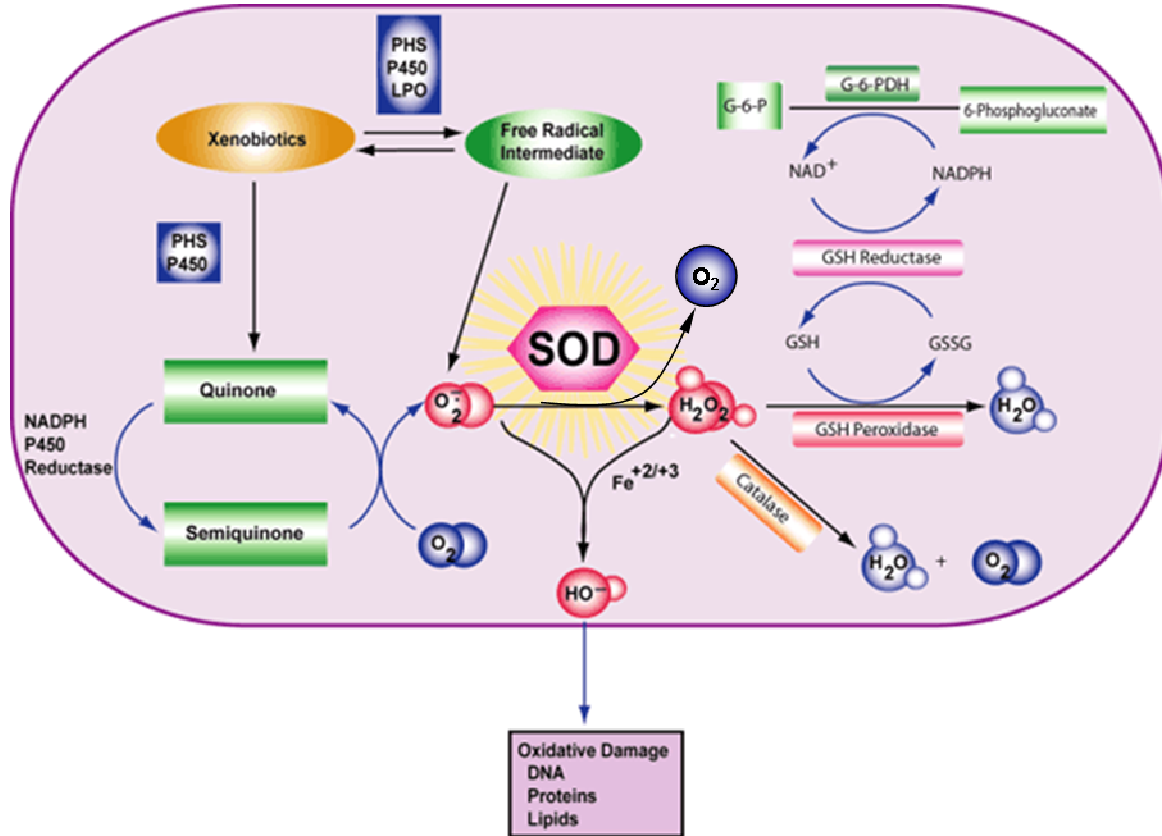


Figure 1.2. The biochemical pathway of superoxide dismutases.²⁹

FeSODs and MnSODs are homologous and catalyze the disproportionation of superoxide through a cyclic (pingpong) mechanism that involves $O_2^{\bullet-}$ oxidation at M^{III} followed by proton-induced $O_2^{\bullet-}$ reduction at M^{II} (eq 1.1).^{21, 25-27}



M stands for the metal ion, and the coordinated solvent molecule that normally couples proton transfer to electron transfer is in parentheses.

The active site of SOD is buried within the protein, containing a single Fe or Mn ion coordinated with distorted trigonal bipyramidal geometry, by two Histidins (His) and an Asparagin (Asp) in the equatorial plane, plus a third His and a coordinated solvent molecule $\text{H}_2\text{O}/\text{OH}^-$ ligand ($\text{pK}_a = 8.5$) in the axial positions (His73, His160, Asp156, and His26, Figure 1.3),²⁸ which makes it easier to control proton delivery. The structure of MnSODs is very similar.

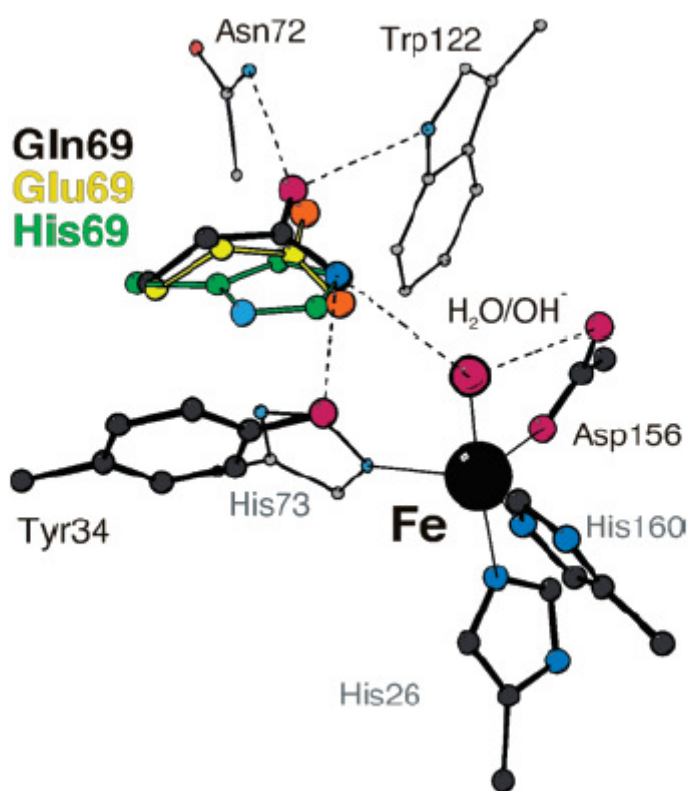


Figure 1.3. Diagram of the active site of FeSOD showing ligands to Fe and selected second sphere residues (taken from reference 28).

By poisoning the SOD redox potential half-way between the potentials at which superoxide is oxidized and reduced, the redox active metal center of SOD is able to both oxidize and reduce superoxide depending on the protonation states of the nearby residues and the oxidation state of the metal. The SOD catalytic cycle does not require an external source of electrons. The redox potential of the SOD $\text{Fe}^{\text{II}}/\text{Fe}^{\text{III}}$ couple is pH-dependent, and falls in the range from +0.03 to -0.31 V versus SCE (Standard Calomel Electrode).^{21, 30, 31} The redox potential of superoxide ($\text{O}_2^{\bullet-}$) highly

depends on pH, and it is significantly easier to reduce it under acidic conditions. At pH = 0, superoxide is reduced at a potential of +1.27 V versus SCE, whereas at pH = 7.5 and pH = 14, it is reduced at +0.83 and -0.041 V, respectively. Protons are used to raise the redox potential of superoxide by stabilizing H₂O₂ as a reduction product.

The binding of cations to the metal center of the enzyme can possibly affect the SOD structure, properties and its activity. It was reported, for example, that the binding of Ca^{II} had no effect on the enzyme activity, but caused a conformational effect with a change of symmetry on the metal-binding site.³² It has recently become apparent that cation- π interactions are in general important for molecular recognition and stabilization in many biological systems, as well as in SODs.³³ Furthermore, the modeling of supramolecular mimics for the active sites of different superoxide dismutases has been the topic of a recent report.³⁴ It was demonstrated that the mimic with a guanidyl cation could exhibit a potent SOD activity. This cation was located in the effective range around the metal center, being crucial for attracting the superoxide anion to and seize it from the active metal.³⁴ Such a kind of binding can also be responsible for the change in redox potential of the enzyme.

1.2.1.1. Proton-Coupled Electron Transfer

As it can be seen from eq 1.1, two protons must be supplied to a substrate to generate a product. Electron transfer to the superoxide ion is unfavorable because O₂^{•-} is already negatively charged and the resulting peroxide anion (O₂²⁻) is very unstable, so protonation is most likely to be a pre- or co-requisite for reduction of O₂^{•-}.³⁵ Transfer of the second proton has been proposed to be the rate-limiting step, and the second proton may aid in product dissociation by displacing the bound product from the metal ion in an inner-sphere mechanism.³⁶ FeSOD has been shown to take up one proton upon reduction throughout the pH range of activity (eq 1.1a).³⁶ The redox-coupled proton is therefore re-released upon metal ion oxidation (eq 1.1b) and becomes available locally as the substrate becomes reduced. Thus, reduction of the substrate can be thought of as proton-coupled electron transfer.^{37, 38}

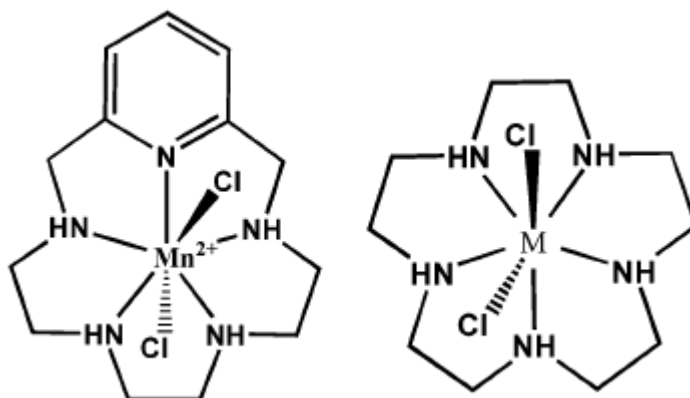
For the MnSOD it has been shown that the enzyme takes up a proton upon reduction, which provides support for the prevalent assumption that key features of MnSOD's mechanism are the same as those for FeSOD.^{21, 35}

In general, electron and proton transfer processes are essential in most enzymatic catalysis (see also [Sections 2.1.2](#) and [2.2.2](#)).^{38, 39} The question whether they take place in a concerted way or as individual processes has promoted great theoretical and experimental interest.^{40, 41} Proton-coupled electron transfer pathways are suggested for fast electron transfer in biological systems, as in the case of photosystem II.⁴² Very recently Carrasco et al. reported results of the theoretical study on a simple enzyme model to contribute to the elucidation of the reaction mechanism of iron and manganese SODs.⁴³ They could emphasize the presence of a coupled transfer process where two protons and one electron are involved, and were able to hypothesize that concerted proton-electron transfer occurs.⁴³ But still, the overall mechanism is still not completely clarified up to date.

1.2.2. SOD Mimetics

The natural SODs were proven to be therapeutically applicable in preclinical as well as clinical trials for the treatment of disease states connected with superoxide overproduction, although they suffer as drug candidates primarily from immunogenic response.⁴⁴⁻⁴⁷ In light of the clinical data surrounding the use of SOD enzymes, their low molecular weight mimetics have been proposed for the treatment of a great variety of diseases.⁴⁷ SOD mimetics could have distinct advantages over the natural enzymes as pharmaceutical agents, including the ability to access intercellular space, the lack of immunogenicity, a longer half-life in the blood, potential for oral delivery, and a lower cost of goods. There are a wide range of therapeutic applications for SOD mimetics considering the multitude of deleterious effects known to derive from oxidative stress induced by an excess of superoxide (Figure 1.1).⁴⁷

For a few years, seven-coordinate 3d metal complex species in solution were shown to exhibit interesting chemical properties and catalytic activity.⁴⁵⁻⁵⁰ It was found that they are able to catalyze the disproportionation of $O_2^{\bullet-}$ to H_2O_2 and O_2 even faster than natural enzymes.⁴⁸ The best SOD mimetics known to date are seven-coordinate Mn(II) complexes with macrocyclic pentadentate ligands, pyridine derivatives of pentaazacyclopentadecane [15]aneN₅ (Scheme 1.1).^{45, 47, 48}

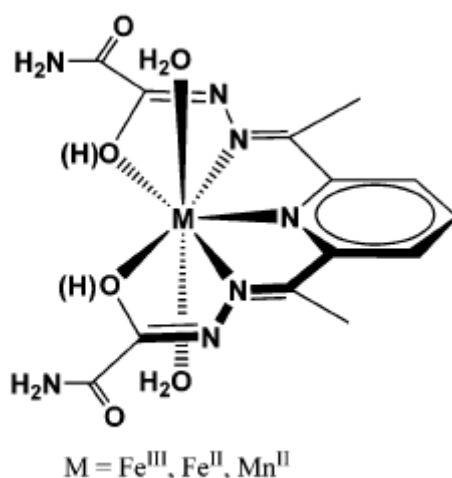


Scheme 1.1.

Iron-containing SOD mimetics would be also desirable because of their higher kinetic and thermodynamic stability compared to manganese complexes.⁴⁷ However, the Fe^{III} complexes with [15]aneN₅-type macrocycles have low pK_a values for the coordinated water molecules⁵⁰ forming inactive dihydroxo species, and have a tendency to react with hydrogen peroxide, which are serious drawbacks in their catalytic activity under physiological conditions.⁴⁷ In general, it has been postulated that only seven-coordinate complexes of macrocyclic ligands with prominent conformational flexibility could possess SOD activity.^{48, 51}

Another type of Fe and Mn seven-coordinate complexes was designed, synthesized and is being mechanistically investigated in our group. These are complexes of acyclic and rigid pentadentate H₂dapsox [H₂dapsox=2,6-diacetylpyridine-bis(semioxamide)]^{52, 53} that have several important features regarding their potential SOD activity (Scheme 1.2).⁵² It was demonstrated that such complexes,

despite of the above mentioned postulation, are able to catalyze the fast disproportionation of superoxide.⁵²



Scheme 1.2.

A lower cost of materials (more economic syntheses) is the first advantage of these complexes compared to the complexes of macrocyclic ligands in terms of their potential application as drugs. Further important features of the Fe^{II/III}dapsox systems as SOD mimetics are: a) the higher pK_a values for the coordinated water molecules, and b) a variable number of protons exchanged during the redox reactions in a wide pH range (Section 2.1).^{54, 55} Because of this feature it was possible to study mechanistically multiple proton-coupled electron transfer reactions. In Section 2.1 of this dissertation the effect of pressure on thermodynamics of such reactions is established and reported. Section 2.2 presents results of detailed studies of different reaction steps in a wide pH range to contribute to the elucidation of the mechanism of elementary redox processes. Since the protons play a crucial role in the overall native SOD activity and the mechanism of the overall disproportionation reaction is still not established, the possibility to find out how the elementary processes within SOD catalytic cycle mimetics occur is of great importance. Furthermore, in Section 3, it is demonstrated that our seven-coordinate [Fe(dapsox)(H₂O)₂]₄ClO₄⁵³ complex behaves also as a ditopic receptor for lithium salts in acetonitrile. The simulation of

an enzymatic active site, which can bind small metal cations and in that way enhance the binding of superoxide, would be of importance (see [Section 1.2.1](#)).

1.3. General Goal

Since the treatment of oxidative stress through decomposition of superoxide by metal-based SOD mimetics as human pharmaceuticals started to be a widely used concept, elucidation of basic reactions of SOD active complexes, such as ligand substitution (see [Section 3](#)) and the electron transfer reactions (see [Section 2](#)), is of vast importance. Deep understanding of chemical processes behind the physiological effects enables the prediction of possible side effects of their application as drugs and the estimation whether and how their utilization can lead to beneficial effects.

2. Proton-Coupled Electron Transfer Reactions of Seven-Coordinate Iron Complexes in Aqueous Solutions

2.1. Effect of Pressure on Thermodynamics

2.1.1. General remark

The work presented below has been published as a full paper⁵⁴:

Sarauli, D.; Meier, R.; Liu, G.-F.; Ivanović-Burmazović, I.; van Eldik, R. *Inorganic Chemistry* **2005**, *44*, 7624-7633.

2.1.2. Introduction

Investigations on proton-coupled electron transfer (PCET) processes and the understanding of the fundamental aspects involved are of current interest since PCET reactions play an important role in many biological redox processes.^{37, 56-60} An interesting example of biologically relevant PCET reactions is the disproportionation of superoxide to hydrogen peroxide and dioxygen by Fe- and Mn-superoxide dismutases (SODs).^{35, 36} Disproportionation of $O_2^{\bullet-}$ requires uptake of two protons, in which the second proton assists product (H_2O_2) dissociation from the metal center. This one-electron–two-proton transfer process seems to be a particularly desirable feature of the redox active center for it to be an efficient SOD catalyst (Section 1.2.1.1).

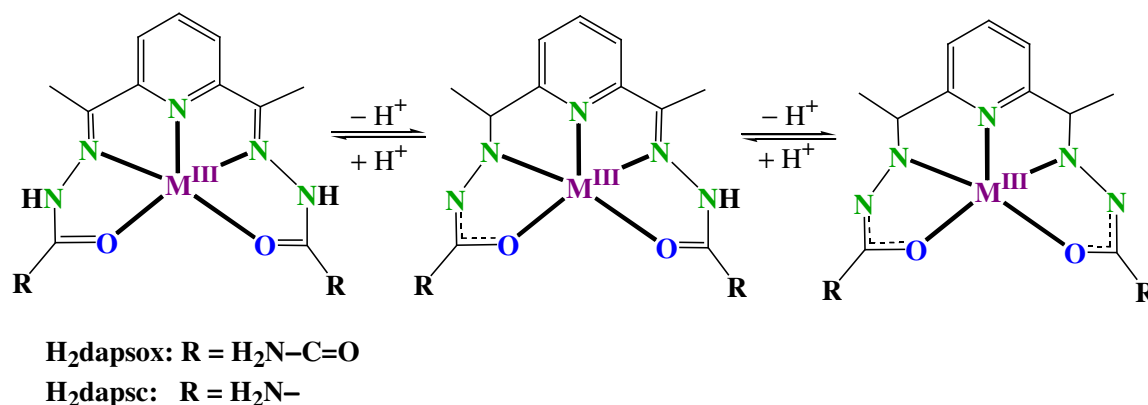
Riley et al.⁵⁰ have shown that seven-coordinate Fe^{III} diaqua complexes with pentaaza macrocyclic ligands possess SOD activity and could be used as SOD functional mimics. In these systems, the aqua-hydroxo form of the complex is responsible for the high catalytic activity. However, at physiological pH, the catalytically inactive dihydroxo form of the pentaaza complex is also present in solution ($pK_{a1} = 3.5-5.1$, $pK_{a2} = 7.3-7.7$).⁵⁰ Thus, it would be desirable to have seven-coordinate Fe^{III}

complexes with higher pK_a values for the coordinated water molecules to yield higher catalytic activity under physiological conditions. At the same time, because the assignment of species involved in a proton transfer that assists superoxide disproportionation is extremely difficult in the case of enzymatic systems, investigations on adequate model complexes could be of importance.

Modulation of the iron redox potential by deprotonation of the potentially heptadentate N-tripodal ligands has been examined.^{61, 62} It has also been reported that, in these systems, the protonation state controls the spin state of the iron center.⁶¹ However, all these studies involve complexes with a six-coordinate octahedral structure that does not change upon ligand deprotonation. The influence of the ligand protonation state on the geometry, coordination number, and electronic and magnetic properties of seven-coordinate pentagonal-bipyramidal complexes of planar pentadentate ligands has already been established.⁶³ Since seven-coordinate pentagonal-bipyramidal iron complexes with planar pentadentate ligand are interesting as potential SOD mimetics, the study of multiple proton transfer processes coupled to redox reactions in such systems is of significant importance. In the seven-coordinate SOD mimetics studied so far, the possibility for a proton-transfer process in which the pentadentate ligand is involved does not exist.

As shown below, the seven-coordinate Fe^{III} complexes of 2,6-diacetylpyridine-bis(acylhydrazone) chelates used in the present study enable such investigations of PCET processes in aqueous solution. These ligands can coordinate to the Fe^{III} centre in the neutral, mono- and dianionic form without changing their coordination mode (Scheme 2.1), and their acidity can be varied by changing the $-R$ groups. The presence of additional carbonyl groups in $H_2dapsox$ enables the isolation of the Fe^{III} complex from aqueous solution in the $[Fe(dapsox)(H_2O)_2]^+$ form with a doubly deprotonated chelate,⁵³ whereas in the case of H_2dapsc the isolated $[Fe(H_2dapsc)Cl_2]^+$ complex has the neutral pentadentate in the equatorial plane.^{64, 65}

Because of the presence of the dianionic pentadentate in the $[\text{Fe}(\text{dapsox})(\text{H}_2\text{O})_2]^+$ complex, the $\text{p}K_{\text{a}}$ values of the coordinated water molecules are higher ($\text{p}K_{\text{a}1} = 5.78$,



Scheme 2.1

$\text{p}K_{\text{a}2} = 9.45$)⁵⁵ than in the case of the above-mentioned Fe^{III} SOD mimetics with pentaaza macrocyclic ligands. Therefore, the highly reactive aqua-hydroxo form is the major species in solution at physiological pH.

The two structurally similar pentagonal-bipyramidal $\text{Fe}^{\text{III/II}}$ redox systems studied here have been shown to be good models to elucidate PCET processes. This is because the number of protons exchanged during the redox reaction varies along the studied pH range. Both complexes exhibit four acid–base equilibria in the pH range 1–12. The corresponding equilibrium constants have been estimated independently by spectrophotometric, potentiometric, and electrochemical titration methods. The number of protons exchanged during the electrode reactions was evaluated from the slopes of appropriate $E_{1/2}$ –pH plots ($E_{1/2}$ = half-wave potential).

To provide an insight into the fundamental aspects of PCET reactions, the effect of pressure on the thermodynamics of the electrode reactions was investigated in detail. The effect of pressure P on a thermodynamic equilibrium constant K^0 is related to the overall reaction volume, ΔV^0 , which can be expressed in terms of the pressure dependence of the potential of the half-cell reaction (conventionally written as a reduction process) relative to a particular reference half-cell:

$$\Delta V^0 = -nF(\partial\Delta E^0/\partial P)_T \quad (2.1)$$

where n is the number of moles of electrons transferred and F is the Faraday constant.⁶⁶ The measurement of E^0 (identical with $E_{1/2}$ as a first approximation) with electrochemical methods such as cyclic voltammetry (CV) or differential pulse voltammetry as a function of pressure leads to a ΔV^0 value for the reaction under the selected experimental conditions. The volume change associated with the reduction of the metal complex, $\Delta V^0_{\text{complex}}$, consists of the following contributions: a) intrinsic volume changes ΔV^0_{intr} , reflecting bond length and conformational changes in the structure of the complex and b) electrostrictive volume changes ΔV^0_{elec} , reflecting the contraction or expansion of the surrounding solvent in response to the change in charge on the complex.⁶⁷ Electrostriction plays an important role in the electron-transfer process. According to the Drude-Nernst expressions,⁶⁸ the electrostrictive reaction volume should depend on $\Delta z^2/r$ ($\Delta z^2 =$ is the difference in the square of the charge, r is the effective complex ion radius⁶⁹⁻⁷¹). However, it has been observed for a number of studied systems that ΔV^0_{elec} depends linearly on Δz^2 rather than on $\Delta z^2/r$.⁶⁹⁻⁷³ This is a consequence of the fact that the difference in complex radii between different complexes is less important than the change in Δz^2 .

Tregloan et al.⁷² studied the reduction of differently charged Fe^{III} complexes, which do not show any pH dependent behavior in aqueous solution. They found a very good correlation between the reaction volume and the difference between the squares of the charges on the oxidized and reduced forms of the complexes, namely,

$$\Delta V^0_{\text{elec}} = 4.3\Delta z^2 \quad (2.2)$$

where $\Delta z^2 = z^2_{\text{oxidized}} - z^2_{\text{reduced}}$. Some recent studies on binuclear Ru^{III}-Fe^{II}⁷³ and Co^{III}-Fe^{II}⁷⁴ complexes showed that this correlation is very useful in the case of pure electron-transfer reactions.

A similar dependence on Δz^2 was reported for the neutralization reaction volume of a series of differently charged complexes in aqueous solution.⁷⁵ A linear relationship between ΔV^0 and Δz^2 for 19 neutralization reactions of the type (eq 2.3)



[M = Co^{III}, Rh^{III}, Fe^{III}, or Pt^{IV}; A = H₂O, NH₃ and C₂O₄H; and B = OH, NH₂ and C₂O₄] was found to be

$$\Delta V^0 = (14.5 \pm 0.8) - (2.5 \pm 0.2)\Delta z^2 \quad (2.4)$$

where $\Delta z^2 = (z-1)^2 - z^2$.

The goal of our study was to find a correlation between the reaction volume ΔV^0 and the change in overall charge Δz^2 for the reduction of seven-coordinate Fe^{III} complexes that is coupled to the transfer of different numbers of protons. This report presents, for the first time, results from the study of pressure effects on electron-transfer reactions of metal complexes that are coupled to proton-transfer processes. It will be shown that the measured reaction volume can also be expressed as a linear function of the change in the square of the overall charge on the metal complexes during PCET processes.

2.1.3. Experimental Section

2.1.3.1. Chemicals

All reagents and solvents were commercially available (Sigma, Acros Organics, Fluka) and used without further purification. Deionized Millipore water was used for all types of measurements. Freshly distilled solvents were used for all syntheses described below.

2.1.3.2. Synthesis of Complexes

[Fe^{II}(H₂dapsox)(H₂O)₂](ClO₄)₂. 2,6-diacetylpyridine (0.163g, 1 mmol) and semioxamid (0.218 g, 2.1 mmol) were heated in a 2:1 mixture of

methanol/acetonitrile (60 mL) up to 65 °C and refluxed for 2 h under an argon atmosphere. After this period, $\text{Fe}(\text{ClO}_4)_2 \cdot 4\text{H}_2\text{O}$ (0.35 g, 1 mmol) was carefully added to the resulting white suspension under an argon atmosphere. The color of the suspension changed to gray, and the white precipitate dissolved slowly with time. After 5 h of refluxing, a part of the solvent mixture was removed under reduced pressure. The dark gray solution was filtered and placed in the refrigerator. A dark gray powder was collected after 2 days. Anal. Calcd for $\text{C}_{13}\text{H}_{19}\text{Cl}_2\text{FeN}_7\text{O}_{10}$: C, 27.88; H, 3.42; N, 17.51%. Found: C, 27.56; H, 3.39; N, 17.62%

A solution of the iron(III) counterpart $\{[\text{Fe}^{\text{III}}(\text{dapsox})(\text{H}_2\text{O})_2]\text{ClO}_4\}$ adjusted to pH = 2 was reduced by potentiostatically controlled electrolysis, and the spectrum of the product was identical with that of a solution of the synthesized $[\text{Fe}^{\text{II}}(\text{H}_2\text{dapsox})(\text{H}_2\text{O})_2](\text{ClO}_4)_2$ recorded at pH = 2 (Figure 2.1).

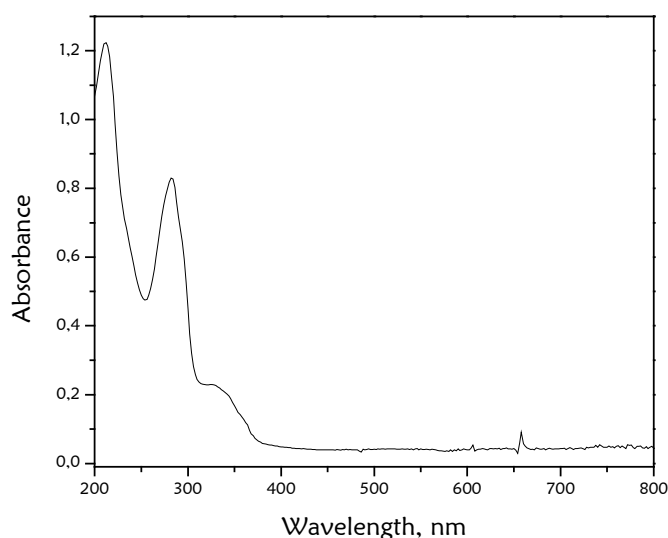


Figure 2.1. UV/vis spectrum of the synthesized $\text{Fe}^{\text{II}}(\text{H}_2\text{dapsox})(\text{H}_2\text{O})_2$. Conditions: $[\text{Fe}^{\text{II}}(\text{H}_2\text{dapsox})(\text{H}_2\text{O})_2]^{2+} = 5 \times 10^{-5} \text{ M}$, pH 2.0, $T = 298 \text{ K}$.

$[\text{Fe}^{\text{III}}(\text{dapsox})(\text{H}_2\text{O})_2]\text{ClO}_4$. The complex was prepared and characterized as described previously.⁵³

[Fe^{III}(H₂dapsc)Cl₂]Cl·2H₂O and [Fe^{II}(H₂dapsc)(H₂O)Cl]Cl. The complexes were prepared following the procedure of Palenik et al.⁶⁴

2.1.3.3. Spectrophotometric and potentiometric pH-titrations

The pH of the solutions was measured with a Mettler Delta 350 pH meter using a combined glass electrode. The latter was calibrated applying standard buffer solutions (pH = 4, 7 and 10) and 0.1 M HCl (pH = 1). The pH-electrode was filled with NaCl instead of KCl to prevent precipitation of KClO₄. The pH-dependent spectrophotometric titrations of [Fe(H₂dapsox)(H₂O)₂](ClO₄)₂, [Fe(H₂dapsc)Cl₂]Cl and [Fe(H₂dapsc)(H₂O)Cl]Cl were carried out with a Hewlett-Packard 8452A spectrophotometer. The complex solutions were prepared using 0.1 M Britton-Robinson⁷⁶ buffer solutions (pH = 2–12). In the range below pH = 2, no buffer solutions were used. The pH of the solutions was changed by addition of HClO₄ or NaOH. The complex concentrations during these experiments were 5 × 10⁻⁵ M and the ionic strength was kept constant at *I* = 0.1 M (NaClO₄). Measurements were performed under a nitrogen atmosphere. The calculation of the equilibrium constants (pK_a values) and the resulting pH-dependent speciation was performed with the software package Specfit/32 global analysis.

Potentiometric titrations of [Fe(dapsox)(H₂O)₂]ClO₄, [Fe(H₂dapsox)(H₂O)₂](ClO₄)₂, [Fe(H₂dapsc)Cl₂]Cl, and [Fe(H₂dapsc)(H₂O)Cl]Cl were performed on a METROHM 702 SM Titrino in a jacketed, airtight glass titration cell equipped with a combined pH glass electrode (METROHM), a N₂ inlet and outlet, and a graduated 20 ml microburet (METROHM). The electrode was calibrated with strong acid and a strong base so that a direct reading in hydrogen ion concentration would be made using four different commercially available standard buffer solutions of pH = 2, 4, 7, and 10. The ion product of water, that is, pK_w = -log [H⁺][OH⁻] = 13.75, was determined experimentally. Carbonate-free 0.05 M sodium hydroxide or perchloric acid solutions were prepared with boiled, distilled, and nitrogen-saturated water and were standardized by titrations with 0.05 M potassium hydrogen phthalate solution. Gran's method^{77, 78} was used to confirm the absence of carbonate in the sodium

hydroxide standard solution (carbonate content 0.13 %). All solutions were adjusted to an ionic strength of 0.1 M with NaClO_4 . The temperature was maintained at 25.0 ± 0.1 °C by circulating thermostated water through the outer jacket of the cell. All measurements were carried out under a constant atmosphere of nitrogen above the solution and were repeated at least four times. The concentration of the complexes was 1×10^{-3} M, and the ionic strength was kept constant at 0.1 M by NaClO_4 . The $\text{p}K_a$ values and species distribution of the complexes were calculated using the program TITFIT.⁷⁹

2.1.3.4. Electrochemical Measurements

Cyclovoltammetric measurements were carried out with an Autolab PGSTAT 30 device (Eco Chemie). A conventional three-electrode arrangement was employed consisting of a gold disk working electrode (geometric area: 0.07 cm^2) (Metrohm), a platinum wire auxiliary electrode (Metrohm), and a Ag/AgCl, NaCl (3 M) (Metrohm) reference electrode. The measurements in aqueous solutions were done in 0.1 M NaClO_4 supporting electrolyte. All solutions were initially thoroughly degassed with prepurified nitrogen (15 min), and a stream of N_2 gas was passed over the sample solutions during the measurements. The solutions were thermostated at 25 °C. The proton stoichiometry of the individual $\text{Fe}^{\text{III/II}}-\text{L}$ electrode reactions was evaluated from the slopes of $E_{1/2}-\text{pH}$ diagrams according to the Nernst equation.⁸⁰ The redox potentials reported in the text refer to an Ag/AgCl/3M NaCl reference electrode (+0.214 V vs. NHE, 25 °C). A modified 0.1 M Britton–Robinson buffer [mixture of acetic acid/acetate, PIPES = piperazine-N,N'-bis(2-ethanesulfonic acid), and boric acid/borate] had to be used to reach optimal buffering in the pH range 3.5–12. This buffer was applied to evaluate the pH-dependence of the cyclovoltammetrically measured $E_{1/2}$ values. No buffer was used for the evaluation of the pH-dependent $E_{1/2}$ at $\text{pH} < 3.5$. The $\text{p}K_a$ values were calculated using the program EFIT.⁸¹

Electrochemical measurements under elevated pressure were performed in a homemade cell (Figure 2.2). A three electrode system was employed. It consisted of

a gold working disk electrode (geometric area: 0.02 cm²) (BAS), a platinum wire (Sigma-Aldrich) as an auxiliary electrode, and an Ag/AgCl reference electrode. The reference electrode was prepared as follows: the Ag wire covered with AgCl was placed in a shrink tube (BAS) filled with 4 M NaCl solution and closed carefully with porous Vycor (BAS). The set of electrodes was placed into the Teflon cup, which was screwed into the electrochemical cell body. The cell was filled with a solution made up of 0.1 M NaClO₄ electrolyte and 1 mM complex. Nitrogen was bubbled through the solution for at least 25 min to ensure that oxygen had been removed. Then, the Teflon cup was closed with a Teflon plug and a screw (Figure 2.2). The assembled pressure vessel containing the cell was placed in a thermostated water-jacket (Figure 2.2), and a period of 45 min was given to reach thermal equilibrium (25.0 ± 0.1 °C) of the cell after assembly and after each change in pressure.



Figure 2.2. Left: the set of electrodes and Teflon cell body; right: the whole high-pressure electrochemical cell.

The pH values of solutions were controlled using perchloric acid, NaOH and different buffer systems (MES, Collidine, CAPS). The buffer systems were selected in such a way that the effect of pressure on the pK_a values are known to be very small.⁸² In the case of the $[\text{Fe}^{\text{III}}(\text{dapsox})(\text{H}_2\text{O})_2]^+ / [\text{Fe}^{\text{II}}(\text{Hdapsox})(\text{H}_2\text{O})_2]^+$ and $[\text{Fe}^{\text{III}}(\text{H}_2\text{dapsc})(\text{H}_2\text{O})(\text{OH})]^{2+} / [\text{Fe}^{\text{II}}(\text{H}_2\text{dapsc})(\text{H}_2\text{O})_2]^{2+}$ redox couples (see later Tables 2.2 and 2.3), measurements were performed at pH 5.1 in MES buffer to prevent the

use of acetate/acetic acid buffers, which show a significant pressure dependence of their pK_a value.

Scan rates were optimized for each system so as to obtain reversible (quasi-reversible) behavior with peak separation ΔE (difference between anodic and cathodic peaks) of around 60–80 mV. The peak separations (ΔE) as well as the half-wave potentials ($E_{1/2}$) were determined from the original CV current peak positions and compared with those simulated by GPES software.⁸³ An excellent agreement between these values was found. The pressure runs were carried out in an ascending and descending pressure cycle, and each measurement was repeated at least three times.

To prove the validity of our data, high-pressure test measurements on the $[\text{Co}(\text{en})_3]\text{Cl}_3$ complex were performed and the value of ΔV^0 was compared with reported data in the literature.⁸⁴ The dependence of the half-wave potential on pressure is shown in Figure 2.3. The value of the reaction volume was found to be $\Delta V^0 = 26.2 \pm 1.6 \text{ cm}^3 \text{ mol}^{-1}$, which is in excellent agreement with $\Delta V^0 = 26.7 \pm 0.7 \text{ cm}^3 \text{ mol}^{-1}$ reported by Fu and Swaddle.⁸⁴

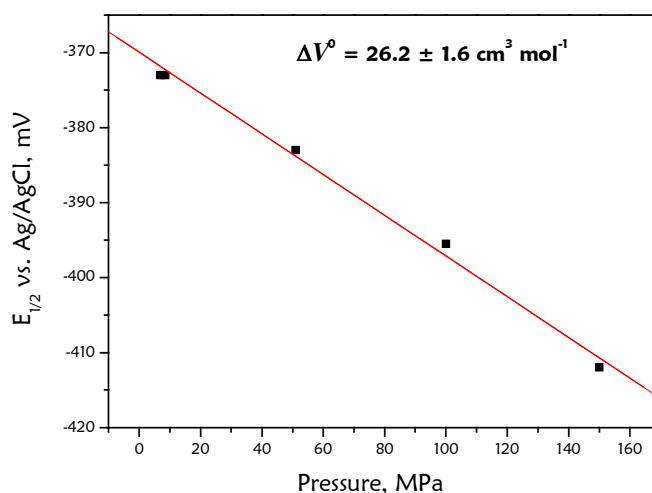


Figure 2.3. Dependence of the half-wave potential on pressure for 0.002 M $[\text{Co}(\text{en})_3]\text{Cl}_3$ in 0.5 M NaCl, together with free en (0.2 M).

2.1.4. Results and Discussion

2.1.4.5. Determination of the pK_a values of the Fe complexes

The seven-coordinate iron complexes investigated in this study have the pentadentate 2,6-diacetylpyridine-bis(acylhydrazone) ligands coordinated to the metal center in the equatorial plane and two water molecules in the apical positions.^{53, 64, 65} Since these ligands can be coordinated to the iron center in neutral, mono-, or dianionic forms (Scheme 2.1) and the two coordinated water molecules can also be deprotonated, a total of four protons can be neutralized upon titration in the pH range 1–12.

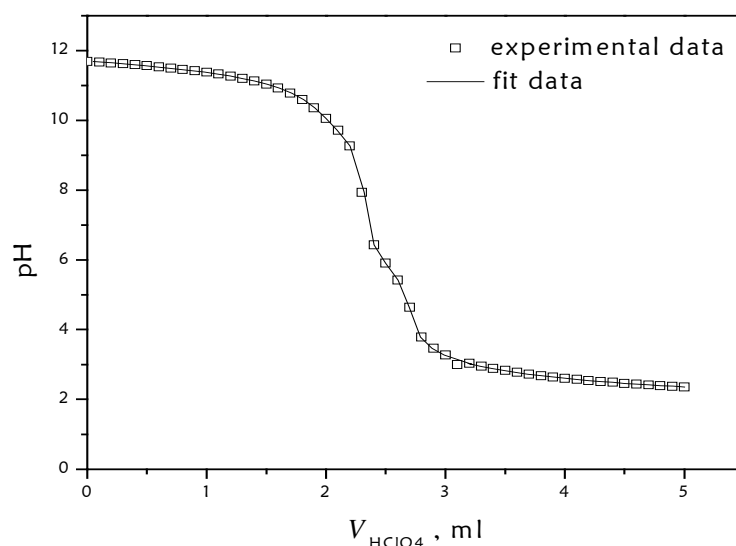


Figure 2.4. Potentiometric titration curve. Experimental conditions: $[\text{Fe}^{\text{III}}\text{dapsox}] = 1 \text{ mM}$, $T = 298 \text{ K}$, $I = 0.1\text{M NaClO}_4$.

In the case of the $\text{Fe}^{\text{III}}\text{dapsox}$ system, the pK_a values of the two coordinated water molecules were spectrophotometrically determined to be $pK_{a1}^{\text{water}} = 5.78$ and $pK_{a2}^{\text{water}} = 9.45$.⁵⁵ Identical pK_a^{water} values were also found by potentiometric titrations, carried out in the present study in both directions (by adding acid or base). Potentiometric titrations allowed the determination of two additional pK_a values, $pK_{a1}^{\text{ligand}} = 1.6$ and $pK_{a2}^{\text{ligand}} = 2.4$, which correspond to the first and second

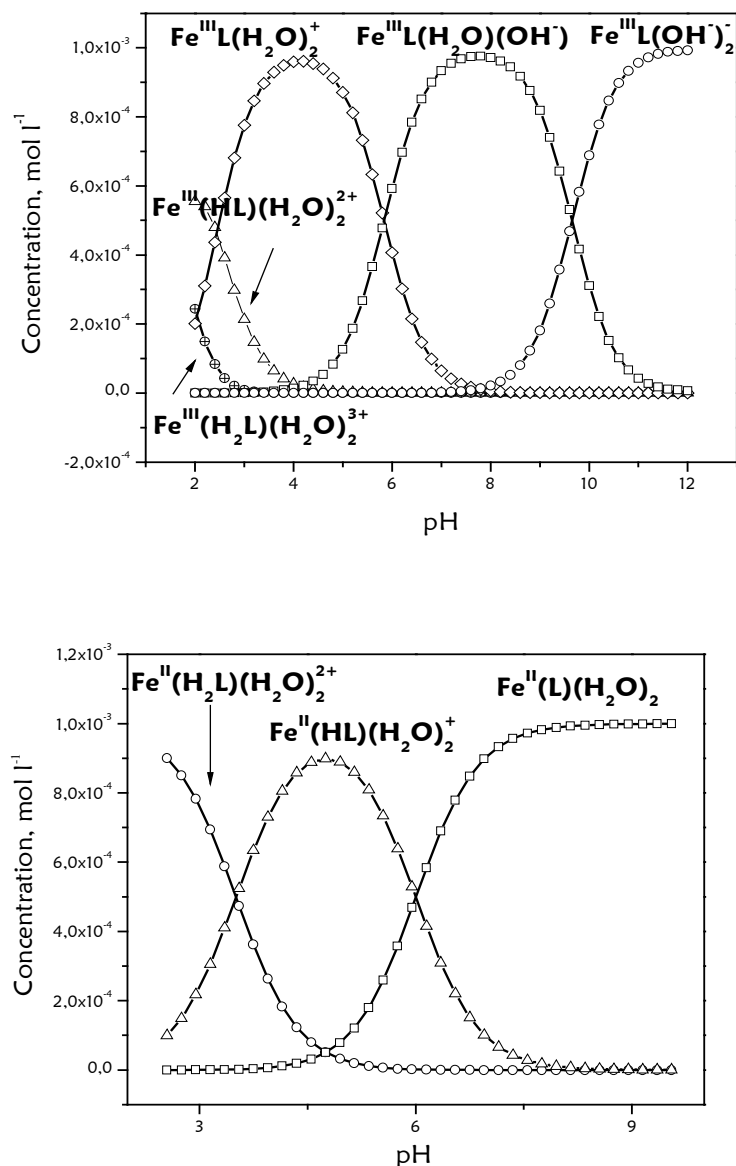


Figure 2.5. Calculated species distribution plots for Fe^{III}dapsox (above) and Fe^{II}dapsox (below). Experimental conditions: [Fe^{III/II}dapsox] = 1 mM, *T* = 298 K, *I* = 0.1M NaClO₄.

The Fe(dapsox) complexes,^{64, 65} however, show different acid–base properties. In the case of the H₂dapsox pentadentate, the Fe^{III} complex crystallizes with two coordinated Cl⁻ anions in apical positions, whereas the Fe^{II} complex crystallizes with one Cl⁻ and one water molecule coordinated to the metal center. However, in aqueous solutions, both complexes are present in the diaqua form. Solutions of the complexes were treated with silver triflate and filtered to remove the AgCl precipitate. After this treatment, solutions were investigated spectrophotometrically.

The determined pK_a values were compared with those obtained from a titration of the initial complex solutions and the values were found to be identical.

Spectra recorded on changing the pH from 1 to 13 as well as spectra of five different species present in aqueous solution of $\text{Fe}^{\text{III}}\text{dapsc}$ (calculated using Specfit/32 global analysis software) are summarized in Figure 2.6.

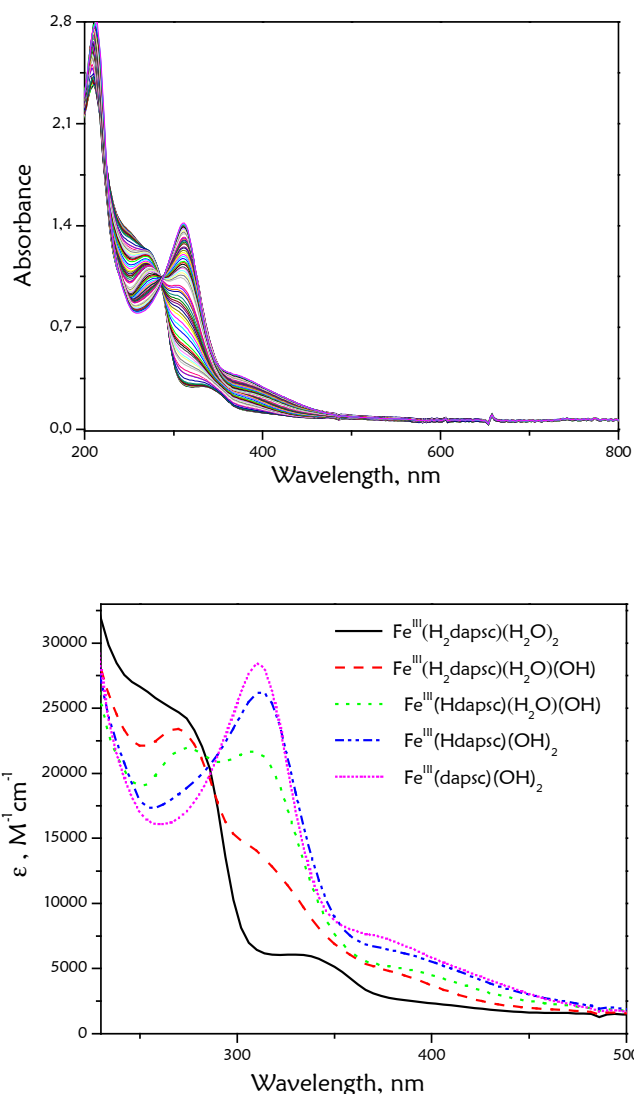
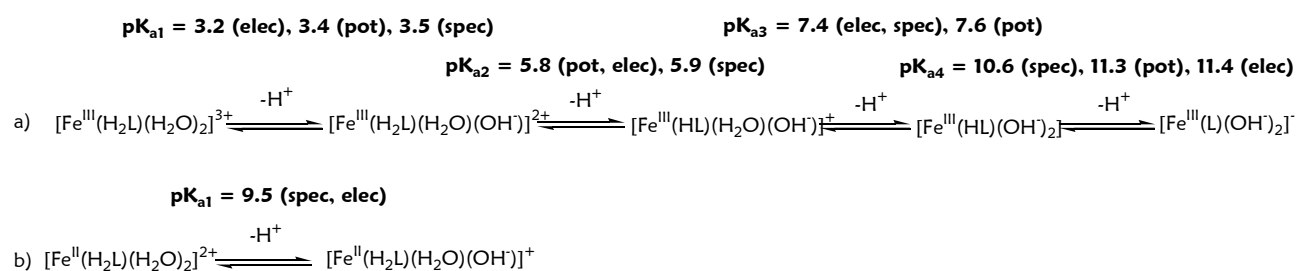


Figure 2.6. Spectrophotometric titration: UV/vis spectra of $\text{Fe}^{\text{III}}\text{dapsc}$ at different pH values from pH 1 to 13. Above: the overall spectral changes; below: spectra of all different complex species. Experimental conditions: $[\text{Fe}^{\text{III}}\text{dapsc}] = 5 \times 10^{-5} \text{ M}$, $T = 298 \text{ K}$, $I = 0.1 \text{ M NaClO}_4$.

From the analysis of the pH dependent UV/vis spectra, four pK_a values were found. The pK_a values determined from potentiometric titrations are in good agreement with the spectrophotometric data. The results are summarized in Scheme 2.3, showing all deprotonation steps and corresponding pK_a values. Only the spectrophotometrically determined pK_{a4} value deviates significantly from the other values because of relatively small spectral changes that accompany the last deprotonation step. The corresponding species distribution diagram is shown in Figure 2.7.



Scheme 2.3. L = dapsc.

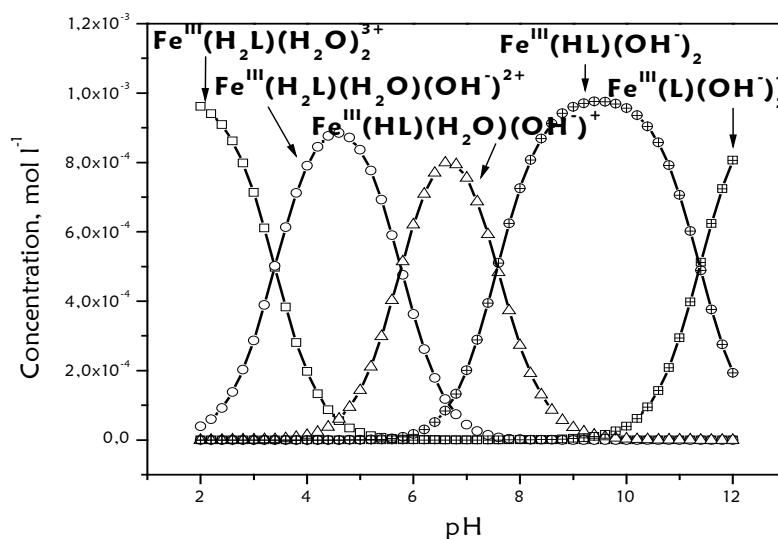


Figure 2.7. Calculated species distribution for $\text{Fe}^{\text{III}}\text{dapsc}$. Experimental conditions: $[\text{Fe}^{\text{III}}\text{dapsc}] = 1 \text{ mM}$, $T = 298 \text{ K}$, $I = 0.1 \text{ M NaClO}_4$.

The coordinated H_2dapsc pentadentate is less acidic than H_2dapsox , which has two adjacent carbonyl groups. Thus, the first $\text{p}K_{\text{a}1}$ of $\text{Fe}^{\text{III}}\text{dapsc}$ is assigned to the deprotonation of one water ligand. The $\text{p}K_{\text{a}1}$ of $\text{Fe}(\text{H}_2\text{O})_6^{3+}$ is 2.2.⁸⁵ Taking into consideration the effect of three nitrogen and two oxygen donors coordinated to the Fe^{3+} center, a somewhat higher $\text{p}K_{\text{a}}$ value for the deprotonation of a coordinated water molecule is expected (Scheme 2.3a). As reported later, the formation of a μ -oxo dimer can be observed during the electrochemical titration between pH 3 and 5. This supports the deprotonation of the coordinated water molecule in this pH range.

The second $\text{p}K_{\text{a}2}$ for $\text{Fe}^{\text{III}}\text{dapsc}$ can be assigned to the first deprotonation step of the chelate. It is known that the analogous Cr^{III} complex with pentadentate dapsc can be isolated with a singly deprotonated form of the ligand at $\text{pH} > 3$.⁶⁵ Taking into account that the $[\text{Fe}^{\text{III}}(\text{H}_2\text{dapsc})(\text{H}_2\text{O})(\text{OH})]^{2+}$ species has a lower charge than $[\text{Cr}^{\text{III}}(\text{H}_2\text{dapsc})(\text{H}_2\text{O})_2]^{3+}$, it is reasonable to expect a higher $\text{p}K_{\text{a}}$ value for the first deprotonation step of the chelate in the case of the Fe^{III} complex (Scheme 2.3a).

The next $\text{p}K_{\text{a}3}$, calculated to be 7.6, represents the deprotonation of the second coordinated water molecule, and since $[\text{Fe}^{\text{III}}(\text{Hdapsc})(\text{H}_2\text{O})(\text{OH})]^+$ has a positive charge, this $\text{p}K_{\text{a}}$ value is lower than the corresponding $\text{p}K_{\text{a}2}^{\text{water}}$ of the neutral $[\text{Fe}^{\text{III}}(\text{dapsox})(\text{H}_2\text{O})(\text{OH})]$ species. Thus, the $\text{p}K_{\text{a}4} = 11.3$ is assigned to the second deprotonation step of the chelate.

$\text{Fe}^{\text{II}}(\text{H}_2\text{dapsc})$ was titrated spectrophotometrically in the range $5 \leq \text{pH} \leq 12$. At $\text{pH} < 5$, no spectral changes could be detected (Figure 2.8). Analysis of the spectra led to the determination of only one $\text{p}K_{\text{a}}$ value, assigned to the deprotonation of a water molecule coordinated to the Fe^{II} center ($\text{p}K_{\text{a}}^{\text{II}} = 9.5$). The change in absorbance upon titration at 304 nm, where the largest change in absorbance was observed, is also shown in Figure 2.8. The obtained $\text{p}K_{\text{a}}$ value is identical to $\text{p}K_{\text{a}}^{\text{II}}$ for $\text{Fe}(\text{H}_2\text{O})_6^{2+}$.⁶⁵ This suggests that the electronic nature of the Fe^{II} center remains unchanged upon coordination of the neutral H_2dapsc pentadentate and that the

axially coordinated water molecules are not affected by the $(N)_3(O)_2$ donor set in the equatorial plane.

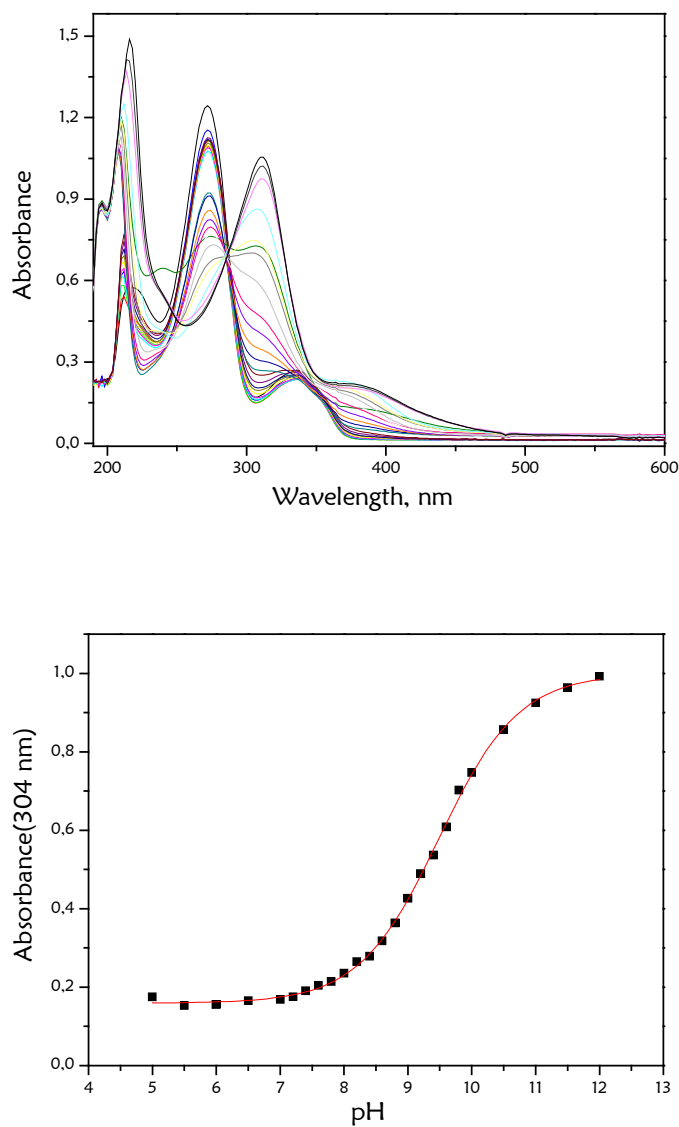


Figure 2.8. Spectrophotometric titration: UV/vis spectra of $Fe^{II}dapsC$ at different pH values from pH 5 to 12. Above: the overall spectral changes; below: change in absorbance at $\lambda = 310$ nm as a function of pH. Experimental conditions: $[Fe^{II}dapsC] = 5 \times 10^{-5}$ M, $T = 298$ K, $I = 0.1$ M $NaClO_4$.

2.1.4.6. Electrochemical behavior and pH dependence

The Fe^{III/II}dapsox couple shows reversible electrochemical behavior with $E_{1/2} = +0.216$ V vs. NHE (Normal Hydrogen Electrode) and $\Delta E_p = 60$ mV at pH 4.4. Fe^{III/II}dapsc exhibits analogous reversible behavior. CVs for both complexes at certain pH values are given in Figure 2.9.

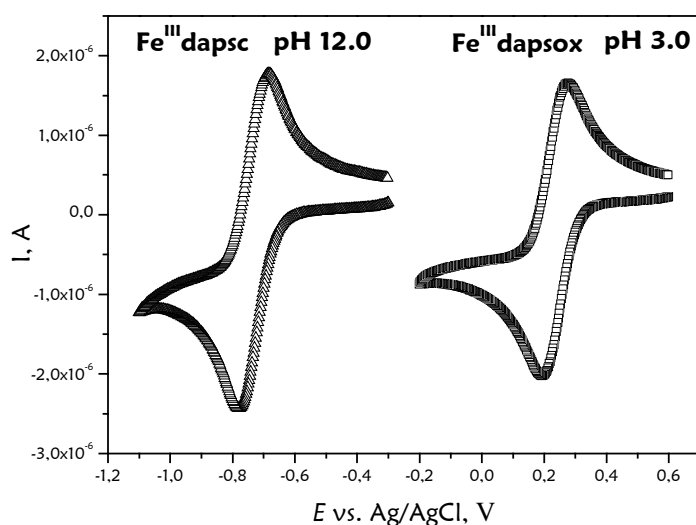


Figure 2.9. Cyclic voltammograms of Fe^{III/II}dapsox (squares, pH 3) and Fe^{III/II}dapsc (triangles, pH 12); Experimental conditions: [complex] = 1 mM, scan rate – 50 mV/s, $T = 298$ K, $I = 0.1$ M NaClO₄.

To determine the number of protons involved in PCET, a detailed study of the pH-dependent redox potentials was performed. The $E_{1/2}$ values of both Fe complexes strongly depend on pH, showing a gradual negative shift in the reduction potential for the Fe^{III/II} couple with increasing pH. When the pH is higher than 10, the voltammograms become quasi-reversible with $\Delta E > 90$ mV. By fitting the pH-dependent redox potential curve using the software EFIT, the pK_a values of both oxidation states of Fe(dapsox) as well as Fe(dapsc) were determined. Furthermore, from the slopes of the titration curves, the number of protons, which are taken upon one-electron reduction in the different pH ranges, can be calculated from the Nernst equation.⁸⁰

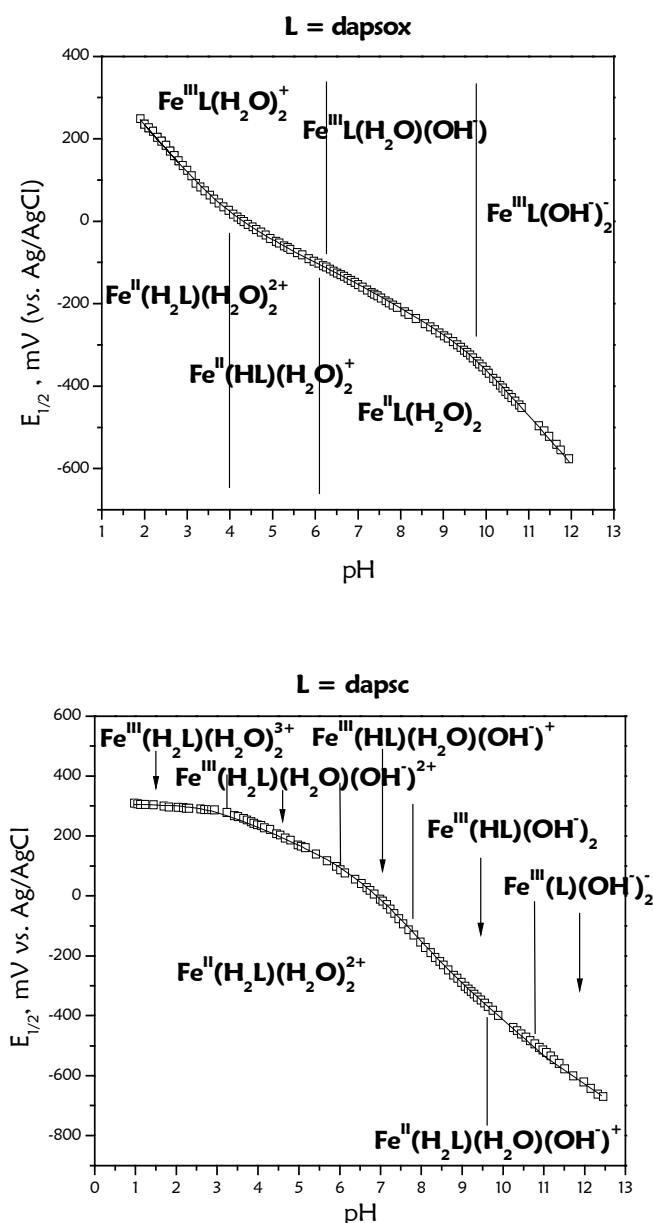


Figure 2.10. pH-dependent redox potential diagrams for the $\text{Fe}^{\text{III/II}}\text{dapsox}$ (above) and $\text{Fe}^{\text{III/II}}\text{dapsc}$ (below) systems. Experimental conditions: $[\text{complexes}] = 1 \times 10^{-3} \text{ M}$, scan rate = 50 mV/s , $T = 298 \text{ K}$, and $I = 0.1 \text{ M NaClO}_4$. The solid lines represent fit-data (EFIT).

The pK_a values for $\text{Fe}^{\text{III}}\text{dapsox}$ and $\text{Fe}^{\text{II}}\text{dapsox}$ estimated from the electrochemical measurements are in good agreement with those calculated from potentiometric and spectrophotometric titration data. The assignment of the Fe^{III} and Fe^{II} species (Scheme 2.2) is also in agreement with the number of protons transferred upon reduction in the particular pH range (Figure 2.10). At $\text{pH} < 4$ and $\text{pH} > 10$, a “two-

proton–one-electron transfer” occurs, whereas between pH 4 and 10 a “one-proton–one-electron transfer” occurs.

In the case of the Fe^{III}dapsc complex, at low pH, the redox potential is independent of [H⁺]; that is, the complex reduction proceeds without proton transfer. Going to higher pH, dimer formation was observed in the cyclic voltammogram between pH 3 and 5, with two characteristic reductions at $E_{\text{red1}} = +0.25 \text{ V}$ and $E_{\text{red2}} = 0 \text{ V}$ (vs. Ag/AgCl at pH = 3.5). At pH > 5, the second reduction peak disappears. This fact proves our assumption that the first $\text{p}K_{\text{a1}}^{\text{III}} = 3.4$ refers to the deprotonation of a coordinated water molecule. The $\text{p}K_{\text{a}}$ values of Fe^{III}dapsc and Fe^{II}dapsc, which result from the pH-dependent cyclic voltammetric measurements ($\text{p}K_{\text{a1}}^{\text{III}} = 3.2$, $\text{p}K_{\text{a2}}^{\text{III}} = 5.8$, $\text{p}K_{\text{a3}}^{\text{III}} = 7.4$, $\text{p}K_{\text{a4}}^{\text{III}} = 11.4$, $\text{p}K_{\text{a1}}^{\text{II}} = 9.5$; Figure 2.10) are similar to those obtained from other titrations. The corresponding acid-base equilibria of Fe^{III}dapsc and Fe^{II}dapsc (Scheme 2.3) account for the number of protons transferred upon reduction in different pH ranges (Figure 2.10). It should be noted that within the pH range 7.5–9.5, three protons are taken upon reduction, which was not observed in the case of the Fe(dapsox) system.

2.1.4.7. Effect of Pressure on PCET

On the basis of the spectrophotometric, potentiometric, and electrochemical studies, and the generated species distribution curves, pH values for the high-pressure cyclic voltammetric measurements were selected in a way that the different protonated forms of the Fe(dapsox) and Fe(dapsc) systems were present in solution as the predominant species. The shifts in the half-wave potentials ($E_{1/2}$) with pressure were followed for all the different protonated forms of Fe(dapsox) and Fe(dapsc). The values of $E_{1/2}$ and the peak separation ΔE for all systems as a function of pressure are reported in Tables 2.1 and 2.2. Pressure dependence of the half-wave potentials is illustrated for the $[\text{Fe}^{\text{III}}(\text{dapsox})(\text{H}_2\text{O})_2]^+ / [\text{Fe}^{\text{II}}(\text{Hdapsox})(\text{H}_2\text{O})_2]^+$ and $[\text{Fe}^{\text{III}}(\text{dapsc})(\text{OH})_2]^- / [\text{Fe}^{\text{II}}(\text{H}_2\text{dapsc})(\text{H}_2\text{O})(\text{OH})]^+$ couples, which show the highest and lowest values of the corresponding ΔV_{cell}^0 , respectively, in Figure 2.11.

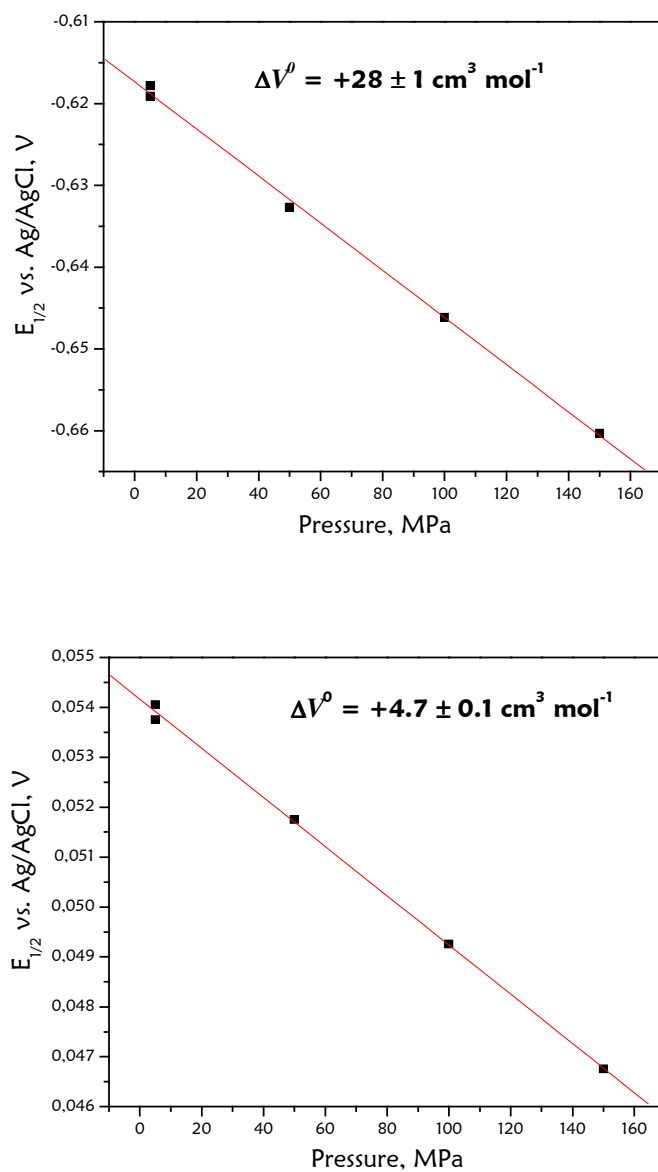


Figure 2.11. Pressure dependences of the half-wave potentials for $[\text{Fe}^{\text{III}}(\text{dapsc})(\text{OH})_2]^- / [\text{Fe}^{\text{II}}(\text{H}_2\text{dapsc})(\text{H}_2\text{O})(\text{OH})]^+$ at pH 12 (above) and $[\text{Fe}^{\text{III}}(\text{dapsox})(\text{H}_2\text{O})_2]^+ / [\text{Fe}^{\text{II}}(\text{Hdapsox})(\text{H}_2\text{O})_2]^+$ at pH 5.1 (below). Scan rate = 50 mV/s, $T = 298 \text{ K}$, $I = 0.1 \text{ M}$ (NaClO_4).

Table 2.1. Studied Fe^{III}dapsox complex: pH values at which measurements were done, applied pressures, values of the half-wave potentials at each pressure and the peak separations.

Complex	pH	Pressure, MPa	$E_{1/2}$, V vs. Ag/AgCl	ΔE , mV
Fe ^{III} dapsox	2.9	5	0.1253	75
		50	0.1213	77
		100	0.1176	80
		150	0.1136	83
		5	0.1250	76
	5.1	5	0.0537	76
		50	0.05175	78
		100	0.04925	81
		150	0.04675	85
		5	0.054	75
	7.0	5	-0.1569	74
		50	-0.1604	77
		100	-0.1639	81
		150	-0.1684	86
		5	-0.1566	75
	11.0	5	-0.4747	95
		50	-0.4877	98
		100	-0.4997	101
		150	-0.5107	104
		5	-0.4761	94

Table 2.2. Studied Fe^{III}dapsc complex: pH values at which measurements were done, applied pressures, values of the half-wave potentials at each pressure and the peak separations.

Complex	pH	Pressure, MPa	$E_{1/2}$, V vs. Ag/AgCl	ΔE , mV
Fe ^{III} dapsc	2.0	5	0.3	68
		50	0.2942	64
		100	0.2885	69
		150	0.2837	69
		5	0.2995	68
	5.0	5	0.175	66
		50	0.171	68
		100	0.167	71
		150	0.162	75
		5	0.1753	65
	6.6	5	0.0403	64
		50	0.0364	67
		100	0.032	71
		150	0.0289	76
		5	0.0399	65
	8.5	5	-0.2284	75
		50	-0.2332	78
		100	-0.2392	81
		150	-0.2462	84
		5	-0.2279	74
10.4	10	-0.4569	95	
	50	-0.4626	98	
	100	-0.4684	101	
	150	-0.4742	104	
	5	-0.4567	94	
12.0	5	-0.6178	105	
	50	-0.6327	108	
	100	-0.64615	111	
	150	-0.6603	114	
	5	-0.6191	104	

The investigated reactions are all of the type



and the values of ΔV_{cell}^0 , calculated according to (2.1), can be considered to consist of

$$\begin{aligned} \Delta V_{\text{cell}}^0 &= \Delta V_{\text{ref}}^0 + \Delta V_{\text{PCET}}^0 = \Delta V_{\text{ref}}^0 + \Delta V_{\text{complex}}^0 - nV_{\text{H}^+}^0 \\ &= \Delta V_{\text{ref}}^0 + (\Delta V_{\text{elec}}^0 + \Delta V_{\text{intr}}^0)_{\text{complex}} - nV_{\text{H}^+}^0 \end{aligned} \quad (2.6)$$

where ΔV_{ref}^0 is the half-cell contribution for a Ag/AgCl reference electrode, ΔV_{elec}^0 is the electrostrictive volume change on the complex, ΔV_{intr}^0 is the intrinsic volume change on the complex, $V_{\text{H}^+}^0$ is the partial molar volume of the proton as a reactant, and n is the number of protons transferred.

The half-cell reaction volume for the Ag/AgCl reference electrode was determined by Sun et al.⁸⁶ and reported to be $\Delta V_{\text{ref}}^0 = -9.0 \pm 1.0 \text{ cm}^3 \text{ mol}^{-1}$. As mentioned above, ΔV_{intr}^0 arises from changes in bond lengths and angles upon reduction, whereas ΔV_{elec}^0 depends strongly on changes in charge. With the application of eq. 2.2, eq. 2.6 can be expressed as

$$\Delta V_{\text{complex}}^0 = \Delta V_{\text{cell}}^0 - \Delta V_{\text{ref}}^0 + nV_{\text{H}^+}^0 = \Delta V_{\text{intr}}^0 + k \Delta z_{\text{overall}}^2 \quad (2.7)$$

where k is an empirical parameter. In the present case, $\Delta z_{\text{overall}}^2$ for reaction 2.5 results not only from the change in the oxidation state of the metal center, but also from changes in the overall charge as a result of the different number of protons involved in the reduction process.

The partial molar volume of the proton, $V_{\text{H}^+}^0$, was estimated by various methods in the past (in water at 25 °C), as reported by Millero.⁸⁷ The average values for $V_{\text{H}^+}^0$ were found to be $-4.2 \pm 1.5 \text{ cm}^3 \text{ mol}^{-1}$ and $-4.7 \pm 1.1 \text{ cm}^3 \text{ mol}^{-1}$.⁸⁷ In another study,⁷⁵ the reaction volumes of 19 different neutralization reactions (eq 2.3) were

determined. On combining eq 2.3 with the dissociation of a water molecule, whose reaction volume is $-22.2 \pm 0.2 \text{ cm}^3 \text{ mol}^{-1}$,^{82, 88} it can be converted to a protonation reaction, namely,



Combination of eq 2.4 with the given volume for the dissociation of water, results in the following expression for eq 2.8.

$$\Delta V^0 = \Delta V_{\text{elec}}^0 - V_{\text{H}^+}^0 = (2.5 \pm 0.2)\Delta z^2 + (7.7 \pm 0.8) \quad (2.9)$$

Thus, the experimental value for $V_{\text{H}^+}^0$ that results from the 19 studied neutralization reactions, is $-7.7 \pm 0.8 \text{ cm}^3 \text{ mol}^{-1}$, which is in agreement with the value reported by Stokes and Robinson.⁸⁹

Table 2.3. Fe(dapsox): species in aqueous solution before and after electrochemical reduction, number of protons transferred upon reduction, the difference in the square of the charge, pH values at which measurements were done, measured reaction volumes and $\Delta V_{\text{complex}}^0 = \Delta V_{\text{cell}}^0 - \Delta V_{\text{Ag/AgCl}}^0 + nV_{\text{H}^+}^0$.

Species	number of protons, n	$\Delta z^2_{\text{overall}}$	pH	$\Delta V_{\text{cell}}^0, \text{ cm}^3 \text{ mol}^{-1}$	$\Delta V_{\text{complex}}^0, \text{ cm}^3 \text{ mol}^{-1}$
	2	-3	2.9	$+7.7 \pm 0.2$	$+1 \pm 2$
	1	0	5.1	$+4.7 \pm 0.1$	$+6 \pm 2$
	1	0	8.0	$+7.6 \pm 0.2$	$+9 \pm 2$
	2	1	11.0	$+23.8 \pm 0.3$	$+17 \pm 2$

Table 2.4. Fe(dapsc): Species in aqueous solution before and after electrochemical reduction, number of protons transferred upon reduction, the difference in the square of the charge, pH values at which measurements were done, measured reaction volumes and $\Delta V^0_{\text{complex}} = \Delta V^0_{\text{cell}} - \Delta V^0_{\text{Ag/AgCl}} + nV^0_{\text{H}^+}$.

Species	number of protons, n	$\Delta z^2_{\text{overall}}$	pH	$\Delta V^0_{\text{cell}}, \text{cm}^3 \text{mol}^{-1}$	$\Delta V^0_{\text{complex}}, \text{cm}^3 \text{mol}^{-1}$
	0	5	2.0	$+10.9 \pm 0.2$	$+20 \pm 2$
	1	0	5.1	$+8.6 \pm 0.3$	$+10 \pm 2$
	2	-3	6.6	$+7.7 \pm 0.2$	$+1 \pm 2$
	3	-4	8.5	$+11.7 \pm 0.3$	-2 ± 2
	2	-1	10.4	$+11.9 \pm 0.2$	$+6 \pm 2$
	3	0	12.0	$+28.0 \pm 1.0$	$+14 \pm 3$

In the present study on the redox reactions of seven-coordinate Fe^{III} complexes coupled to the transfer of different numbers of protons (eq 2.5), the experimental value of $V^0_{\text{H}^+} = -7.7 \pm 0.8 \text{ cm}^3 \text{ mol}^{-1}$ was adopted since it is based on data obtained for deprotonation reactions of metal complexes and as such is closely related to the proton transfer processes studied here. In Tables 2.3 and 2.4, the studied reactions are summarized along with the experimentally obtained values of ΔV^0_{cell} and the calculated values of $\Delta V^0_{\text{complex}}$. The values of $\Delta V^0_{\text{complex}}$ were corrected for the

reference electrode contribution and the effect of the different number of protons transferred upon reduction as formulated in eq 2.7. The error limits of $\Delta V_{\text{complex}}^0$ were calculated from the error limits of the various contributing terms in eq 2.7.

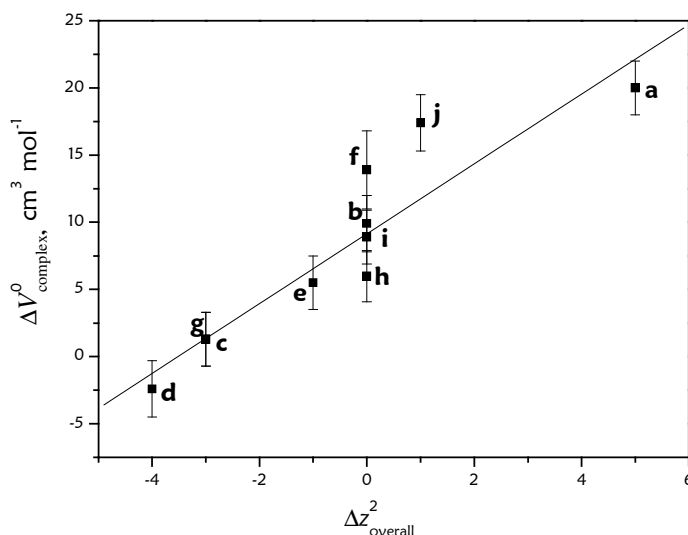


Figure 2.12. Plot of $\Delta V_{\text{complex}}^0$ versus $\Delta z_{\text{overall}}^2$, where $\Delta V_{\text{complex}}^0 = \Delta V_{\text{cell}}^0 - \Delta V_{\text{ref}}^0 + nV_{\text{H}^+}^0$ and $\Delta z_{\text{overall}}^2 = z_{\text{oxid}}^2 - z_{\text{red}}^2$. Fe(dapsc): pH = 2 (a), 5.1 (b), 6.6 (c), 8.5 (d), 10.4 (e) and 12 (f). Fe(dapsox): pH = 2.9 (g), 5.1 (h), 8.0 (i) and 11.0 (j).

The plot of $\Delta V_{\text{complex}}^0$ versus Δz^2 according to eq 2.7, using the data in Tables 2.3 and 2.4, is presented in Figure 2.12. Although the results include the data of two different seven-coordinate Fe complexes that undergo PCET reactions involving the transfer of a different number of protons, the plot shows a satisfactory fit and can be expressed as

$$\Delta V_{\text{complex}}^0 = (9.2 \pm 0.7) + (2.6 \pm 0.3) \Delta z_{\text{overall}}^2 \quad (2.10)$$

The intercept of the plot corresponds to the intrinsic volume change (ΔV_{intr}^0) associated with the electrochemical reduction of the pentagonal-bipyramidal Fe^{III} complexes. Although it is not easy to predict the contribution from intrinsic volume changes for non-spherical complexes, the obtained value of $+9.2 \pm 0.7 \text{ cm}^3 \text{ mol}^{-1}$ is

in good agreement with $\Delta V_{\text{intr}}^0 = +9.6 \text{ cm}^3 \text{ mol}^{-1}$ determined for the reduction of $[\text{Fe}(\text{H}_2\text{O})_6]^{3+}$.⁶⁷ According to structural data the increase in the Fe–H₂O bond length upon reduction is 0.131 Å.⁹⁰ On the basis of crystallographic data available for Fe^{III}(dapsc) and Fe^{II}(dapsc),^{64, 91, 92} the increase in the average equatorial bond length is approximately 0.1 Å during reduction. However, as a result of the presence of a deprotonated pentadentate in the case of Fe^{III} complexes and a protonated form in the case of Fe^{II} complexes, a somewhat larger change than 0.1 Å/bond is expected. A similar contribution is expected from the apical bonds in the case of the reduction of Fe^{III}–hydroxo to Fe^{II}–aqua species, since Fe–OH bonds are known to be shorter than Fe–OH₂ bonds. Thus, in the light of these possible deviations, the average value of $+9.2 \pm 0.7 \text{ cm}^3 \text{ mol}^{-1}$ is quite acceptable for the intrinsic volume change upon reduction of the studied Fe^{III} complexes. The deviation of some of the data points from the linear plot in Figure 2.12, especially around $\Delta z^2 = 0$, can possibly be accounted for in terms of deviations in the value of ΔV_{intr}^0 from the average value quoted above. In particular, in the case of Fe^{III/II}dapsox (h and j in Figure 2.12), the larger deviations from the linear plot can be explained by the fact that at pH 5.1, upon reduction, only a single protonation of the larger and more rigid pentadentate ligand takes place. This will cause a significantly smaller intrinsic volume change than the protonation of two coordinated OH⁻ ligands at pH 11.0 that results in the elongation of the Fe–O bonds.

In the case of Fe^{III/II}dapsc at pH 12.0 (f in Figure 2.12), a number of factors can play a role. As a result of the fact that the complex is triply protonated upon reduction, whereas at the same time there is no change in the absolute charge, a larger intrinsic volume change is also expected. In this case, the protonation of one coordinated OH⁻ also occurs and results in the elongation of the Fe–O bond, which is even more pronounced because of the trans influence caused by the remaining nonprotonated OH⁻ group.

The slope of the plot in Figure 2.12 is very close to that observed in the series of neutralization reactions studied before⁷⁵ and is smaller than that observed in redox

processes in which no coupled proton-transfer reactions occur.⁷² The smaller slope suggests weaker electrostriction dependence. Electrostriction effects for PCET reactions follow the trend observed for proton-transfer reactions. It should, however, also be kept in mind that the earlier studies on pure electron-transfer reactions^{67, 69-72} included only six-coordinate octahedral complexes, whereas the present work deals with seven-coordinate pentagonal-bipyramidal complexes. In that case the charge is spread out over a larger coordination sphere, thus, allowing for somewhat diluted electrostriction effects are expected.

2.1.5. Conclusion

For the first time the acid–base equilibria of seven-coordinate Fe^{III} and Fe^{II} complexes with 2,6-diacetylpyridine-bis(acylhydrazone) chelates could be studied in detail, and the speciation over a wide pH range could be resolved. On the basis of these data, the effect of pressure on the redox processes in which a different number of protons are involved (from 0 to 3 protons per electron) was studied for all the different protonation forms of the two selected complexes. This is the first time that the effect of pressure on the redox potential of proton-coupled electron-transfer processes has been investigated. Interestingly, previously reported linear correlations found between Δz^2 and the redox reaction volumes⁶⁹⁻⁷² as well as the neutralization reaction volumes⁷⁵ for different types of transition metal complexes, were also observed in the present study in which the two processes were combined. Consequently, the change in overall charge is not only caused by change in the oxidation state of the metal center but also by protonation/deprotonation of the pentadentate chelate or the coordinated water ligand. Thus, the approximately linear dependence of the reaction volume on Δz^2 seems to have general application and was shown to be valid for proton-coupled electron transfer as well (Figure 2.13).

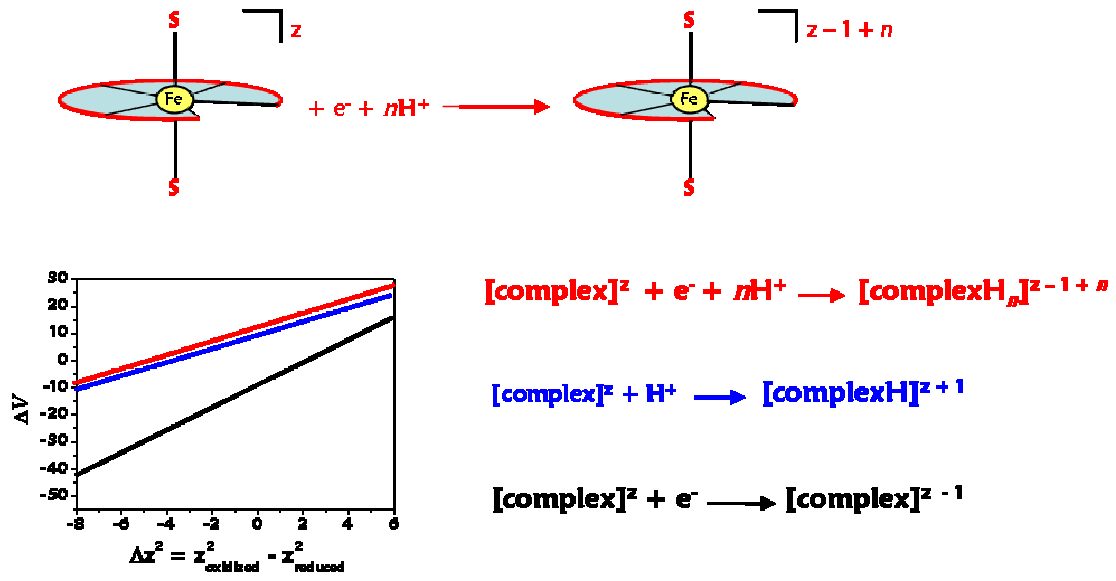


Figure 2.13. Summary of the relevant conclusions.

2.2. Evidence for a Concerted Proton-Electron Transfer Mechanism

2.2.1. General Remark

The work presented below is in preparation for submission to the Journal of the American Chemical Society:

Sarauli, D.; van Eldik, R.; Ivanović-Burmazović, I. **2008**.

2.2.2. Introduction

The Fe- and Mn-containing superoxide dismutases (SODs) are a diverse group of metalloenzymes critical to the existence of oxygen-tolerant organisms. They catalyze the disproportionation of the superoxide radical to hydrogen peroxide and dioxygen (eq 2.11, [Section 1.2](#)), and thus protect aerobic living forms from oxidative damage caused by its excess.⁴⁵⁻⁴⁷ The mechanism of this disproportionation

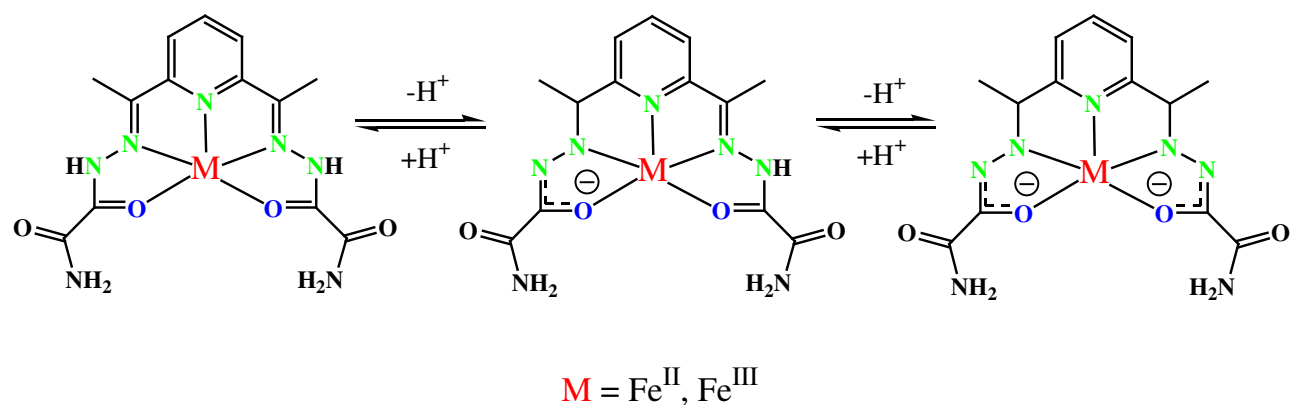


involves alternating reduction and oxidation of the trivalent and divalent catalytic iron or manganese metal centers.^{2, 35, 36, 43, 93} This net reaction is an exceptionally simple one, yet it incorporates central themes of redox catalysis in general, including the coupling between protons and electrons, which is a potent device for conservation, transduction and utilization of energy. Indeed, Bull and Fee demonstrated that FeSOD takes up one proton in conjunction with one electron, across the whole pH range of activity.³⁶ Furthermore, even by supplying only one of two protons required for the formation of H₂O₂, the enzyme can greatly promote and accelerate the reduction of O₂^{•-}.⁹⁴

In general, proton-coupled electron transfer (PCET) processes are essential in most cases of enzymatic catalysis ([Section 1.2.1.1](#)).⁹⁵⁻⁹⁹ However, often it is difficult to recognize and demonstrate whether they take place in a concerted way (CPET) or as

separate individual processes involving initial electron transfer (ET-PT) or initial proton transfer (PT-ET). This question has promoted great theoretical and experimental interest.^{40, 43, 100-106} Parallel to numerous theoretical approaches,^{100, 102, 107-110} concerted pathways were experimentally demonstrated to be involved in different biological systems, such as photosystem II and its related mimics,^{99, 111-116} cytochrome c oxidase,¹⁰⁴ ribonucleotide reductase,¹¹⁷ copper-containing monooxygenase/oxidase,¹¹⁸ and recently suggested for the functioning of superoxide dismutase.^{21, 43, 49, 119} To conceive whether a reaction proceeds by a concerted pathway, it is valuable to know both the thermodynamics and kinetics of all ET, PT and CPET steps. This is usually difficult to establish experimentally in the case of enzymatic systems in general and of the SOD enzymes in particular. Consequently, detailed thermodynamic and kinetic investigations on adequate stable low-molecular-weight metal complexes, which are able to catalyze $O_2^{\bullet-}$ dismutation, are of great importance.

In the latest report,⁵² it was demonstrated that the seven-coordinate Fe^{II} , Fe^{III} and Mn^{II} complexes of the acyclic and rigid $H_2dapsox$ ligand [$H_2dapsox = 2,6$ -diacetylpyridine-bis(semioxamazide)]^{53, 63} with pentagonal-bipyramidal geometry were able to catalytically decompose $O_2^{\bullet-}$, contrary to the previous postulations that only seven-coordinate complexes of macrocyclic ligands with prominent conformational flexibility could possess SOD activity.^{48, 51} The manganese complex demonstrated higher SOD activity than the analogous iron complex.⁵² However, high stability of the iron complexes over a very wide pH range⁵⁴ is an advantage in terms of detailed mechanistic studies of proton-coupled electron transfer. The $Fe^{II/III}dapsox$ complexes exhibiting four acid-base equilibria in the pH range 1-12 (Scheme 2.4), have been proven to represent excellent models for studying multiple PCET processes, since the number of protons exchanged during the redox reaction varies from 1 to 2 protons per electron along the studied pH region (Section 2.1.4).⁵⁴



Scheme 2.4.

These interesting features allow the elucidation of the thermodynamics of all PT steps (for both iron oxidation states) by determining acid dissociation constants (K_a) at different temperatures, as well as by temperature-dependent cyclic voltammetric measurements for the determination of the driving force of each ET and CPET reaction steps at different pH values. If the concerted proton-electron transfer occurs, then its driving force is more favorable than those of the rate-limiting steps of ET-PT or PT-ET reaction pathways.¹²⁰

In general, PCET reactions, carried out in water, especially in buffered solutions, have currently attracted particular interest of different research groups.^{56, 108, 113, 121-123} Costentin et al. summarized various expected stepwise and CPET reaction pathways in aqueous media and discussed them on thermodynamic and kinetic bases.¹⁰⁸ If water acts as proton acceptor, the CPET pathway was demonstrated to compete favorably with the stepwise pathway. In buffered medium, the basic component of the buffer may serve as a proton acceptor in the CPET mechanism.¹⁰⁸ One of the major unresolved questions inducing controversial interpretation in the literature,^{108, 124, 125} is whether the driving force and consequently the rate constant for the PCET is a pH-dependent process or not. Electrochemistry, through techniques like cyclic voltammetry, may provide a quite effective access to concerted proton-coupled electron transfer in terms of diagnosis and quantitative kinetic characterization.^{107, 126, 127} Still, reports on electrochemical CPET are insufficient, with rather hypothetically

or theoretically established than experimentally demonstrated reaction mechanisms.^{128, 129}

In the subsequent Sections, the results from temperature-dependent thermodynamic and kinetic electrochemical studies of all Fe^{II/III}dapsox complex species existing in aqueous solution over the pH range 1-12 in buffered and unbuffered media will be reported. On the basis of the obtained temperature-dependent half-wave potentials ($E_{1/2}$) of each ET and PCET steps, the driving forces were determined. Temperature-dependent potentiometric titrations were carried out to clarify the thermochemistry of all PT steps. Since a major manifestation of concerted proton-electron transfer is the existence of the deuterium kinetic isotope effect (KIE),^{109, 110, 114, 130, 131} we compared the measured heterogeneous rate constants (k_{el}) for the electrode reactions in H₂O and D₂O for certain complex species. Relying on the latest evidence that the concerted proton-electron transfer processes might be present in the natural SOD enzymes,⁴³ the experimentally gained results for their mimetics in this section were analyzed mechanistically in order to rule out other possible reaction pathways.

2.2.3. Experimental Section

2.2.3.1. Chemicals

All reagents and solvents were commercially available (Sigma, Acros Organics, Fluka) and used without further purification. Deionized Millipore water was used for all types of measurements.

[Fe^{II}(H₂dapsox)(H₂O)₂](NO₃)₂·H₂O and [Fe^{III}(dapsox)(H₂O)₂]ClO₄: Complexes were prepared and characterized as described previously (see also 2.1.3.2).^{52, 53}

2.2.3.2. pH Potentiometric Titrations

Temperature-dependent potentiometric titrations of [Fe^{II}(H₂dapsox)-(H₂O)₂](NO₃)₂·H₂O and [Fe^{III}(dapsox)(H₂O)₂]ClO₄ were performed on a METROHM 702 SM Titrino in a jacketed, air-tight glass titration cell equipped with a combined pH glass electrode (Metrohm), N₂ inlet and outlet, and a graduated 20

ml microburet (METROHM). The pH electrode was calibrated at each measurement temperature using four different commercially available standard buffer solutions of pH = 2, 4, 7 and 10. This calibration allowed direct interpretation of pH data in terms of H^+ concentration. The ion product of water, i. e. $pK_w = -\log [H^+][OH^-]$, was determined experimentally for each temperature. Carbonate-free 0.05 M sodium hydroxide or perchloric acid solutions were prepared with boiled, distilled and nitrogen saturated water and were standardized by titrations with 0.05 M potassium hydrogen phthalate solution. Gran's method^{77, 78} was used to confirm the absence of carbonate in the sodium hydroxide standard solution (carbonate content 0.13 %). The temperatures suitable for the measurements were adjusted and kept constant by circulating thermostated water through the outer jacket of the cell. All measurements were carried out under a constant atmosphere of nitrogen above the solution and were repeated at least four times (with both HCl and NaOH). The concentration of the complexes was 1×10^{-3} M and the ionic strength was kept constant at 0.1 M with $NaClO_4$. The temperature-dependent pK_a values and species distribution of the complexes were calculated using the program TITFIT.⁷⁹

2.2.3.3. Electrochemical Measurements

Cyclic voltammograms were recorded on an Autolab PGSTAT 30 device (Eco Chemie). The electrodes were as follows: working, gold disk electrode (geometric area: 0.07 cm^2) (Metrohm); auxiliary, platinum wire (Metrohm); and reference, Ag/AgCl (3M NaCl) (Metrohm) in 0.1 M $NaClO_4$ electrolyte solution. The concentration of the iron complex species was 1 mM. The pH of the solutions was measured with a Mettler Delta 350 pH meter using a combined glass electrode. The latter was calibrated applying standard buffer solutions (pH = 4, 7 and 10) and 0.1 M HCl (pH = 1). The pH-electrode was filled with NaCl instead of KCl to prevent precipitation of $KClO_4$. The pH values of solutions were controlled using perchloric acid, NaOH and different buffer systems (MES, TAPS). The buffer systems were selected in a way to have the same experimental conditions as already published (Section 2.1). All solutions were initially thoroughly degassed with pre-purified

nitrogen (15 min) and a stream of N₂ gas was passed over the sample solutions during the measurements.

For temperature-dependent cyclic voltammetry, a single solution was used for each system. Typically, the electrochemical one-compartment isothermal cell was prepared and degassed and CVs were collected, yielding $E_{1/2}$ vs. Ag/AgCl/3M NaCl reference electrode. The entire cell was then placed in a warm water bath and allowed to come to thermal equilibrium before CVs were collected. This process was repeated using an ice bath. The cell was allowed to return to ambient temperature, and a final series of CVs were collected; in all cases, the $E_{1/2}$ was found to be within 4 mV of the initial room-temperature measurements. Scan rates were optimized for each system in order to obtain reversible (quasi-reversible) behavior with a peak separation ΔE (difference between anodic and cathodic peaks) of around 60-80 mV. The peak separation as well as $E_{1/2}$ was determined from the original CV current peak positions and compared with those simulated by GPES software.⁸³ An excellent agreement between these values was found. The values of all measured half-wave potentials ($E_{1/2(\text{exp})}$) were finally converted to be cited vs. normal hydrogen electrode, taking into consideration the correction of the variation of the redox potential of the reference electrode with temperature [$E_{1/2\text{corr}} = E_{1/2(\text{exp})} - 0.33(T - 25^\circ\text{C})$]. Additionally, the obtained corrected values were extrapolated to the values at pH = 0, resulting in $E_{1/2}^0$ values.

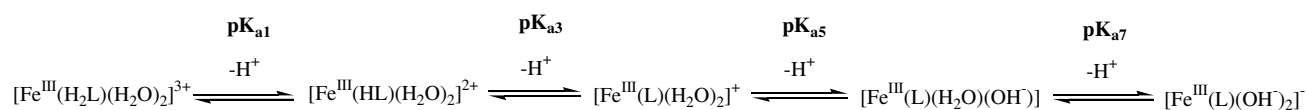
During determination of the heterogeneous rate constant k_{el} , the gold disk working electrode surface was gently polished with 0.05- μm alumina before each experiment, then sonicated in water, and air-dried immediately before use. CVs were recorded in a quite broad range of scan rates ν (10 – 4000 mV s⁻¹). At the lower scan rates $E_{1/2}$ was found to be independent of ν and reproducible to ± 1 mV. The uncompensated resistance R_u of the electrochemical cell was measured at each experiment and was found to have a negligible effect on the measured $E_{1/2}$ (< 5 mV). The transfer coefficient $\alpha = 0.5$, did not change with pH and remained constant for all complex species.

For evaluation of the deuterium kinetic isotope effect (KIE), DClO_4 and NaOD were used to adjust the pD of solutions. The values of pD were determined by using the following relation: $\text{pD} = \text{pH}_{\text{read}} - 0.4$.¹³² All measurements were carried out at a constant ionic strength of $I = 0.1 \text{ M}$ (NaClO_4).

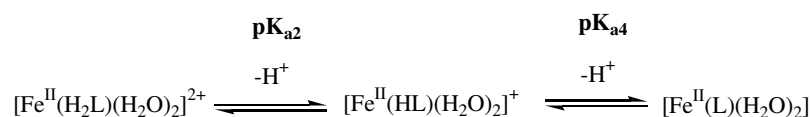
2.2.4. Results

2.2.4.1. Thermodynamics of Proton Transfer (PT) Reactions

In the previously published report (Section 2.1) it was possible to resolve all acid-base equilibria of seven-coordinate $[\text{Fe}^{\text{III/II}}(\text{dapsox})(\text{H}_2\text{O})_2]\text{ClO}_4$ complexes over a wide pH range at $25 \text{ }^\circ\text{C}$. To provide additional insight into the thermodynamic aspects of proton transfer steps (Schemes 2.5 and 2.6), temperature-dependent pH titrations of the before mentioned complexes were carried out. The changes in $\text{p}K_{\text{an}}$ ($n = 1, 3, 5, 7$ for $\text{Fe}^{\text{III}}\text{dapsox}$; $n = 2, 4$ for $\text{Fe}^{\text{II}}\text{dapsox}$) values with temperature are summarized in Tables 2.5 and 2.6. A least-squares regression analysis of $R\ln K_a$ versus T ($R\ln K_a = \Delta S^\circ - \Delta H^\circ/T$, van't Hoff plot) had a slope and an intercept related to the values of ΔH° and ΔS° , respectively. All plots were linear, with the points scattered in an apparently random fashion about the regression lines (Figure 2.14). The corresponding driving forces for all **proton dissociation steps** are also reported in Tables 2.5 and 2.6.



Scheme 2.5. $\text{Fe}^{\text{III}}\text{dapsox}$



Scheme 2.6. $\text{Fe}^{\text{II}}\text{dapsox}$

Table 2.5. Temperature-dependent pK_a values and the corresponding values of ΔG^0 according to Scheme 2.5.

t °C	pK_{a1}	pK_{a3}	pK_{a5}	pK_{a7}
5	1.685 ± 0.006	2.261 ± 0.003	6.069 ± 0.003	9.648 ± 0.003
15	1.666 ± 0.003	2.400 ± 0.005	6.171 ± 0.006	9.659 ± 0.003
25	1.643 ± 0.003	2.524 ± 0.005	6.250 ± 0.003	9.669 ± 0.002
35	1.626 ± 0.006	2.627 ± 0.006	6.384 ± 0.005	9.682 ± 0.004
ΔG^0_{298} , kJ mol ⁻¹				
	$+8 \pm 1$	$+14 \pm 2$	$+35 \pm 2$	$+55 \pm 5$

Table 2.6. Temperature-dependent pK_a values and the corresponding values of ΔG^0 according to Scheme 2.6.

t °C	pK_{a2}	pK_{a4}
5	3.173 ± 0.004	6.605 ± 0.008
15	3.322 ± 0.003	6.315 ± 0.004
25	3.550 ± 0.003	6.005 ± 0.006
35	3.880 ± 0.003	5.757 ± 0.004
ΔG^0_{298} , kJ mol ⁻¹		
	$+20 \pm 3$	$+34 \pm 1$

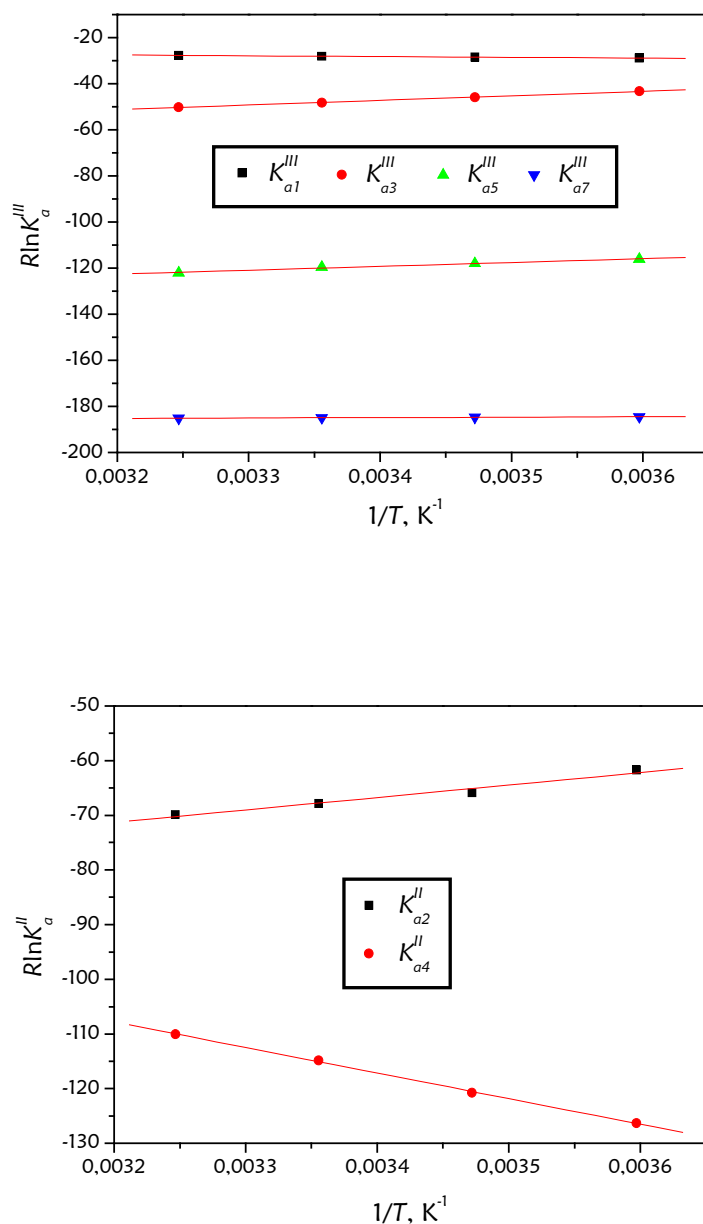


Figure 2.14. Van't Hoff plots of the data summarized in Tables 2.5 (above) and 2.6 (below).

2.2.4.2. Effect of Temperature on Net Proton-Electron Transfer (PCET)

On the basis of the resolved species distribution (Sections 2.1.4.5 and 2.1.4.6), temperature-dependent cyclic voltammetric measurements at certain pH values, chosen by virtue of different numbers of protons involved in redox processes, were performed.

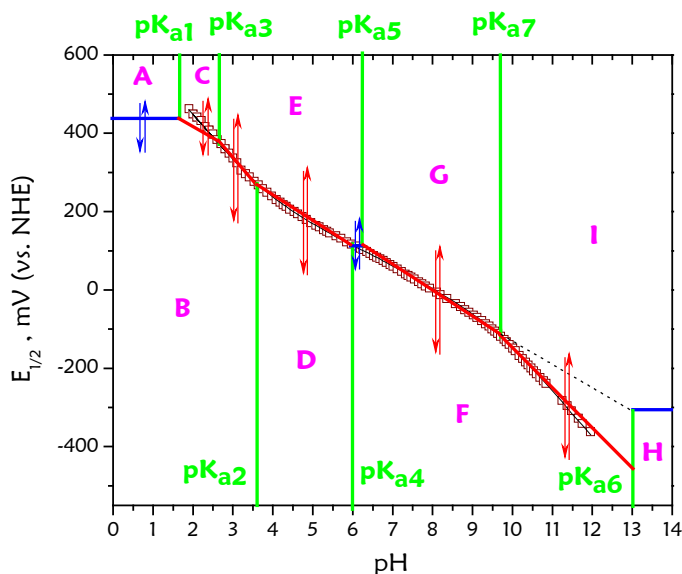


Figure 2.15. pH-dependent redox potential diagrams of the $\text{Fe}^{\text{III/I}}$ dapsox system. Experimental conditions: $[\text{complex}] = 1 \times 10^{-3} \text{ M}$, scan rate = 50 mV/s, $T = 298 \text{ K}$, and $I = 0.1 \text{ M NaClO}_4$. Solid lines represent fit-data (EFIT). For the assignment of the species A-H see Schemes 2.5 and 2.6, also [Section 2.1.4.6](#).

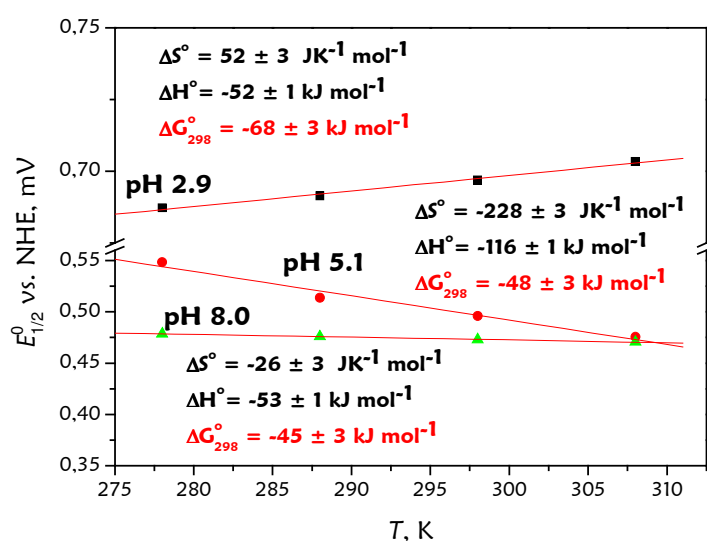
According to the pH-dependent half-wave potential diagram (Figure 2.15 presents the modified diagram from Figure 2.10 (above)), the following pH values (with corresponding net proton-electron transfer processes in brackets) were selected for the temperature-dependent cyclic voltammetry measurements: pH 2.9 ($E \rightarrow B$, $1e^-/2H^+$, no buffer), pH 5.1 ($E \rightarrow D$, $1e^-/1H^+$, MES buffer), pH 8.0 ($G \rightarrow F$, $1e^-/1H^+$, TAPS buffer) and pH 11 ($I \rightarrow F$, $1e^-/2H^+$, no buffer). In all these processes (red lines and arrows in Figure 2.15), in general described by eq 2.12,



(O and R are the oxidized deprotonated and reduced protonated forms of the redox couples, respectively), transfer of n electrons and m protons (PCET) occurs.

Table 2.7. Temperature-dependent $E_{1/2}^0$ values for selected PCET processes and corresponding values of ΔG_{298}^0 .

T, K	$E_{1/2}^{E \rightarrow B}$ vs. NHE, V	$E_{1/2}^{E \rightarrow D}$ vs. NHE, V	$E_{1/2}^{G \rightarrow F}$ vs. NHE, V
278	0.6872 ± 0.002	0.5486 ± 0.002	0.4786 ± 0.001
288	0.6914 ± 0.003	0.5138 ± 0.001	0.4758 ± 0.004
298	0.6969 ± 0.003	0.4962 ± 0.001	0.4729 ± 0.003
308	0.7034 ± 0.002	0.4756 ± 0.001	0.4707 ± 0.002
$\Delta G_{298}^0, \text{kJ mol}^{-1}$	-68 ± 3	-48 ± 3	-45 ± 3

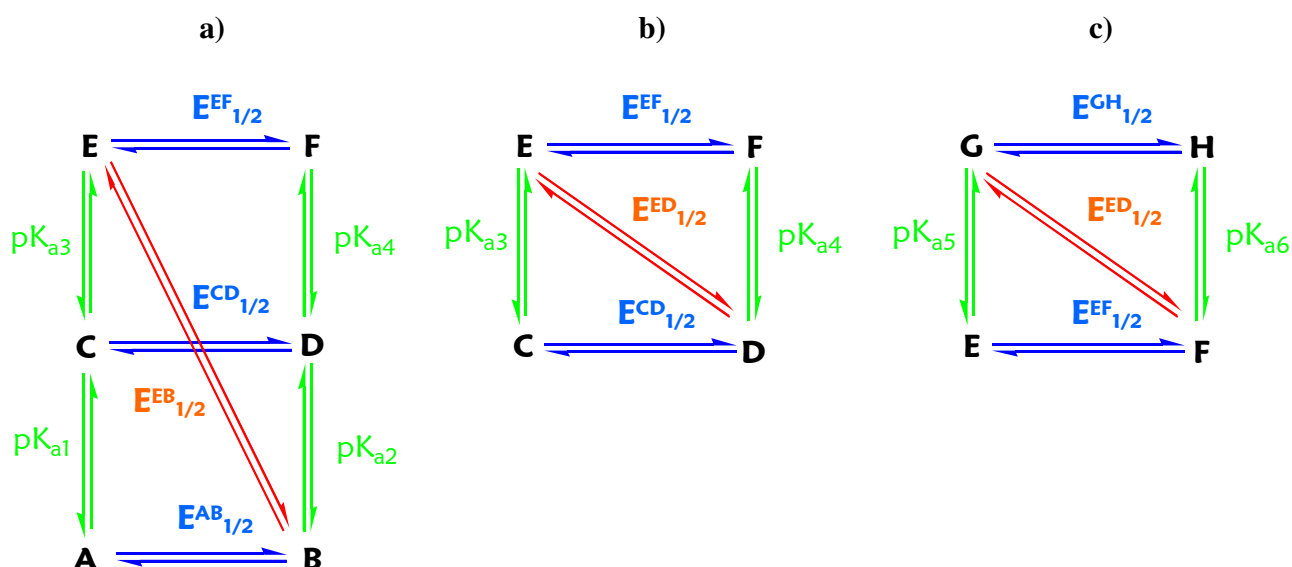
**Figure 2.16.** Plots of $E_{1/2}^0$ of selected PCET processes versus T . All relevant values are given in Table 2.7.

The mean values of $E_{1/2}$ for all corresponding complex species were calculated in the range of ascending scan rates (10 – 200 mV/s) at which CVs were found to be fully reversible ($E_{\text{ox}} - E_{\text{red}} = 60 \text{ mV}$). The experimental values were converted to $E_{1/2}^0$ vs.

NHE (see [Section 2.2.3.3.](#)) and are reported in Table 2.7. Unfortunately, at pH 11 and lower temperatures the CV measurements were unsuccessful, since the presence of indefinable additional complications led to greatly broadened voltammograms even for those taken at the lowest scan rate.

To gain an insight into the thermochemistry of the mentioned PCET processes, the driving forces of each reaction by plotting $E_{1/2}^0$ values versus temperature [$E_{1/2}^0 = (T\Delta S^0 - \Delta H^0)/F$, $\Delta G^0 = \Delta H^0 - T\Delta S^0$, Figure 2.16] were determined. The values of PCET driving forces are summarized in Table 2.7.

2.2.4.3. Effect of Temperature on Discrete Electron Transfer (ET) Steps



Scheme 2.7. ET steps are marked blue, PT steps green, PCET steps red. The complex species were assigned in accordance with Figure 2.14. Mechanisms: a) 1e⁻, 2H⁺ six-member ladder reaction scheme (pH 2.9); b) 1e⁻, 1H⁺ square reaction scheme (pH 5.1); c) 1e⁻, 1H⁺ square reaction scheme (pH 8.0).

In the early 80's Laviron presented a theoretical analysis of the square (1e⁻, 1H⁺)¹³³ and six-member ladder (1e⁻, 2H⁺)¹³⁴ schemes of heterogeneous reactions with protonations occurring in solution near the electrode and assumed then to be at equilibrium. It was shown that if the transfer coefficient α is 0.5 for all electrochemical processes, and the diffusion coefficients for all oxidized and reduced

complex species are equal ($D_{\text{ox}}/D_{\text{red}} = 1$), such reaction behaves as a single monoelectronic process. Later it will be shown that these conditions are applicable in our system, so the studied processes can be described in the way demonstrated in the Schemes 2.7a, 2.7b and 2.7c.

From electrostatic arguments, the acid dissociation constants (K_a) in the mentioned reaction schemes decrease from left to right; hence, $\text{p}K_a$ values increase from left to right.¹⁰² Similarly, formal potentials become more positive moving from top to bottom. In general, within a system, the higher oxidation state species are more acidic and the more protonated species are more oxidizing.^{102, 135} Because ET and PT are part of the same square, the difference between the $\text{p}K_a$ values is equal to the difference in redox potentials divided by 0.059 V (to convert ΔE to a \log_{10} equilibrium constant). The ΔE or $\Delta \text{p}K_a$ value is the thermodynamic coupling between the proton and the electron, describing how sensitive the proton properties are to the presence or absence of the electron and vice versa. It is a key parameter in any proton-coupled electron transfer process.^{39, 102, 120}

The following equations for the determination of all pH-independent couples (ET reactions: $A \rightarrow B, C \rightarrow D, E \rightarrow F, G \rightarrow H$; see Schemes 2.7a, 2.7b and 2.7c) can be written as:^{133, 134}

$$E_{1/2}^{A \rightarrow B} = E_{1/2}^{C \rightarrow D} + (2.3RT/F)(\text{p}K_{a2} - \text{p}K_{a1}) \quad (2.13)$$

$$E_{1/2}^{C \rightarrow D} = E_{1/2}^{E \rightarrow B} - (2.3RT/F) \log\left(\frac{[H^+]/K_{a2} + 1 + K_{a4}/[H^+] }{[H^+]/K_{a1} + 1 + K_{a3}/[H^+]}\right) \quad (2.14)$$

$$E_{1/2}^{E \rightarrow F} = E_{1/2}^{E \rightarrow D} - (2.3RT/F) \log(1 + [H^+]/K_{a4}) / (1 + [H^+]/K_{a3}) \quad (2.15)$$

$$E_{1/2}^{G \rightarrow H} = E_{1/2}^{G \rightarrow F} - (2.3RT/F) \log(1 + [H^+]/K_{a6}) / (1 + [H^+]/K_{a5}) \quad (2.16)$$

Equations 2.14–2.16 are valid at all pH's. Consequently for the calculations, $E_{1/2(\text{corr})}$ were used instead of $E_{1/2}^0$ (see Section 2.2.3.3.). A plot of $E_{1/2}^{\text{EB}}$ (Scheme 2.7) versus pH exhibits a -120 mV pH^{-1} slope (Figure 2.15) in the range $\text{p}K_{a3} < \text{pH} < \text{p}K_{a2}$. $E_{1/2}^{\text{ED}}$ and $E_{1/2}^{\text{GF}}$ change each by -60 mV pH^{-1} at $\text{p}K_{a3} < \text{pH} < \text{p}K_{a4}$ and $\text{p}K_{a5} < \text{pH} < \text{p}K_{a6}$.

respectively. The pK_{a6} value could not be obtained from potentiometric titration measurements. Therefore eq 2.16 was not taken into account. Since some electrochemical measurements were carried out in MES (process $E \rightarrow D$) and TAPS (process $G \rightarrow F$) buffer systems, which show significant temperature-dependence of their pK_a and high values of reaction enthalpies,^{136, 137} the related temperature-dependent change in solution pH was included in the calculation of E values. Apart from that, it is theoretically possible to determine the redox potentials for all four above listed pH-independent couples ($E_{1/2}^{A \rightarrow B}$, $E_{1/2}^{C \rightarrow D}$, $E_{1/2}^{E \rightarrow F}$ and $E_{1/2}^{G \rightarrow H}$ in Scheme 2.7). The conclusion can be drawn that two processes ($C \rightarrow D$ and $G \rightarrow H$) do not occur in solution (Figure 2.15). The values of $E_{1/2}^{A \rightarrow B}$ ($pH < pK_{a1}$) and $E_{1/2}^{E \rightarrow F}$ ($pK_{a4} < pH < pK_{a5}$) at all measurement temperatures were calculated and summarized together with the corresponding values of the driving force in Table 2.8.

Table 2.8. Temperature-dependent $E_{1/2}$ values (calculated according to eqs. 2.14-2.16) for the occurring ET processes and the corresponding values of ΔG^0_{298} .

T, K	$E_{1/2}^{A \rightarrow B}$ vs. NHE, V	$E_{1/2}^{E \rightarrow F}$ vs. NHE, V
278	0.488 ± 0.003	0.167 ± 0.004
288	0.459 ± 0.003	0.143 ± 0.003
298	0.442 ± 0.002	0.124 ± 0.003
308	0.432 ± 0.004	0.105 ± 0.003
$\Delta G^0_{298}, kJ mol^{-1}$	-43 ± 8	-12 ± 2

2.2.4.4. Effect of Temperature on Kinetics of Net Proton-Electron Transfer (PCET) on the Electrode Surface

The cyclic voltammograms of three chosen CPET processes at pH 2.9 ($E \rightarrow B$, $1e^-/2H^+$, no buffer), pH 5.1 ($E \rightarrow D$, $1e^-/1H^+$, MES buffer), pH 8.0 ($G \rightarrow F$, $1e^-/1H^+$,

TAPS buffer) and pH 11 ($I \rightarrow F$, $1e^-/2H^+$, no buffer) were quasi-reversible with $\Delta E_p > 60$ mV at scan rates higher than 200 mV/s. The rate constant for heterogeneous electron transfer (k_{el}) was therefore determined by analysis of the CV data at different scan rates ν (Nicholson's method)^{138, 139}

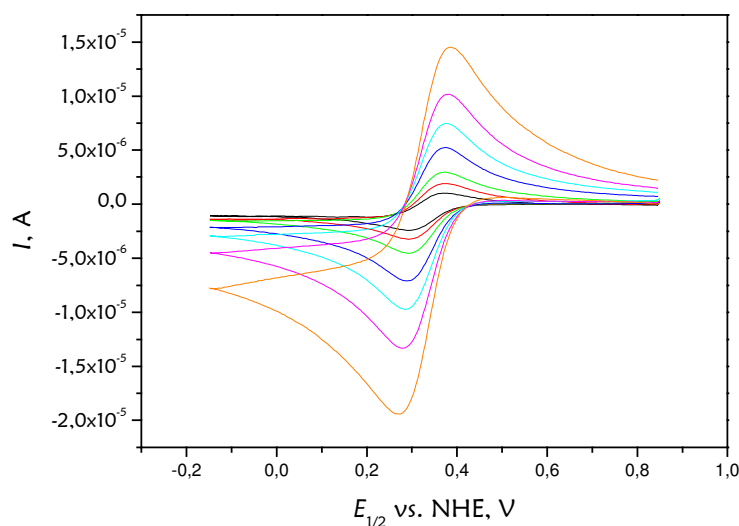


Figure 2.17. Scan rate-dependent CVs of the process $E \rightarrow B$ (Figure 2.15) at pH 2.9. Conditions: $[Fe^{III}dapsox] = 1 \times 10^{-3}$ M, $I = 0.1$ M ($NaClO_4$), $T = 298$ K. Au working electrode, scan rates = 0.05 – 0.5 V/s.

Figure 2.17 demonstrates the example of scan rate-dependent CVs in the case of pH 2.9 (process $E \rightarrow B$, $1e^-/2H^+$). k_{el} is related to ΔE_p and ν by eqs 2.17–2.19,

$$k_{el} = \psi \left(\frac{\pi D_{ox} F \nu}{RT} \right)^{1/2} \left(\frac{D_{red}}{D_{ox}} \right)^{\alpha/2} \quad (2.17)$$

$$\ln \psi = 3.69 - 1.16 \ln(\Delta E_p^{298} - 59) \quad (2.18)$$

$$I_{Ox/Red} = -0.446 n A C F \left(\frac{n F}{RT} \right)^{1/2} D_{Ox/Red}^{1/2} \nu^{1/2} \quad (2.19)$$

where I_{ox} , D_{ox} and I_{red} , D_{red} are the current maxima (A) and diffusion coefficients ($cm^2 s^{-1}$) for the oxidized and reduced forms of the analyte, respectively. ΔE_p^{298} is the

potential peak difference ($E_{\text{ox}} - E_{\text{red}}$, V) at 25 °C, α is the transfer coefficient (taken to be 0.5), A is the geometric area of the working electrode (cm^2), C is the concentration of complex species (mol cm^{-3}), and R and T have their standard meanings. Since the dimensionless charge transfer parameter $\psi(\Delta E_p)$ is known to be temperature-dependent,^{140, 141} one should modify eq 2.18 so that it can be applicable to the calculations of k_{el} at different temperatures (eq 2.20),

$$\ln \psi = 3.69 - 1.16 \ln \left(\frac{298}{T} \Delta E_p^T - 59 \right) \quad (2.20)$$

where ΔE_p^T is the potential peak difference at any measurement temperature T . All electrochemical data derived from cyclic voltammetry and used to determine k_{el} for the chosen CPET processes are summarized in Tables 2.9a–2.9c; all related plots are depicted in Figures 2.18–2.20.

Although solvent-dynamical control of electrode reaction rates is important in nonaqueous media, conventional transition-state theory seems to be valid for electrode kinetics in undiluted aqueous solutions.¹³⁹ Accordingly, plots of $R \ln(k_{\text{el}}/T)$ versus T (eq 2.21) were necessary to determine the Eyring parameters

$$R \ln \frac{k_{\text{el}}}{T} = \left(\Delta S_{\text{el}}^\ddagger - R \ln \frac{h}{k_B} \right) - \frac{\Delta H_{\text{el}}^\ddagger}{T} \quad (2.21)$$

ΔG^\ddagger ($\Delta G^\ddagger = \Delta H^\ddagger - T\Delta S^\ddagger$) of the selected reactions $E \rightarrow B$, $E \rightarrow D$ and $G \rightarrow F$ (see Schemes 2.7a–2.7c). All related values are combined in Table 2.10.

In additionally, the same electrochemical measurements were carried out with the structurally similar seven-coordinate $[\text{Fe}(\text{H}_2\text{dapsc})\text{Cl}_2]^+$ complex. Its speciation has already been carefully resolved⁴² (Section 2.1). Analogous to the principle reported in Section 2.1, temperature and pressure-dependent cyclic voltammograms at pH values where CPET processes occur (see Figure 2.10) were taken and all reaction and activation parameters for both complexes were determined. All measured data are summarized in Tables 2.11–2.14.

Table 2.9. All measured data required for the determination of diffusion coefficients and heterogeneous rate constants for the Fe^{III}/dapsox system (eqs 2.17, 2.19 and 2.20):**a)** pH 2.9 (process $E \rightarrow B$, $1e^-/2H^+$, $I = 0.1$ M NaClO₄/HClO₄)

$v, V s^{-1}$	$[I_{pa} (I_{pc})]_{278}, \mu A$	$[I_{pa} (I_{pc})]_{288}, \mu A$	$[I_{pa} (I_{pc})]_{298}, \mu A$	$[I_{pa} (I_{pc})]_{308}, \mu A$				
0.01	1.786 (1.696)	2.037 (1.902)	2.319 (2.092)	2.757 (2.625)				
0.02	2.541 (2.451)	2.909 (2.897)	3.364 (3.290)	4.021 (3.952)				
0.05	4.023 (3.983)	4.631 (4.641)	5.426 (5.433)	6.487 (6.514)				
0.1	5.639 (5.611)	6.549 (6.612)	7.725 (7.790)	9.310 (9.372)				
0.2	7.818 (7.797)	9.169 (9.285)	10.93 (11.07)	13.19 (13.41)				
0.5	11.82 (12.03)	14.02 (14.44)	16.96 (17.39)	20.60 (21.17)				
	$[D_{ox} (D_{red})]_{278},$ $\mu cm^2 s^{-1}$	$[D_{ox} (D_{red})]_{288},$ $\mu cm^2 s^{-1}$	$[D_{ox} (D_{red})]_{298},$ $\mu cm^2 s^{-1}$	$[D_{ox} (D_{red})]_{308},$ $\mu cm^2 s^{-1}$				
	0.6413 (0.7077)	0.9518 (1.0722)	1.5562 (1.6676)	2.3624 (2.5547)				
$v, V s^{-1}$	$\Delta E_p^{278},$ mV	ψ^{278}	$\Delta E_p^{288},$ mV	ψ^{288}	$\Delta E_p^{298},$ mV	ψ^{298}	$\Delta E_p^{308},$ mV	ψ^{308}
0.5	88.5	0.79	91.8	0.698	93.0	0.6573		
1	97.8	0.575	101.5	0.517	105.1	0.4718	106.2	0.458
1.5	107.2	0.447	111.1	0.408	111.2	0.4092	114.4	0.38
2	115.6	0.371	116.0	0.368			123.7	0.318
2.5	117.4	0.358	121.8	0.329	126.3	0.305	130.0	0.285

3	124.9	0.311	130.5	0.283				
3.5	125.8	0.306			134.2	0.2676	138.1	0.252
4	133.3	0.271						
5			147.9	0.22	139.1	0.2483	143.3	0.234
7					154.0	0.1814	148.4	0.218
10							173.2	0.164

k_{el}^{278} , 10^{-3} cm s ⁻¹	k_{el}^{288} , 10^{-3} cm s ⁻¹	k_{el}^{298} , 10^{-3} cm s ⁻¹	k_{el}^{308} , 10^{-3} cm s ⁻¹
---	---	---	---

5.2824

5.9937

6.7656

7.5826

b) pH 5.1 (process $E \rightarrow D$, $1e^-/1H^+$, 0.1 M MES buffer)

v , V s ⁻¹	$[I_{pa} (I_{pc})]_{278}$, μA	$[I_{pa} (I_{pc})]_{288}$, μA	$[I_{pa} (I_{pc})]_{298}$, μA	$[I_{pa} (I_{pc})]_{308}$, μA
0.01	2.013 (2.174)	2.336 (2.432)	2.541 (2.664)	2.804 (2.919)
0.02	2.855 (3.040)	3.344 (3.462)	3.704 (3.855)	4.102 (4.291)
0.05	4.380 (4.656)	5.221 (5.377)	5.930 (6.105)	6.644 (6.875)
0.1	5.831 (6.316)	7.052 (7.321)	8.129 (8.424)	9.202 (9.541)
	$[D_{ox} (D_{red})]_{278}$, $\mu cm^2 s^{-1}$	$[D_{ox} (D_{red})]_{288}$, $\mu cm^2 s^{-1}$	$[D_{ox} (D_{red})]_{298}$, $\mu cm^2 s^{-1}$	$[D_{ox} (D_{red})]_{308}$, $\mu cm^2 s^{-1}$
	1.0876 (0.941)	1.497 (1.397)	2.013 (1.875)	2.636 (2.449)

$\nu, \text{V s}^{-1}$	$\Delta E_p^{278},$ mV	ψ^{278}	$\Delta E_p^{288},$ mV	ψ^{288}	$\Delta E_p^{298},$ mV	ψ^{298}	$\Delta E_p^{308},$ mV	ψ^{308}
0.05	103.6	0.489	99.5	0.547	103.0	0.497	106.5	0.455
0.1	123.2	0.320	123.7	0.318	120.1	0.340	124.0	0.316
0.2	145.6	0.226	146.9	0.223	148.2	0.219	144.7	0.229
0.5	192.3	0.137	174.0	0.163	180.3	0.154	192.2	0.137
	$k_{el}^{278}, 10^{-3} \text{ cm s}^{-1}$		$k_{el}^{288}, 10^{-3} \text{ cm s}^{-1}$		$k_{el}^{298}, 10^{-3} \text{ cm s}^{-1}$		$k_{el}^{308}, 10^{-3} \text{ cm s}^{-1}$	
	1.3091		1.4825		1.6579		1.8494	

c) pH 8.0 (process $G \rightarrow F$, $1e^-/1H^+$, 0.1 M TAPS buffer)

$\nu, \text{V s}^{-1}$	$[I_{pa} (I_{pc})]_{278}, \mu\text{A}$	$[I_{pa} (I_{pc})]_{288}, \mu\text{A}$	$[I_{pa} (I_{pc})]_{298}, \mu\text{A}$	$[I_{pa} (I_{pc})]_{308}, \mu\text{A}$
0.007				
5	1.563 (1.702)	1.859 (1.944)	1.986 (2.152)	2.225 (2.386)
0.01	1.830 (1.878)	2.173 (2.221)	2.380 (2.536)	2.727 (2.910)
0.02	2.602 (2.533)	3.083 (2.970)	3.511 (3.594)	4.147 (4.258)
0.05	4.082 (3.747)	4.849 (4.403)	5.697 (5.386)	6.756 (6.450)
	$[D_{ox} (D_{red})]_{278},$ $\mu\text{cm}^2 \text{ s}^{-1}$	$[D_{ox} (D_{red})]_{288},$ $\mu\text{cm}^2 \text{ s}^{-1}$	$[D_{ox} (D_{red})]_{298},$ $\mu\text{cm}^2 \text{ s}^{-1}$	$[D_{ox} (D_{red})]_{308},$ $\mu\text{cm}^2 \text{ s}^{-1}$
	0.810 (0.776)	1.141 (1.013)	1.524 (1.669)	2.102 (2.251)

$v, \text{V s}^{-1}$	$\Delta E_p^{278},$ mV	ψ^{278}	$\Delta E_p^{288},$ mV	ψ^{288}	$\Delta E_p^{298},$ mV	ψ^{298}	$\Delta E_p^{308},$ mV	ψ^{308}
0.05	96.1	0.605	99.0	0.590	95.1	0.634	96.0	0.608
0.1	108.2	0.436	112.7	0.418	107.2	0.447	111.8	0.432
0.2	126.9	0.300	127.6	0.297	124.1	0.315	129.0	0.295
0.5	157.7	0.195	163.3	0.183	150.7	0.201	161.3	0.187
1	195.9	0.133	195.2	0.134	194.0	0.135	196.5	0.132
	$k_{el}^{278}, 10^{-3} \text{ cm s}^{-1}$		$k_{el}^{288}, 10^{-3} \text{ cm s}^{-1}$		$k_{el}^{298}, 10^{-3} \text{ cm s}^{-1}$		$k_{el}^{308}, 10^{-3} \text{ cm s}^{-1}$	
	1.3994		1.6108		1.8966		2.1782	

Table 2.10. Temperature-dependent heterogeneous rate constants of the chosen CPET processes and corresponding values of ΔG_{298}^\ddagger (see Tables 2.9a–2.9c, Figures 2.16–2.18).

T, K	$k_{el}^{E \rightarrow B}, 10^{-3} \text{ cm s}^{-1}$	$k_{el}^{E \rightarrow D}, 10^{-3} \text{ cm s}^{-1}$	$k_{el}^{G \rightarrow F}, 10^{-3} \text{ cm s}^{-1}$
278	5.2824	1.3091	1.3994
288	5.9937	1.4825	1.6108
298	6.7656	1.6579	1.8966
308	7.5826	1.8494	2.1782
$\Delta G_{298}^\ddagger, \text{kJ mol}^{-1}$	85 ± 2	89 ± 2	88 ± 1

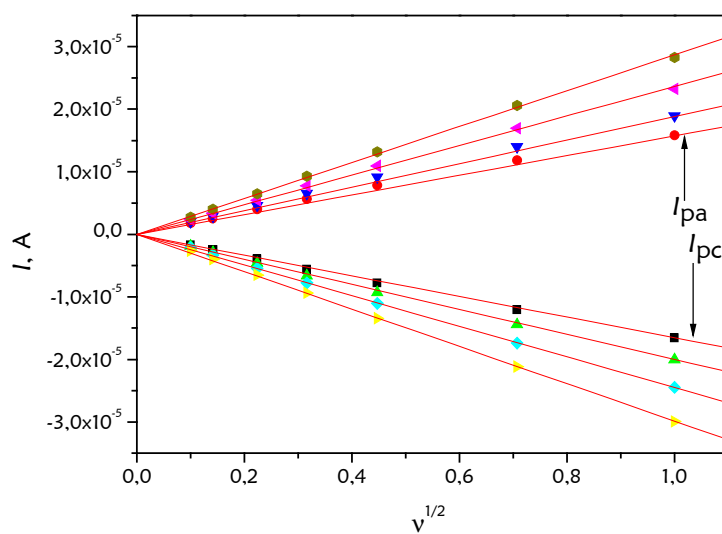
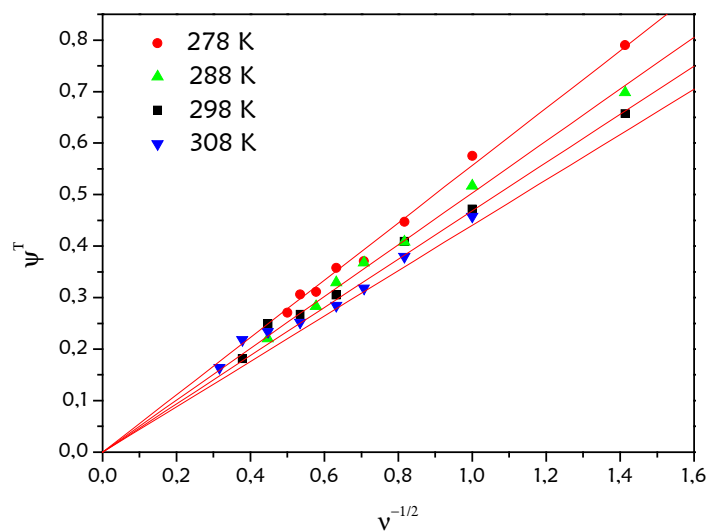
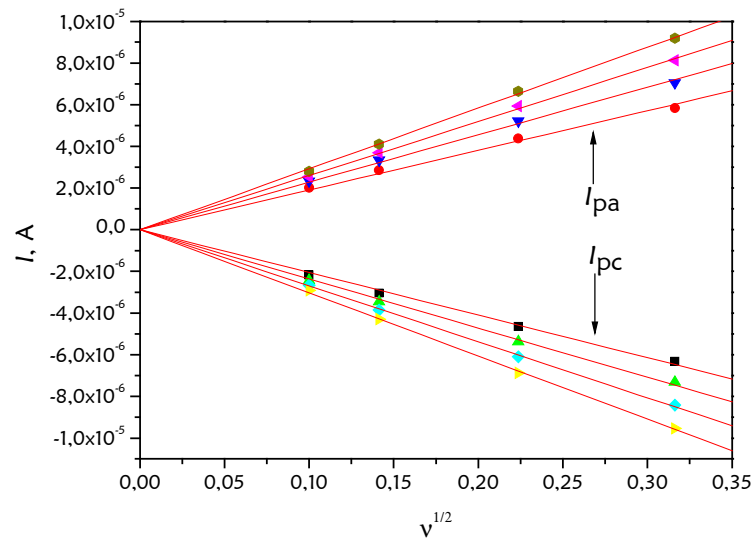
a) Determination of D according to eq 2.19 (see data in Table 2.9a)**b) Determination of k_{el} according to eqs 2.17 and 2.20 (see data in Table 2.9a)**

Figure 2.18. Experimental conditions: pH 2.9 (process $E \rightarrow B$, $1e^-/2H^+$, $I = 0.1$ M $\text{NaClO}_4/\text{HClO}_4$).

a) Determination of D according to eq 2.19 (see data in Table 2.9b)



b) Determination of k_{el} according to eqs 2.17 and 2.20 (see data in Table 2.9b)

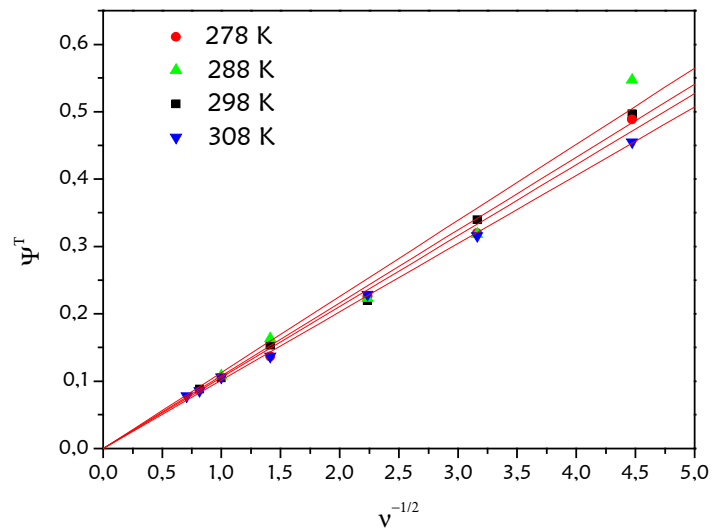


Figure 2.19. Experimental conditions: pH 5.1 (process $E \rightarrow D$, $1e/1H^+$, 0.1 MES buffer).

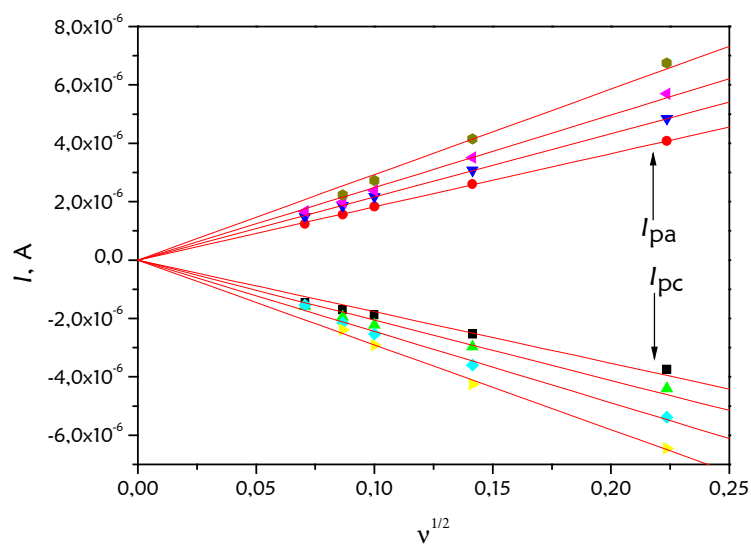
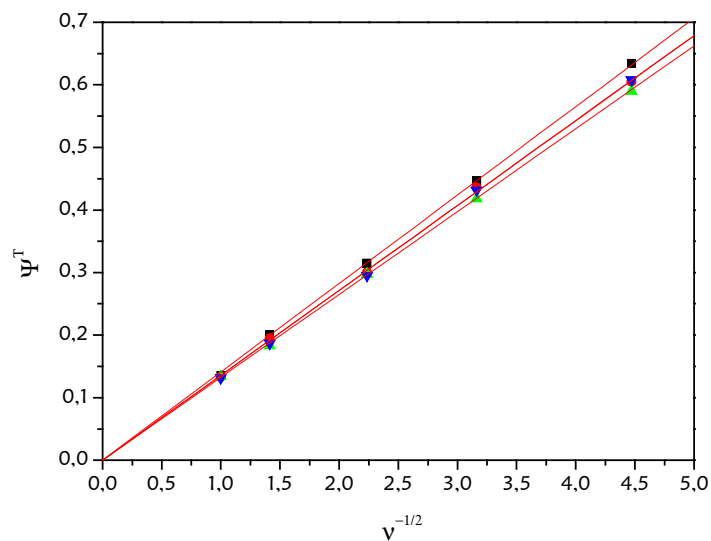
a) Determination of D according to eq 2.19 (see data in Table 2.9c)**b) Determination of k_{el} according to eqs 2.17 and 2.20 (see data in Table 2.9c)****Figure 2.20.** Experimental conditions: pH 8.0 (process $G \rightarrow F$, $1e^-/1H^+$, 0.1 M TAPS buffer).

Table 2.11. Fe(dapsox): species in aqueous solution before and after electrochemical reduction, number of protons transferred upon reduction, the difference in the square of the charge, thermodynamic parameters, redox potentials and pH values at which measurements were done.

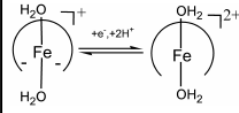
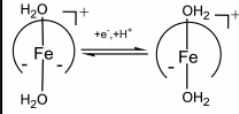
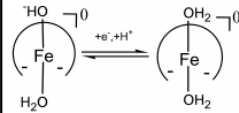
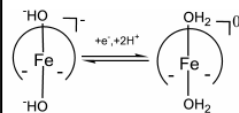
species	number of protons, n	$\Delta z^2_{\text{overall}}$	$\Delta S^{\text{corr}}_{\text{Ag/AgCl}}$, $\text{JK}^{-1} \text{mol}^{-1}$	$\Delta H_{\text{Ag/AgCl}}$, kJmol^{-1}	$\Delta G^{\text{corr}}_{\text{Ag/AgCl}}$, kJ mol^{-1}	$E_{1/2}$ vs. Ag/AgCl, V	pH
	2	-3	-60 ± 3	-52 ± 1	-33 ± 3	+0.135	2.9
	1	0	-274 ± 26	-98 ± 8	-15 ± 8	-0.049	5.1
	1	0	-38 ± 9	-11 ± 3	-2 ± 9	-0.209	8.0
	2	1	-	-	-	-0.473	11.0

Table 2.12. Fe(dapsox): species in aqueous solution before and after electrochemical reduction, number of protons transferred upon reduction, the difference in the square of the charge, heterogeneous rate constants, activation parameters, and pH values at which measurements were done.

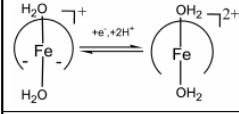
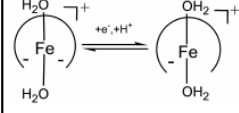
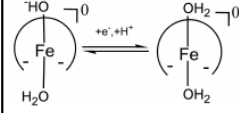
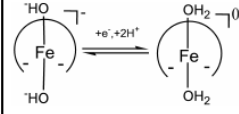
species	number of protons, n	$\Delta z^2_{\text{overall}}$	$k_{\text{el}} \times 10^2$, cm s^{-1} (25 °C)	ΔS^{\ddagger} , $\text{JK}^{-1} \text{mol}^{-1}$	ΔH^{\ddagger} , kJmol^{-1}	ΔV^{\ddagger} , $\text{cm}^3 \text{mol}^{-1}$	pH
	2	-3	0.68	-246 ± 3	12 ± 1	-7.4 ± 1.7	2.9
	1	0	0.17	-233 ± 5	19 ± 2	-7.8 ± 1.2	5.1
	1	0	0.19	-222 ± 2	22 ± 1	$+4.9 \pm 0.6$	8.0
	2	1	-	-	-	-	11.0

Table 2.13. Fe(dapsc): species in aqueous solution before and after electrochemical reduction, number of protons transferred upon reduction, the difference in the square of the charge, thermodynamic parameters, redox potentials and pH values at which measurements were done.

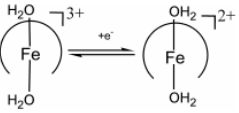
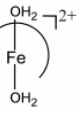
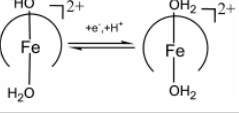
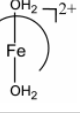
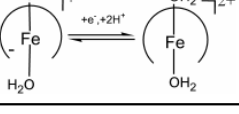
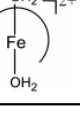
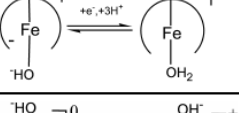
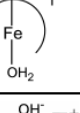
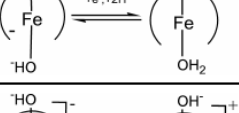
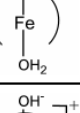
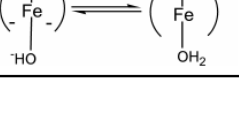
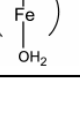
species	number of protons, n	$\Delta Z^2_{\text{overall}}$	$\Delta S^{\text{corr}}_{\text{Ag/AgCl}}$, $\text{JK}^{-1} \text{mol}^{-1}$	$\Delta H_{\text{Ag/AgCl}}$, kJmol^{-1}	$\Delta G^{\text{corr}}_{\text{Ag/AgCl}}$, kJ mol^{-1}	$E_{1/2}$ vs. Ag/AgCl, V	pH
 $\xrightarrow{+e^-}$ 	0	5	$+38 \pm 2$	-45 ± 1	-56 ± 2	+0.295	2.0
 $\xrightarrow{+e^-, +H^+}$ 	1	0	-59 ± 4	-60 ± 1	-42 ± 4	+0.165	5.1
 $\xrightarrow{+e^-, +2H^+}$ 	2	-3	-141 ± 3	-70 ± 1	-28 ± 3	+0.027	6.6
 $\xrightarrow{+e^-, +3H^+}$ 	3	-4	$+26 \pm 0.7$	$+5.0 \pm 0.1$	-3 ± 0.7	-0.247	8.5
 $\xrightarrow{+e^-, +2H^+}$ 	2	-1	-18 ± 3	$+13 \pm 1$	$+18 \pm 3$	-0.461	10.4
 $\xrightarrow{+e^-, +3H^+}$ 	3	0	$+20 \pm 1$	$+40 \pm 0.4$	$+34 \pm 1$	-0.617	12.0

Table 2.14. Fe(dapsc): species in aqueous solution before and after electrochemical reduction, number of protons transferred upon reduction, the difference in the square of the charge, heterogeneous rate constants, activation parameters, and pH values at which measurements were done.

species	number of protons, n	$\Delta Z^2_{\text{overall}}$	$k_{\text{el}} \times 10^2$, cm s^{-1} (25 °C)	ΔS^\ddagger , $\text{JK}^{-1} \text{mol}^{-1}$	ΔH^\ddagger , kJmol^{-1}	ΔV^\ddagger , $\text{cm}^3 \text{mol}^{-1}$	pH
	0	5	1.14	-252 ± 8	9 ± 2	-3.6 ± 0.6	2.0
	1	0	0.12	-228 ± 8	18 ± 2	$+3.1 \pm 0.9$	5.1
	2	-3	0.44	-232 ± 3	19 ± 1	-1.3 ± 0.3	6.6
	3	-4	0.19	-213 ± 3	25 ± 1	-16.6 ± 1.5	8.5
	2	-1	0.20	-166 ± 8	39 ± 2	-	10.4
	3	0	0.28	-173 ± 2	36 ± 1	-	12.0

2.2.4.5. Effect of Temperature on Kinetics of Discrete Electron Transfer (ET) Steps

Coming back to Laviron's theory for heterogeneous proton-coupled electron transfer reactions,^{133, 134} and taking into account Schemes 2.7a–2.7c, k_{el} values for the ET processes of the Fe^{III}dapsox system: $A \rightarrow B$ and $E \rightarrow F$ (the processes $C \rightarrow D$ and $G \rightarrow H$ were not considered, since they cannot occur in solution, see above) could be determined at each selected temperature. The following equations can be written:^{133, 134}

$$k_{\text{el}}^{E \rightarrow B} = \frac{k_{\text{el}}^{A \rightarrow B} [H^+] (K_{a1} K_{a2})^{-1/2} + k_{\text{el}}^{C \rightarrow D} + k_{\text{el}}^{E \rightarrow F} (K_{a3} K_{a4})^{1/2} [H^+]^{-1}}{([H^+] / K_{a1} + 1 + K_{a3} / [H^+])^{-1/2} ([H^+] / K_{a2} + 1 + K_{a4} / [H^+])^{-1/2}} \quad (2.22)$$

$$k_{el}^{E \rightarrow D} = \frac{k_{el}^{C \rightarrow D} ([H^+] / K_{a3}) + k_{el}^{E \rightarrow F} (K_{a4} / K_{a3})^{1/2}}{[1 + ([H^+] / K_{a3})]^{1/2} [(K_{a4} / K_{a3}) + ([H^+] / K_{a3})]^{1/2}} \quad (2.23)$$

$$k_{el}^{G \rightarrow F} = \frac{k_{el}^{E \rightarrow F} ([H^+] / K_{a5}) + k_{el}^{G \rightarrow H} (K_{a6} / K_{a5})^{1/2}}{[1 + ([H^+] / K_{a5})]^{1/2} [(K_{a6} / K_{a5}) + ([H^+] / K_{a5})]^{1/2}} \quad (2.24)$$

$k_{el}^{E \rightarrow B}$, $k_{el}^{E \rightarrow D}$ and $k_{el}^{G \rightarrow F}$ are the apparent heterogeneous rate constants listed in Table 2.10; K_{an} ($n = 1-6$) and $[H^+]$ represent the temperature-dependent acid dissociation constants (Tables 2.5 and 2.6), and the proton concentrations ($[H^+] = 10^{-pH}$) in solution, respectively. The above-mentioned temperature-dependent change in solution pH, for measurements performed in buffer media, was also considered in the calculation of k_{el} values. Since the processes $C \rightarrow D$ and $G \rightarrow H$ are not existing in our system (Figure 2.15), the corresponding $k_{el}^{C \rightarrow D}$ and $k_{el}^{G \rightarrow H}$ can be neglected. Because of the indefinable pK_{a6} value, eq 2.15 could also not be incorporated in our calculations. All these requirements simplify eqs 2.13 and 2.14, hence, $k_{el}^{A \rightarrow B}$ and $k_{el}^{E \rightarrow F}$ can easily be derived. Table 2.15 comprises the values of these heterogeneous rate constants, as well as corresponding Eyring activation parameters of the ET reaction steps; Figure 2.21 demonstrates the Eyring plots.

Table 2.15. The summarized values of temperature-dependent heterogeneous rate constants of ET steps together with the corresponding Eyring barriers.

T, K	$k_{el}^{A \rightarrow B}, 10^{-3} \text{ cm s}^{-1}$	$k_{el}^{E \rightarrow F}, 10^{-3} \text{ cm s}^{-1}$
278	60.32	23.55
288	57.1	16.91
298	56.96	14.22
308	58.7	10.84
$\Delta G_{298}^\ddagger, \text{ kJ mol}^{-1}$	80 ± 2	84 ± 2

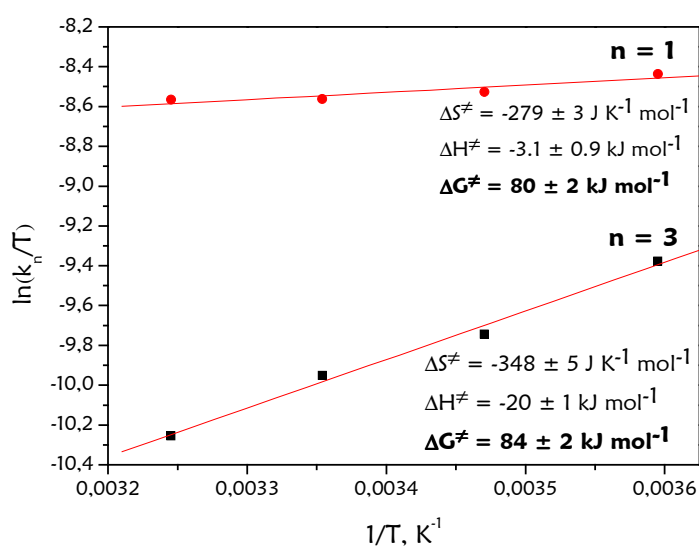


Figure 2.21. Eyring plots for the ET steps and calculated activation parameters (see data in Table 2.15)

2.2.4.6. Deuterium Kinetic Isotope Effect

The general assignment of our seven-coordinate redox couples to eq 2.12 would suggest that a large deuterium kinetic isotope effect ($\text{KIE} = k_{el}^{H_2O} / k_{el}^{D_2O}$) should be observed. The KIE can be regarded as a major manifestation of the concerted proton-electron transfer mechanism. Replacing the proton with a deuterium ion slows down the kinetics of charge transfer dramatically in some cases.³⁹ The isotope effect would be nonexistent in the stepwise model when proton transfer is not the rate limiting step. Thus, cyclic voltammetric measurements of electrode kinetics in D_2O at 25 °C were performed under exactly the same experimental conditions as in H_2O (see above). For the measurements in buffered media, sodium salts of MES and TAPS buffers were used and the pD of solutions was adjusted with $DClO_4$ and NaOD.

Figure 2.22 shows the cyclic voltammograms of the process $E \rightarrow B$ (pD 2.5, no buffer). The $E \rightarrow D$ (pD 4.7, MES buffer) and $G \rightarrow F$ (pD 7.6, TAPS buffer) processes are depicted in Figure 2.23. In the first case, a large isotope effect is evident in the

broadening of both the oxidative and reductive components of the wave. However, in the presence of both buffer components, though the changes in CVs are eminent, **inverse** isotope effects ($KIE < 1$) were observed. Table 2.16 summarizes heterogeneous rate constants in H_2O and D_2O and includes the corresponding KIE values.

Table 2.16. The heterogeneous rate constants measured in H_2O and D_2O and the value of KIE.

process (medium)	$k_{el}^{H_2O}$, $10^{-3} \text{ cm s}^{-1}$	$k_{el}^{D_2O}$, $10^{-3} \text{ cm s}^{-1}$	$k_{el}^{H_2O} / k_{el}^{D_2O}$
$E \rightarrow B$ (no buffer)	6.766	1.406	4.8
$E \rightarrow D$ (MES)	1.658	4.661	0.4
$G \rightarrow F$ (TAPS)	1.897	3.267	0.6

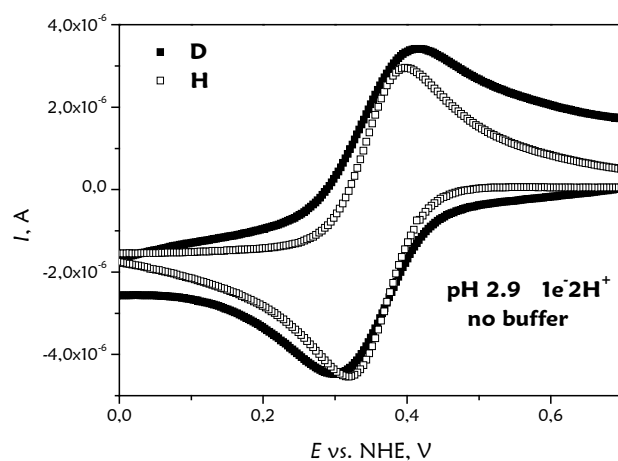


Figure 2.22. Deuterium kinetic isotope effect for $E \rightarrow B$ process measured in the absence of buffer.

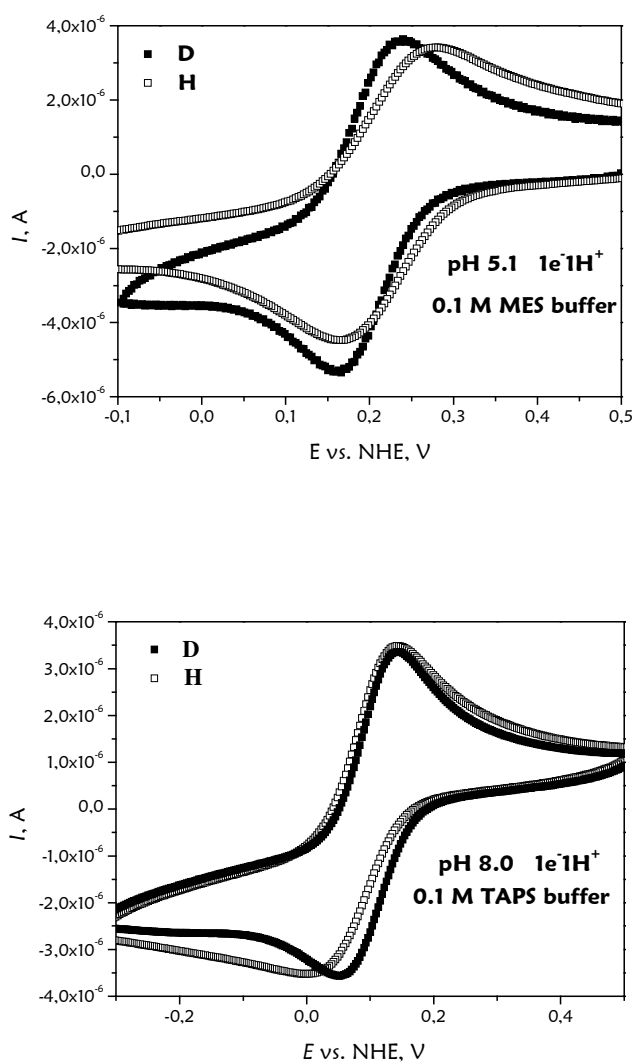
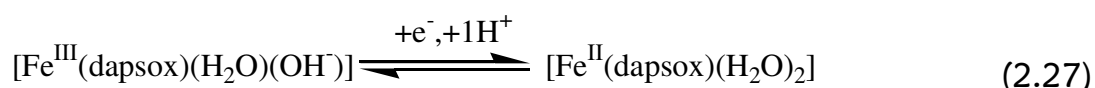
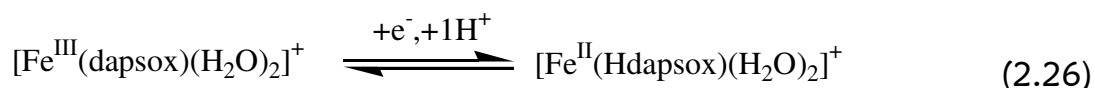
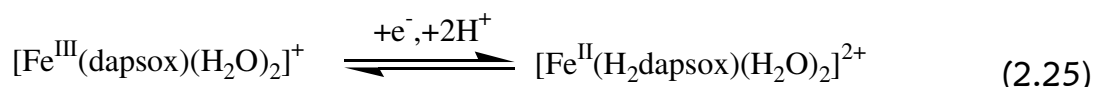


Figure 2.23. Inverse deuterium kinetic isotope effect for selected processes in the presence of buffer.

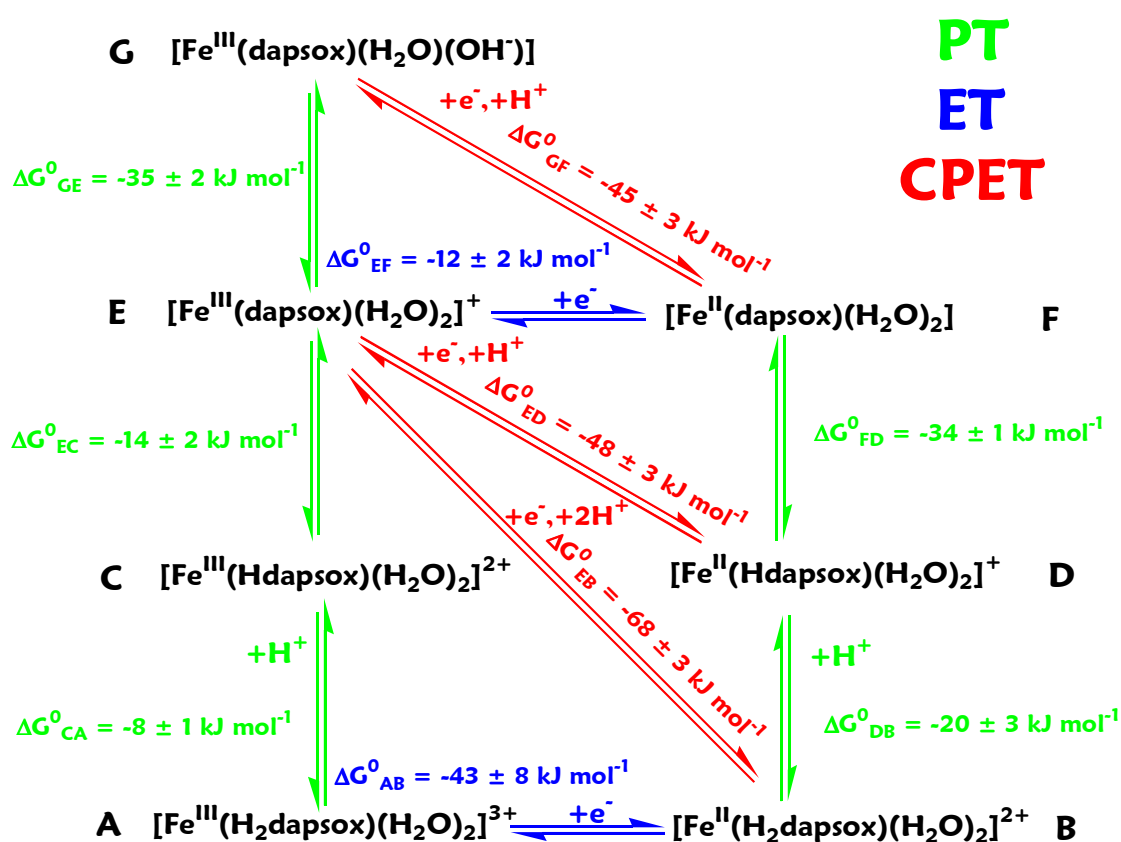
2.2.5. Overall Discussion

First, it should be pointed out that the analysis described below was done only for $Fe^{II/III}$ dapsox system. The $Fe^{II/III}$ dapsc case is more complicated since 3 protons per electron are transferred upon reduction of the complex in some cases, and no theoretical network exists for the analysis of such cases up to date. Subsequently, the measured activation parameters for both complexes will be discussed in short.

For the Fe^{II/III}dapsox system, at pH 2.9, pH 5.1 and pH 8.0 (at 25 °C) the following processes were measured and analyzed (eq 2.25–2.27, Schemes 2.7a–2.7c):



The reaction ascribed by eqs 2.25 can be analyzed using the six-member ladder scheme ($E \rightarrow B$, Scheme 2.7a); in contrast, processes described by eqs 2.26 and 2.27 can be analyzed using the square ($E \rightarrow D$ and $G \rightarrow F$, Scheme 2.7b) schemes. The latter reactions were followed in buffered media (0.1 M MES or TAPS), whereas no buffer was used at pH 2.9 (reaction according to eq 2.25).



Scheme 2.8. The overall thermodynamic scheme for the Fe^{II/III}dapsox system.

On the basis of the experimentally obtained results, it was possible to construct a complete thermodynamic scheme, which exposes all processes existing in aqueous solution of the seven-coordinate $\text{Fe}^{\text{II/III}}$ dapsox redox couple over the whole pH range (Scheme 2.8). The assignment of the species results from Figure 2.15. In Scheme 2.8, the electron-transfer (ET) steps are marked in blue, proton-transfer (PT) steps in green and the concerted proton-electron transfer (CPET) steps in red. The values of the driving forces (ΔG_{298}^0 at 25 °C) are given for all processes and given in the corresponding colors. The values of the driving forces for all PT steps are taken from Tables 2.5 and 2.6, but rewritten for the **protonation steps**. The possible rate-limiting steps in reactions (eqs 2.25–2.27, Scheme 2.8) can thus be carefully analyzed.

2.2.5.1. AEFB Reaction Cycle: $1e-2H^+$

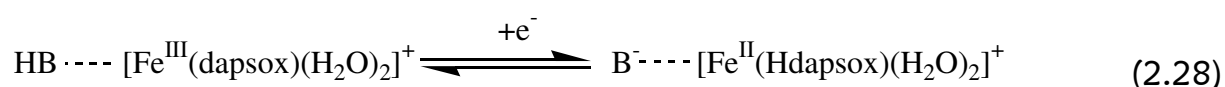
The net reaction step $E \rightarrow B$ (eq 2.25) is thermochemically downhill by 68 kJ mol⁻¹ (Table 2.7). Similarly, the initial electron transfer step $E \rightarrow F$ is downhill by 12 kJ mol⁻¹ (Table 2.8) and the initial proton transfer $E \rightarrow C \rightarrow A$ is downhill by 22 kJ mol⁻¹ (Table 2.5, Scheme 2.8). The energy difference between the ET and the net reaction steps $\Delta G_{\text{ET}}^0 - \Delta G_{\text{net}}^0 = \sim 56$ kJ mol⁻¹ leads to the conclusion that the PCET pathway is more favorable than ET, hence, the simultaneous transfer of two protons together with one electron is thermodynamically driven. The same conclusion can be drawn by taking into account the energy difference between the PT and net reaction steps (~ 46 kJ mol⁻¹).

The indication that the concerted transfer of protons and electron (CPET) is favored was revealed by the heterogeneous electrode kinetics as well, since a substantial deuterium kinetic isotope effect of $k_{el}^{H_2O} / k_{el}^{D_2O} = 4.8$ (Table 2.16, Figure 2.22) was observed. This value is quite high, but still in agreement with isotope effects of other proton-coupled electron transfer reactions.³⁹

2.2.5.2. CEFD Reaction Cycle: 1e⁻1H⁺

The initial proton transfer $E \rightarrow C$ is thermochemically downhill by 14 kJ mol⁻¹ (Scheme 2.8), the net as well as ET steps ($E \rightarrow D$: eq 2.26 and $E \rightarrow F$: eq 2.27, respectively) are downhill by 48 and 12 kJ mol⁻¹ (Tables 2.7 and 2.8). Still the paths involving initial PT or ET steps are less favorable because of the energy differences between PT and ET and the energy of the net reaction step (~ 34 - 36 kJ mol⁻¹). Also in this case it is reasonable to conclude that the CPET reaction step is more thermodynamically driven.

The observed kinetic isotope effect is quite large, but inverse, and is equal to 0.4 (Table 2.16, Figure 2.23). In general, the appearance of inverse isotope effects has been used as a criterion to distinguish rate-limiting proton transfer from proton transfer occurring in a pre-equilibrium prior to the rate-limiting step.³⁹ This effect can be caused by different speciations of the complex in D₂O and the presence of other species at certain pD values. The second reason for the inverse isotope effect can be the pre-equilibrium between the buffer component HB and the [Fe^{III}(dapsox)(H₂O)₂]⁺ complex species existing in solution at pH 5.1 at 25 °C. The description of the overall CPET reaction $E \rightarrow D$ can be given as follows (eq 2.28):

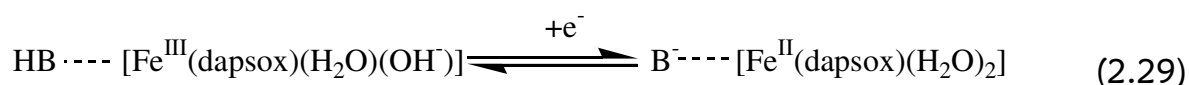


In our previous report⁵⁴ ([Section 2.1.4.7](#)) it was demonstrated that the change in reaction volumes of two similar seven-coordinate iron complex systems (Fe^{III}dapsox and Fe^{III}dapsc) and their change in charge upon electrochemical reduction can be correlated. The correlation was linear and had a slope close to that observed for a series of neutralization reactions studied before,⁷⁵ but smaller than that observed for redox processes in which no coupled proton-transfer reactions occur.⁷² This result manifests weaker electrostriction dependence, so that electrostriction effects for proton-coupled electron-transfer reactions in seven-coordinate iron complexes follow the trend observed for proton-transfer reactions. On this account the consideration of the possible initial ET or PT processes followed by the

proton/electron transfer step in a stepwise manner, seems not to be applicable to our system. Thus, the concerted proton-electron transfer most probably occurs.

2.2.5.3. EGF Reaction Cycle: $1e^-1H^+$

The ET reaction pathway is again less favorable in this case ($\Delta G_{\text{EF}}^0 = -12 \text{ kJ mol}^{-1}$). Taking Figure 2.15 into consideration, it is clear that the direct ET step $G \rightarrow H$ cannot occur in solution, discarding the possibility for the mechanism to follow an ET-PT stepwise pathway. The driving force for the CPET step is downhill by 45 kJ mol^{-1} ; hence, the occurrence of simultaneous proton and electron transfer is thermodynamically favored. The mechanism of this reaction cycle can be thought of as CPET. Also in this case the inverse kinetic isotope effect $k_{\text{el}}^{\text{H}_2\text{O}}/k_{\text{el}}^{\text{D}_2\text{O}} = 0.6$ was measured. This effect is smaller than in previous case, but still noticeable (Figure 2.23). Following the discussion above, a description of the overall CPET reaction $G \rightarrow F$ can be given (eq 2.29):



It can be concluded that in the two former cases the apparent buffer-assisted transfer of one proton upon electrochemical reduction of the corresponding $\text{Fe}^{\text{III}}\text{dapsox}$ species is observed. Thus, the buffer might behave as a proton donor and the seven-coordinate iron complex as a proton acceptor. In order to establish the buffer effect on such elementary reactions, further investigations will be required.

2.2.5.4. Activation Parameters for $\text{Fe}^{\text{II/III}}\text{dapsox}$ and $\text{Fe}^{\text{II/III}}\text{dapsc}$ systems

Tables 2.12 and 2.14 summarize values of ΔH^\ddagger , ΔS^\ddagger and ΔV^\ddagger for both systems. By plotting ΔH^\ddagger vs. ΔS^\ddagger (Figure 2.23), a sort of linear dependence was obtained, wherein ΔS^\ddagger is getting more negative as ΔH^\ddagger becomes smaller (enthalpy-entropy compensation).¹⁴²⁻¹⁴⁶ However, overlay of the heterogeneous rate constants for all the processes on a single Eyring plot shows that there is no point of common intersection within experimental error (Figure 2.24). Thus, the apparent enthalpy-

entropy compensation effect (Figure 2.23) does not represent an evidence of the existence of common mechanism.

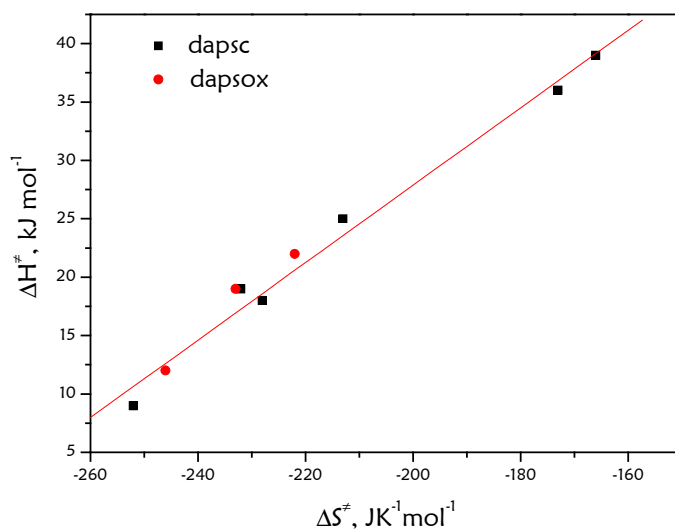


Figure 2.23. Enthalpy-entropy compensation plot for the seven-coordinate $\text{Fe}^{\text{II/III}}$ complexes.

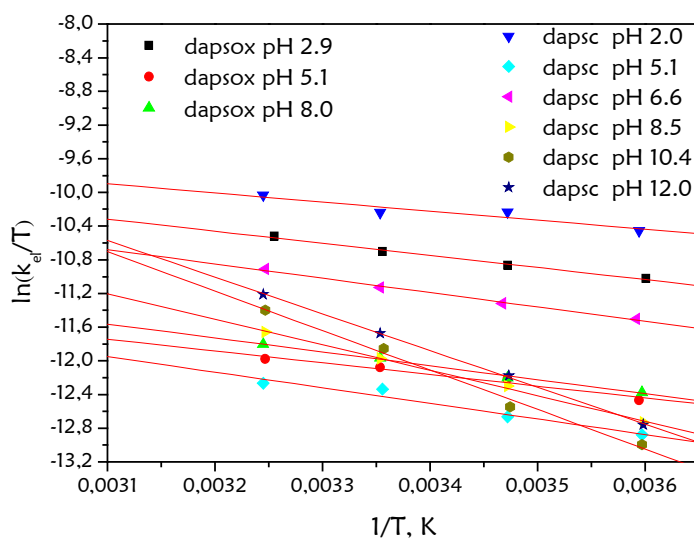


Figure 2.24. Overlay of all relevant Eyring plots for the seven-coordinate $\text{Fe}^{\text{II/III}}$ complexes.

From Figure 2.24 it can be observed that the processes at $\text{pH} < 8$ have the similar ΔH^\ddagger values (similar slopes of the Eyring plots), whereas the values of ΔS^\ddagger vary more prominently (different y-intercepts). The processes at $\text{pH} > 8$ are characterized by higher ΔH^\ddagger and less negative ΔS^\ddagger .

It appears that pH of the solution plays an important role in the mechanism of heterogeneous PCET, not being directly correlated to the accompanied structural changes of the complexes, but rather affecting solvent and surface phenomena. This can be illustrated by the similar pH dependencies of ΔH^\ddagger and ΔS^\ddagger (Figure 2.25).

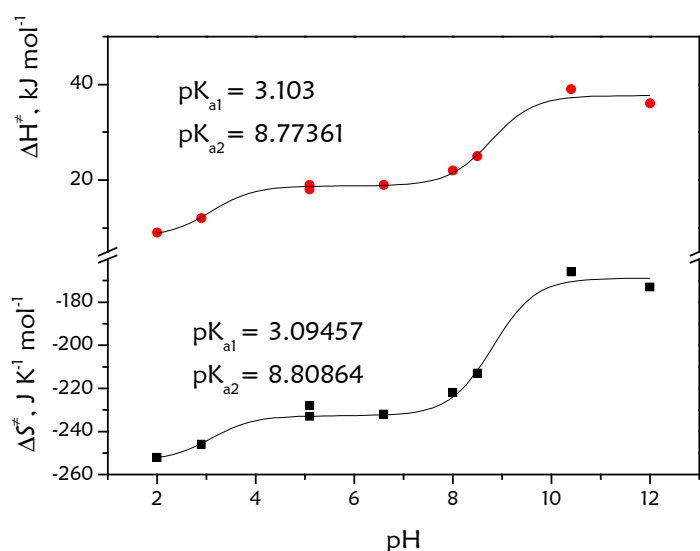


Figure 2.25. pH-dependent activation entropies ΔS^\ddagger and activation enthalpies ΔH^\ddagger of for the seven-coordinate $\text{Fe}^{\text{II/III}}$ complexes.

Different from ΔH^\ddagger and ΔS^\ddagger , the ΔV^\ddagger values do not show systematic dependence on pH . It seems that the activation volumes are affected not only by solvent and heterogeneous effects, but also reflected by electronic changes in the coordination sphere of the complexes. Therefore, a direct correlation between the ΔS^\ddagger and ΔV^\ddagger values cannot be found (Figure 2.26). However, comparing the PCET processes involving the same number of protons (b, c, e and a, f in Figure 2.26) it is possible to conclude that in cases where the protonation of coordinated OH^- is involved, the

corresponding ΔV^\ddagger are significantly more positive than in cases where the protonation of the pentadentate ligands occurs.

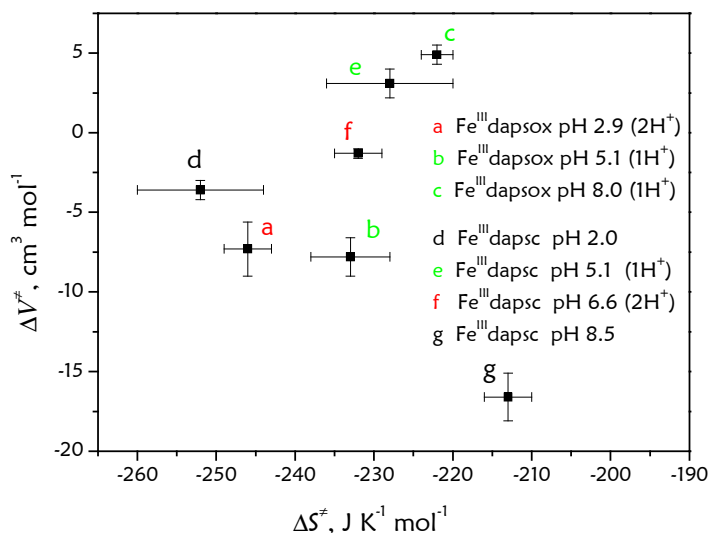


Figure 2.26. Correlation between the activation entropies ΔS^\ddagger and activation volumes ΔV^\ddagger for the seven-coordinate Fe^{II/III} complexes.

The obtained results demonstrate that the activation parameters based on the heterogeneous kinetic measurement do not directly reflect the mechanism of the elementary redox processes, since they are influenced by a variety of effects.

2.2.6. Conclusion

Results from temperature-dependent thermodynamic and kinetic electrochemical studies of all Fe^{II/III}dapsox complex species existing in aqueous solution over the pH range 1-12 in buffered and unbuffered media were reported. Temperature-dependent potentiometric titrations were carried out to clarify the thermodynamics of all PT steps. On the basis of the obtained temperature-dependent half-wave potentials ($E_{1/2}$) of each ET and PCET step, the driving forces were determined. As it can be seen, the thermodynamic bias towards the concerted proton-electron transfer mechanism is unambiguously established. Since the ability of the seven-coordinate Fe^{II} and Fe^{III} complexes of pentadentate H₂dapsox to catalytically decompose

superoxide radicals was recently demonstrated,⁵² it was important for us to show how intimately the connection between the acid-base equilibria and redox processes can be shown. This is the first time, where all PT, ET and CPET processes in Scheme 2.8 were experimentally followed and analyzed.

Since a major manifestation of the concerted proton-electron transfer is the existence of the deuterium kinetic isotope effect (KIE), heterogeneous rate constants (k_{el}) measured for the electrode reactions in H₂O and D₂O for the respective complex species were compared. The occurrence of a large isotope effect was detected at a pH where two protons are taken up on electrochemical reduction, hence, the concerted pathway for this process can be considered. If the measurements were performed in buffer, an inverse kinetic isotope effect appeared. The reason for this unusual effect can be caused by the pre-equilibrium between the buffer components and complex species at certain pHs. The understanding of the influence of buffer on such systems requires further investigations.

Relying on the latest evidence that the concerted proton-electron transfer processes might be present in the natural SOD enzymes,⁴³ the experimentally obtained results for their mimetics in this section were analyzed mechanistically to rule out other possible reaction pathways. The results are important in terms of the action mechanism in superoxide dismutase mimetics.

3. A Seven-Coordinate Iron Complex as Ditopic Receptor for Lithium Salts: Study of Host-Guest Interactions and Substitution Behavior.

3.1. General Remark

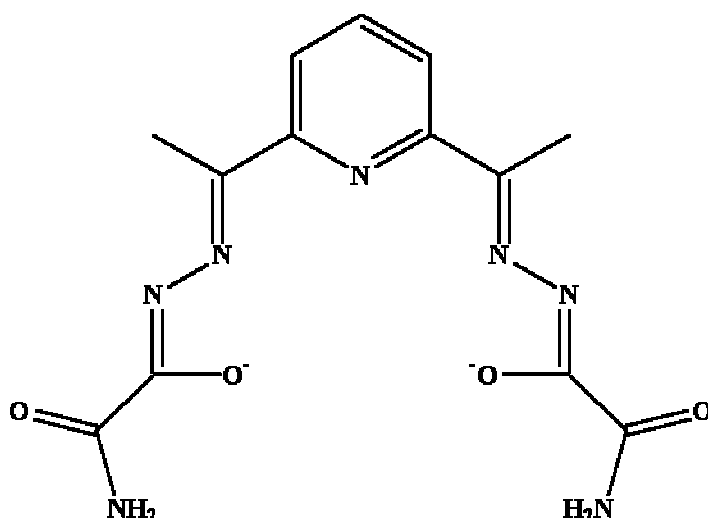
The work presented below has been published as full paper¹⁴⁷:

Sarauli, D.; Popova, V.; Zahl, A.; Puchta, R.; Ivanović-Burmazović, I. *Inorganic Chemistry* **2007**, *46*, 7848-7860.

3.2. Introduction

The solution properties and mechanistic behavior of seven-coordinate 3d metal complexes are still unrevealed research areas. These complexes are especially interesting as excellent low molecular weight catalysts for superoxide dismutation, providing important therapeutic applications.^{45, 46, 48} Although the best SOD mimetics known to date are seven-coordinate complexes of Mn^{II} with macrocyclic pentadentate ligands, iron SOD mimetics would also be desirable because of their higher kinetic and thermodynamic stability than manganese complexes.⁴⁷

To gain an understanding of the solution chemistry of the iron seven-coordinate complexes, the substitution behavior and proton-coupled electron transfer reactions of the pentagonal-bipyramidal (PBP) Fe^{III} complex, [Fe(dapsox)(H₂O)₂]⁺ (H₂dapsox = 2,6-diacetylpyridine-bis(semioxamazide)),⁵³ with an anionic planar pentadentate ligand in the equatorial plane (Scheme 3.1), were systematically studied.^{54, 55, 148}



Scheme 3.1

Mechanistic information on the two-step displacement of the trans coordinated solvent molecules by the monodentate monoanionic thiocyanate ligand were obtained in the case of H₂O, MeOH, EtOH and DMSO as axial ligands.^{55, 148} The latter solvent was selected because kinetic experiments with the superoxide radical anion, especially with more concentrated solutions (in the millimolar range), require the use of aprotic solvents and the mixing of potassium superoxide solutions with aqueous or alcoholic solutions of the studied complexes for kinetic measurements at ambient and low temperatures, respectively. In the DMSO/CH₃CN (29/71) mixture, it is possible to perform low-temperature kinetic measurements down to -53 °C.^{149, 150} In this respect, it was important to understand the substitution behavior of [Fe(dapsox)(H₂O)₂]ClO₄ in CH₃CN solution as well.

In general, kinetic measurements should be performed at constant ionic strength, requiring the use of so-called “innocent” salts as supporting electrolytes, which do not coordinate to the metal center in solution. Because of the good solubility, tetraalkylammonium and some lithium salts are suitable as supporting electrolytes in aprotic solvents like DMSO and CH₃CN. However, added salts can exert strong effects on the rates of reaction between charged species in solution, affecting the solvation of inorganic complexes.^{151, 152} The interaction via hydrogen bonds should also be taken into consideration, especially in aprotic solvents where these

interactions are more prominent.¹⁵³⁻¹⁵⁶ The electrostatic interactions and hydrogen-bonding also play an important role in the host–guest chemistry, in designing specific receptors for small ions, and in generating dynamic combinatorial libraries (DCL) as a new strategy for identifying receptors of high affinity for the respective target.¹⁵⁷ Amide-group containing receptors are very often used for anion recognition,¹⁵⁸⁻¹⁶¹ whereas hydrazone chemistry was involved in creating DCLs and the discovery of receptors for cations, like ammonium,¹⁶² Co^{III} ¹⁶³ and Li^+ .¹⁶⁴ Receptors for Li^+ are of special interest since Li^+ is the smallest metal cation and has clinical, pharmacological, and biochemical importance.¹⁶⁵⁻¹⁷⁰

In the light of these aspects, it was of importance to investigate whether the nature of added electrolyte can exert a significant effect on substitution kinetics of our seven-coordinate Fe^{III} complex in CH_3CN solution, especially due to the fact that our dapsox²⁻ ligand possesses two amide and two hydrazone functional groups at the same time. Thus, from a structural point of view, our seven-coordinate iron complex can potentially be a ditopic receptor, capable of binding anions and small cations simultaneously.

In this Section the results from electrochemical, ^7Li and ^{19}F NMR, and DFT studies of the host–guest interactions between the seven-coordinate $[\text{Fe}(\text{dapsox})(\text{CH}_3\text{CN})_2]^+$ complex and different lithium salts in CH_3CN are reported. Kinetic and spectrophotometric studies on the substitution behavior of this PBP Fe^{III} complex in the presence and absence of lithium ions in acetonitrile solutions have also been reported. Since seven-coordinate pentagonal-bipyramidal 3d metal complexes with planar pentadentate ligands are known to be synthetic SOD enzymes,^{45, 46, 48} simulation of an enzymatic active site, which could bind small metal cations and in that way enhance binding of superoxide, is of importance.

3.3. Experimental Section

3.3.1. Materials

The solvents acetonitrile (Roth, dry, $\geq 99.9\%$, $\leq 0.001\%$ H₂O), DMSO (Acros Organics, $\geq 99.9\%$, $\leq 0.1\%$ H₂O) and methanol (Roth, $\geq 99.9\%$, $\leq 0.005\%$ H₂O), as well as the salts NaSCN (Aldrich, 96%), LiOTf (Aldrich, 96%), LiClO₄ (Aldrich, 98%), LiBF₄ (Aldrich, 98%), LiPF₆ (Acros Organics, 98%), NaClO₄ (Acros Organics, 99+%) and all tetrabutylammonium (TBA) salts (Fluka, $\geq 99\%$, puriss electrochemical grade) were used as received without further purification. The water content in solutions was determined by Karl Fischer titrations. [Fe(dapsox)(H₂O)₂]ClO₄ was prepared and characterized previously.^{53, 63} The [Fe(dapsox)(NCS)₂]⁻ species was prepared in situ by adding a minimum 100-fold excess of NaSCN to the acetonitrile solution of [Fe(dapsox)(H₂O)₂]ClO₄.

3.3.2. Kinetic Measurements

All data were obtained by recording time-resolved UV/vis spectra using a modified Bio-Logic stopped-flow module μ SFM-20 combined with a Huber CC90 thermostat ($\pm 0.1^\circ$) and equipped with a J & M TIDAS high-speed diode-array spectrometer with combined deuterium and tungsten lamps (200-1015 nm wavelength range). Data were analyzed using the integrated Bio-Kine software, version 4.23, and the Specfit/32 program. At least 10 kinetic runs were recorded under all conditions, and the reported rate constants represent the mean values. All kinetic measurements were carried out under pseudo-first-order conditions, i.e., the substituent concentration was in a large excess (concentrations of iron complex were 5×10^{-5} M). The reactions were studied at constant ionic strength (0.2 M). Values of ΔH^\ddagger and ΔS^\ddagger were calculated from the slopes and intercepts of plots of $\ln(k/T)$ versus $1/T$, respectively.

3.3.3. Spectrophotometric Titrations

UV/vis spectra were recorded on a Hewlett-Packard 8542A spectrophotometer at room temperature. Solutions of $[\text{Fe}(\text{dapsox})(\text{CH}_3\text{CN})_2]^+$ and $[\text{Fe}(\text{dapsox})(\text{NCS})_2]^-$ (0.05 and 0.1 mM) in acetonitrile were placed in a 1.0 cm path length cuvette in the thermostated cell block of a spectrophotometer for 10–15 minutes. These solutions were titrated by addition of small aliquots of concentrated stock solutions of substrates (NaSCN , LiOTf , LiBF_4 and LiPF_6) in CH_3CN . The spectra were recorded after equilibration for 10 minutes.

3.3.4. Electrochemical Measurements

Cyclic (CV) and differential pulse (DPV) voltammetry measurements were performed with an Autolab PGSTAT 30 device (Eco Chemie). All measurements were conducted under N_2 in a jacketed, one-compartment cell with Au disk working electrode (geometric area: 0.07 cm^2) (Metrohm), a platinum wire counter electrode (Metrohm) and a Ag wire pseudo-reference electrode. The working electrode surface was polished with $0.05\text{-}\mu\text{m}$ alumina, sonicated in water, and air-dried immediately before use. Various Bu_4NA ($\text{A} = \text{PF}_6^-$, BF_4^- , ClO_4^- , OTf^-) salts (0.1 M) were used as electrolytes. The sweep rate was 50 mV/s . No IR compensation was applied. The stoichiometry of each electron-transfer was established by wave-height comparisons with known one-electron redox processes. O_2 was removed from the electrolyte solution by bubbling N_2 through the solvent for several minutes prior to making the measurement. A N_2 atmosphere was continuously maintained above the solution while the experiments were in progress. Temperature was controlled by using a double-jacketed cell and a thermostat with water bath at $25 \text{ }^\circ\text{C}$.

In order to improve the solubility of the complex, solutions were prepared in dry CH_3CN containing a maximum of 0.1 % DMSO. To determine the equilibrium associated with the redox-dependent binding, titration measurements were run in 0.1 M Bu_4NA electrolyte solutions, using the seven-coordinate Fe^{III} complex as a receptor and different lithium and/or tetrabutylammonium salts as substrates.

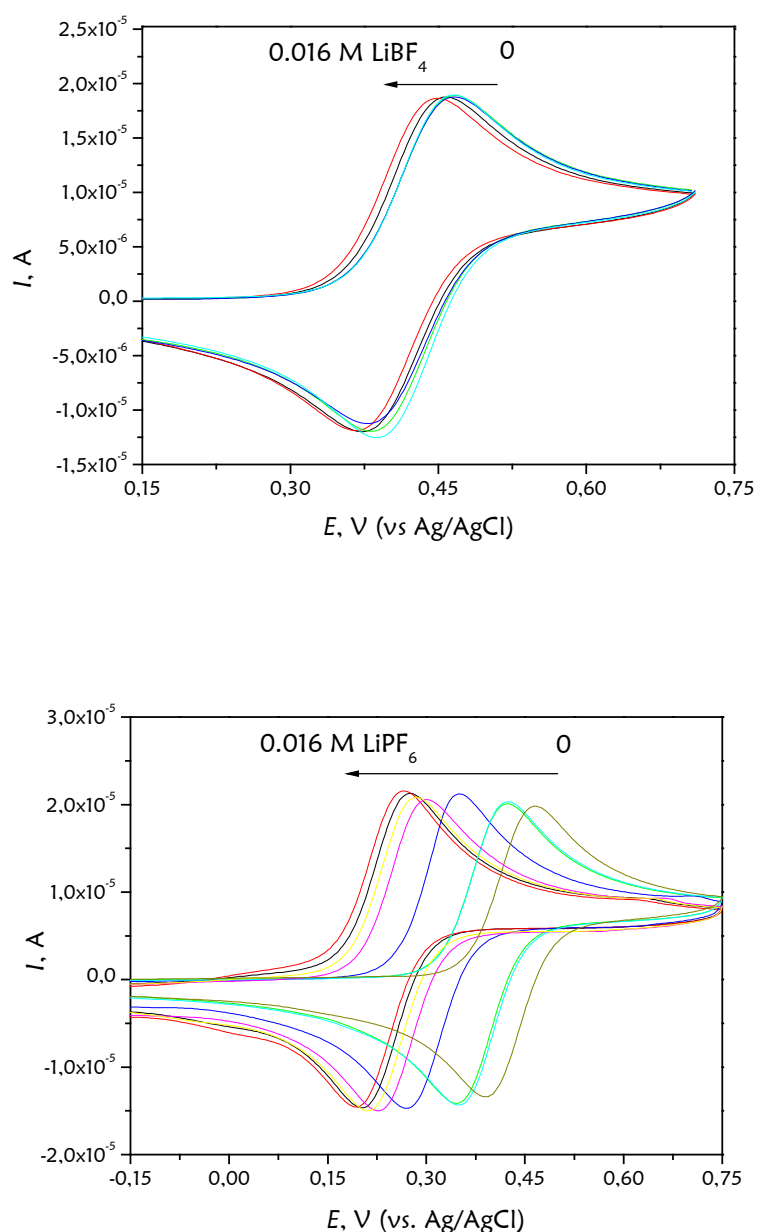


Figure 3.1 Cyclic voltammograms of Fc/Fc⁺ couple in the presence of (above) LiBF₄ (up to 0.016 M) and (below) LiPF₆ (up to 0.016 M) measured against the Ag/AgCl reference electrode. Upon addition of lithium salts, a pronounced shift of the half-wave potential $E_{1/2}$ towards cathodic potential was observed.

Experimentally, aliquots of concentrated lithium/tetrabutylammonium salt solutions were added incrementally to a 20 ml sample of the 1 mM iron complex, and cyclic voltammograms were run after each addition. Potentials are cited versus a Ag/AgCl

electrode. The use of ferrocene as internal standard is not recommended, since its redox potential depends very much on the concentration of lithium salts present in the CH₃CN solution ($\Delta E = 30$ mV in the presence of 16 mM LiBF₄ and $\Delta E = 300$ mV in the presence of 16 mM LiPF₆, Figure 3.1).

3.3.5. Nuclear Magnetic Resonance Spectrometry

The NMR measurements were conducted on a Bruker Avance DRX 400WB spectrometer using a 5 mm broadband probe. ¹⁹F NMR spectra were recorded on a Bruker Avance DPX-300 spectrometer at 282.4 Hz. The solutions to be studied were placed in NMR tubes, and the solution of external standard (CF₂Br₂ in CD₃CN) in a concentric capillary was used for the field/frequency deuterium lock. All measurements were run at room temperature. The chemical shifts were related to CF₂Br₂ ($\delta_F = 7$ ppm vs. CFCI₃). ⁷Li NMR spectra were recorded at 155.5 MHz with a spectral width of 620 Hz and an acquisition time of 13 s. All systems were referenced to the free Li⁺ salt (LiOTf) in DMF (external standard). Measurements were run at room temperature.

⁷Li T₁ relaxation measurements were performed using the inversion recovery pulse sequence (D₁, 180°, τ , 90°). At least fifteen τ values were used for each spin–lattice relaxation time (T₁) determination, and an interpulse delay of at least 10 times the T₁ value was used before repeating the pulse sequence. The observed T₁ values at different Li⁺ concentrations were used to calculate the apparent binding constants K^{III} to the seven-coordinate [Fe(dapsox)(CH₃CN)₂]⁺ complex. The relaxation measurements were accompanied by a 2–10% uncertainty.

3.3.6. Quantum Chemical Methods.

B3LYP/LANL2DZp hybrid density functional calculations were performed, i.e., with pseudo-potentials on the heavy elements and the valence basis set augmented by polarization functions.¹⁷¹⁻¹⁷⁶ The resulting structures were characterized as minima by computation of vibrational frequencies and the wave functions were tested for stability. The GAUSSIAN suite of programs was used.¹⁷⁷

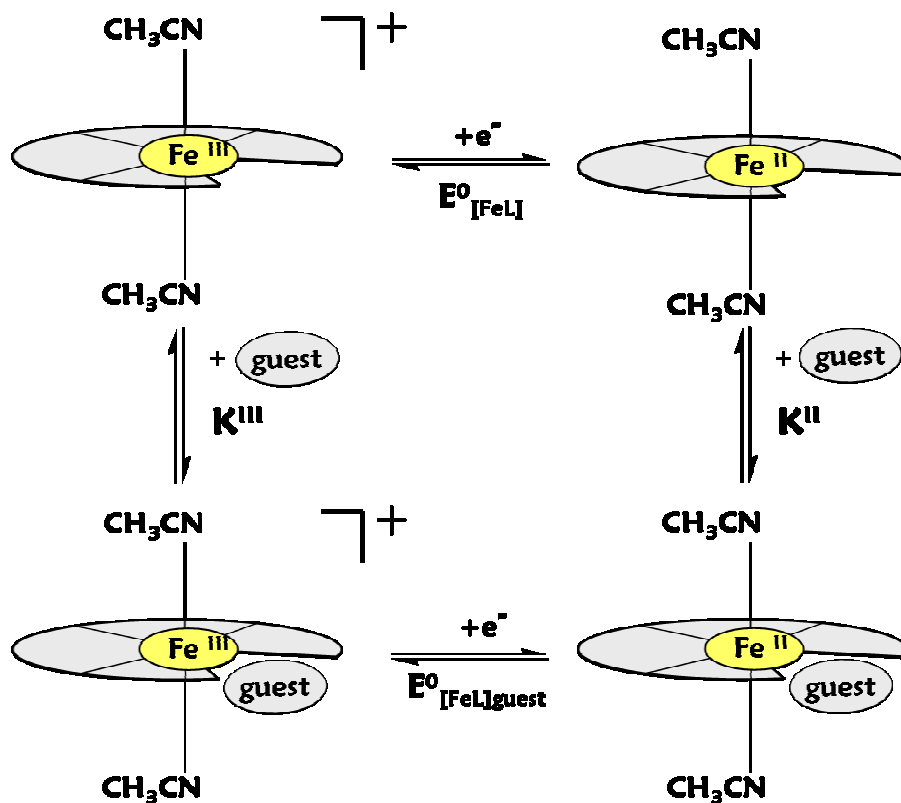
3.4. Results and Discussion

3.4.1. Electrochemical Studies

Cyclic voltammetry measurements of the seven-coordinate $[\text{Fe}(\text{dapsox})(\text{CH}_3\text{CN})_2]^+$ complex in the presence of different tetrabutylammonium (Bu_4^+N) and lithium salts in CH_3CN afford a simple and effective way for estimating the communication between the redox-active iron center and the binding sites of studied cation–anion pairs as potential guests. If present, an interaction between the seven-coordinate iron complex in both its oxidation states (Fe^{III} and Fe^{II}) and the ions in its substrate binding sites would result in a shift of the $[\text{Fe}(\text{dapsox})(\text{CH}_3\text{CN})_2]^{0/+}$ couple redox potential upon increase of the salt concentration.¹⁷⁸ For the electrochemical guest binding titrations, the equilibria can be represented by a redox square (Scheme 3.2), and the interaction can be quantified by determining the apparent guest binding constant according to eq 3.1,^{151, 178, 179} where ΔE is a shift in the host redox potential as a function of guest concentration and K^{II} and K^{III} correspond to the 1:1 host/guest complex in the divalent and trivalent forms of the receptor, respectively.

$$\Delta E = \frac{RT}{F} \ln \left[\frac{1 + K^{\text{II}}[\text{guest}]}{1 + K^{\text{III}}[\text{guest}]} \right] \quad (3.1)$$

However, no increase or decrease in the half wave potential ($E_{1/2}$) of the $[\text{Fe}(\text{dapsox})(\text{CH}_3\text{CN})_2]^{0/+}$ couple (1 mM) was observed when concentrations of Bu_4^+NA^- ($\text{A}^- = \text{PF}_6^-, \text{BF}_4^-, \text{ClO}_4^-, \text{OTf}^-$) were varied from 1 to 50 mM in CH_3CN solution (Figure 3.2). Although in the crystal structure of $[\text{Fe}(\text{dapsox})(\text{H}_2\text{O})_2]\text{ClO}_4$ the charge assisted hydrogen bonding interactions between the tweezerlike $[\text{Fe}(\text{dapsox})(\text{H}_2\text{O})_2]^+$ cation and the ClO_4^- anion have been observed,⁵³ this interaction, based on the performed electrochemical titrations, seems not to be strong enough to be observed in solution.



Scheme 3.2.

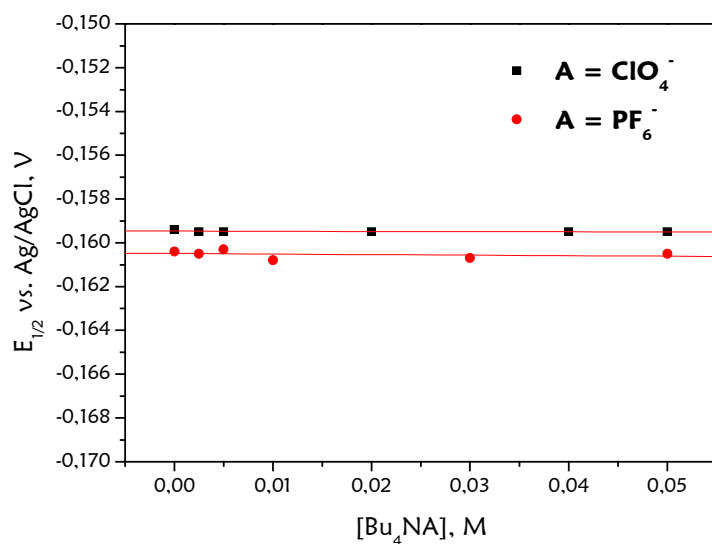


Figure 3.2. Half-wave potential $E_{1/2}$ of $[\text{Fe}(\text{dapsox})(\text{CH}_3\text{CN})_2]^{0/+}$ couple (1 mM) in CH_3CN + 0.1% DMSO at 25 °C in the presence of different amounts (up to 50 mM) of Bu_4NA (A = ClO_4^- , PF_6^-) salts. The solid lines represent linear fits.

Table 3.1. The $E_{1/2}$ values of $[\text{Fe}(\text{dapsox})(\text{CH}_3\text{CN})_2]^{0/+}$ couple (1 mM) upon addition of different lithium salt concentrations (see Figure 3.3).

LiOTf		LiClO ₄		LiBF ₄	
Concentration, mM	$E_{1/2}$ vs. Ag/AgCl, mV	Concentration, mM	$E_{1/2}$ vs. Ag/AgCl, mV	Concentration, mM	$E_{1/2}$ vs. Ag/AgCl, mV
0	-158 ± 0.6	0	-158 ± 0.8	0	-158 ± 0.7
0.25	-139 ± 0.6	0.186	-140 ± 0.8	0.25	-151 ± 0.5
0.5	-128 ± 0.5	0.797	-125 ± 0.9	0.5	-127 ± 0.6
0.74	-123 ± 0.5	1.5	-118 ± 0.8	0.74	-121 ± 0.5
1	-118 ± 0.6	2.5	-110 ± 0.8	1	-112 ± 0.6
2	-108 ± 0.4	5	-103 ± 0.6	2	-109 ± 0.7
3	-98 ± 0.5	7.5	-99 ± 0.5	3	-104 ± 0.6
4	-93 ± 0.6	10	-98 ± 0.6	4	-103 ± 0.6
5	-89 ± 0.4	12.5	-96 ± 0.6	5	-101 ± 0.7

LiOTf		LiClO ₄		LiBF ₄	
					0.7
6	-85 ± 0.5	15	-95 ± 0.7	10	-97 ± 0.8
7	-84 ± 0.5	17.5	-94 ± 0.6	15	-98 ± 0.6
9.8	-83 ± 0.5	20	-94 ± 0.6	20	-95 ± 0.7
14.5	-78 ± 0.6	25	-93 ± 0.8	25	-94 ± 0.6
19	-72 ± 0.6			30	-94 ± 0.6

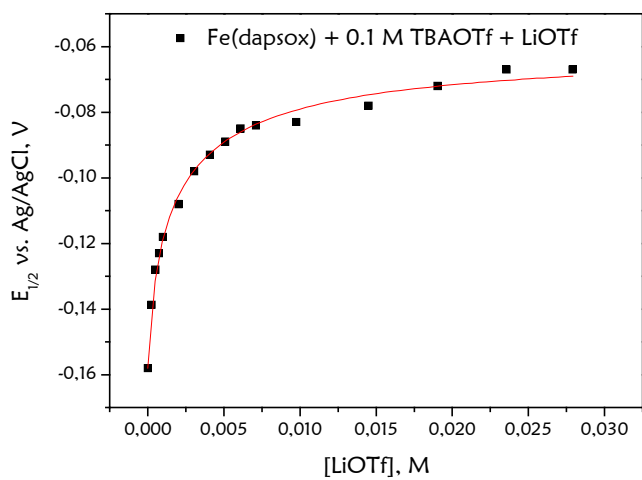
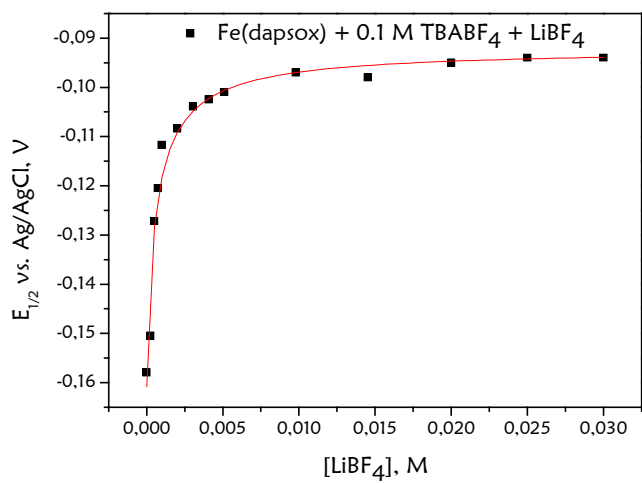
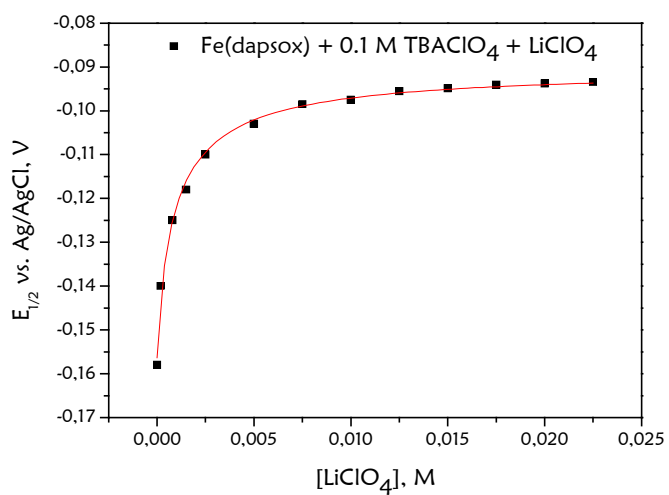


Figure 3.3. Plot of $E_{1/2}$ versus lithium salt concentration $[\text{Li}^+\text{A}^-]$ ($\text{A} = \text{OTf}^-, \text{ClO}_4^-, \text{BF}_4^-$); $[\text{Fe}(\text{dapsox})(\text{CH}_3\text{CN})_2]^+ = 1 \text{ mM}$, $25 \text{ }^\circ\text{C}$, $E_{1/2}$ vs. Ag/AgCl electrode. The corresponding Bu_4^+NA^- salts (0.1 M) were used as supporting electrolytes. Solid curves represent nonlinear least-squares fitting of the data to eq 3.1.

Lithium salts differ from tetrabutylammonium salts because they increase the solubility of $[\text{Fe}(\text{dapsox})(\text{H}_2\text{O})_2]\text{ClO}_4$ and significantly shift the half-wave potential of $[\text{Fe}(\text{dapsox})(\text{CH}_3\text{CN})_2]^{0/+}$ in CH_3CN . The addition of LiOTf , LiClO_4 or LiBF_4 to the electrolyte solution of $[\text{Fe}(\text{dapsox})(\text{CH}_3\text{CN})_2]^+$ (ionic strength of 0.1 M was kept constant) led to a progressive positive shift in the $E_{1/2}$ (one-wave behavior). The maximum shift in the half-wave potential is reached in the presence of an excess of guest species (Figure 3.3, Table 3.1). Cyclic and differential pulse voltammograms obtained during electrochemical titrations of $[\text{Fe}(\text{dapsox})(\text{CH}_3\text{CN})_2]^+$ (Figure 3.4) show the presence of a single reversible redox couple that shifts anodically with added lithium salt, indicating weak binding.^{153, 179, 180} The difference in diffusion coefficients of $[\text{Fe}(\text{dapsox})(\text{CH}_3\text{CN})_2]^+$ and its lithium salt adduct causes the difference in the current intensity observed in Figure 3.4.

The values of K^{II} are quite high ($\sim 10^4$) and are more than 1 order of magnitude larger than K^{III} . This is consistent with the observed positive shift of $E_{1/2}$, confirming that the reduced state of the receptor is stabilized upon complexation with lithium salts.^{153, 180, 181} The K^{II} values are less sensitive to the nature of the counter anion than the K^{III} values, suggesting that more prominent interaction with the anion exists in the case of the Fe^{III} form of the complex. Somewhat higher apparent binding constants are observed for LiBF_4 , where the strongest hydrogen- binding interactions between the anion and amide $-\text{NH}_2$ groups are to be expected. Consequently, stronger anion binding results in a smaller shift of $E_{1/2}$, since, opposite from Li^+ coordination, it increases the electron density around the metal center.

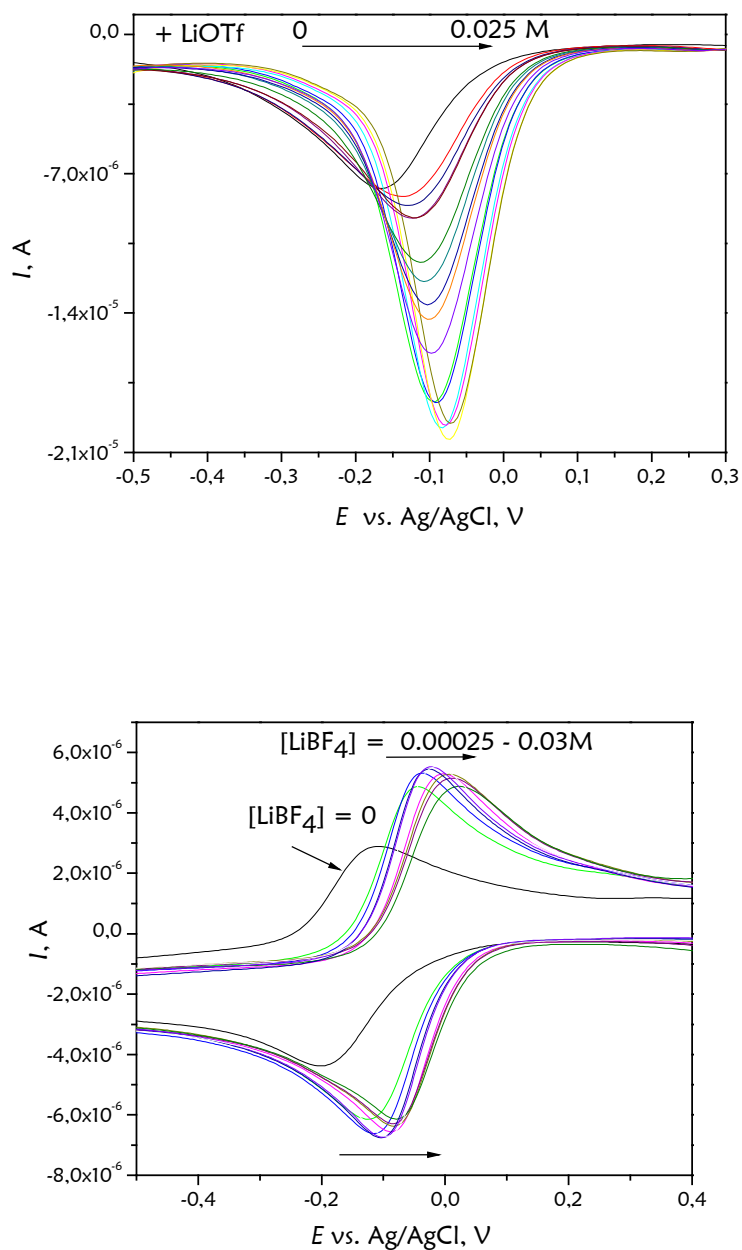


Figure 3.4. Typical electrochemical response of $[\text{Fe}(\text{dapsox})(\text{CH}_3\text{CN})_2]^{0/+}$ (1 mM) upon addition of increasing amounts of (above) LiOTf (differential pulse voltammograms) and (below) LiBF₄ (cyclic voltammograms) using corresponding Bu₄NA salts (0.1 M) as electrolytes.

Table 3.2. Apparent Binding Constants for the Complexation of Li^+A^- Salts in CH_3CN by $[\text{Fe}(\text{dapsox})(\text{CH}_3\text{CN})_2]$ (K^{II}) and $[\text{Fe}(\text{dapsox})(\text{CH}_3\text{CN})_2]^+$ (K^{III}).

Apparent Binding Constants, M^{-1}	Solvent				
	CH ₃ CN			CH ₃ OH	
	Li ⁺ OTf ⁻	Li ⁺ ClO ₄ ⁻	Li ⁺ BF ₄ ⁻	Na ⁺ ClO ₄ ⁻	Li ⁺ BF ₄ ⁻
K^{II} (CV) ^a	3754 ± 418	4004 ± 402	6616 ± 1812	2690 ± 400	2529 ± 301
K^{III} (CV) ^a	90 ± 11	309 ± 28	458 ± 102	< 0.1 ^b	< 0.1 ^b
K^{III} (⁷ Li NMR) ^c	203 ± 32				
K^{III} (kinetics) ^d	49 ± 10				
K^{III} (UV/vis) ^c	165 ± 15				

^a At 25 °C in 0.1 M Bu₄NA. ^b Too small to determine. ^c At 25 °C with no supporting electrolyte. ^d At -15 °C in 0.2 M Bu₄NA.

The electrochemical titrations with NaClO₄ in CH₃CN and with LiBF₄ in MeOH were also performed in order to test the cation and solvent variation effects (Table 3.2). In both cases the K^{III} value was too small ($K^{\text{III}} < 10^{-1} \text{ M}^{-1}$) to be determined,¹⁸⁰ showing that the interactions between the Fe^{III} form of the complex and guest salts are very weak under those conditions. Comparison of the apparent binding constants K^{II} for LiClO₄ (4004 ± 402 M⁻¹) and NaClO₄ (2690 ± 400 M⁻¹) in CH₃CN (Table 3.2) leads to the conclusion that the complex exhibits modest Li⁺ selectivity. Similar complexation selectivity was observed for several redox-active ferrocene crown-ethers.¹⁸² Polarity of the solvent also plays an important role.^{183, 184} Therefore, in more polar MeOH, the interaction of the complex with LiBF₄ is weaker than in CH₃CN resulting in the smaller apparent binding constants K^{II} and K^{III} (Table 3.2).

3.4.2. Solution Behavior in the Presence of LiPF₆

The electrochemical titration was also performed with LiPF₆. However, lithium catalyzed hydrolysis of PF₆⁻ causes the appearance of additional fluorine-containing anionic species and HF,¹⁸⁵ which makes solution chemistry more complex. Immediately upon addition of small aliquots of 0.4 M LiPF₆ in CH₃CN (complex/Li⁺ = 4:1 molar ratio) two new redox waves were observed (Figure 3.5): the intense one (b) with negatively shifted $E_{1/2}$ ($\Delta E_{1/2} = -130$ mV) and the one of lower intensity (c) with positively shifted $E_{1/2}$ ($\Delta E_{1/2} = +132$ mV) relative to the original redox couple. The appearance of two redox waves and the negative shift in redox potential upon addition of lithium salt are unique observations. By increasing the lithium concentration, the intensity of wave (b) decreases and that of (c) increases (Figure 3.5).

To obtain more information about the species present in solution, ¹⁹F NMR measurements were performed. In the ¹⁹F NMR spectrum of Bu₄NPF₆ in acetonitrile, only one 1:1 doublet at $\delta_F = -69.8$ ppm, with a ³¹P–¹⁹F coupling constant $J(P,F) = 707$ Hz, is observed (Figure 3.6a), which is typical for PF₆⁻.¹⁸⁵ However, the ¹⁹F spectrum of LiPF₆ in CH₃CN consists of two doublets with chemical shifts (a) $\delta_F = -69.8$ ppm [$J(P,F) = 707$ Hz] and (b) $\delta_F = -81.6$ ppm [$J(P,F) = 959$ Hz], as well as the singlet (c) with $\delta_F = -148.6$ ppm (Figure 3.6b). The major low-field doublet (a) is assigned to PF₆⁻, whereas the doublet (b) is unambiguously assigned to the PO₂F₂⁻ ion, which is the product of partial hydrolysis of PF₆⁻ in CH₃CN, accelerated by the presence of Li⁺ ions in solution.¹⁸⁵ The singlet (c) is characteristic for HF, which is also consistent with the hydrolysis processes observed in the presence of Li⁺.¹⁸⁵ When the complex (1 mM) was added to the solutions containing 0.1 M NBu₄PF₆ and different concentrations of LiPF₆, the downfield shift of the doublet (b) $\delta_F = -78.6$ ppm [$J(P,F) = 946$ Hz] and the appearance of a new one (d), $\delta_F = -72.1$ ppm [$J(P,F) = 920$ Hz] could be observed (Figure 3.7). The new doublet (d) corresponds to the PO₃F²⁻ anion.¹⁸⁵

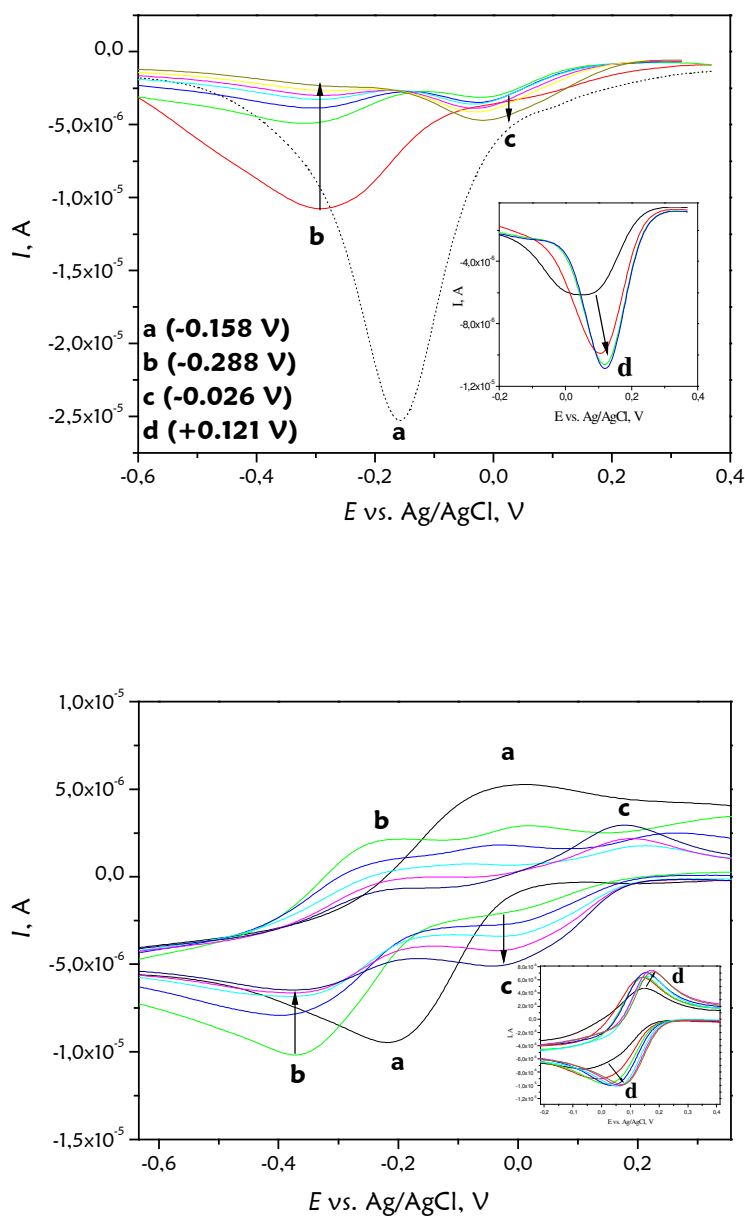


Figure 3.5. DPV (above) and CV (below) electrochemical response of $[\text{Fe}(\text{dapsox})(\text{CH}_3\text{CN})_2]^{0/+}$ (1 mM) upon addition of increasing amounts of LiPF_6 . The wave (a) is assigned to the $[\text{Fe}(\text{dapsox})(\text{CH}_3\text{CN})_2]^+$ in the absence of lithium salt. The waves (b) and (c) appear in acetonitrile solution of complex after addition of LiPF_6 (up to 0.0019 M). The wave (d) (Insets) appears after further addition of LiPF_6 (0.0019 M – 0.019 M).

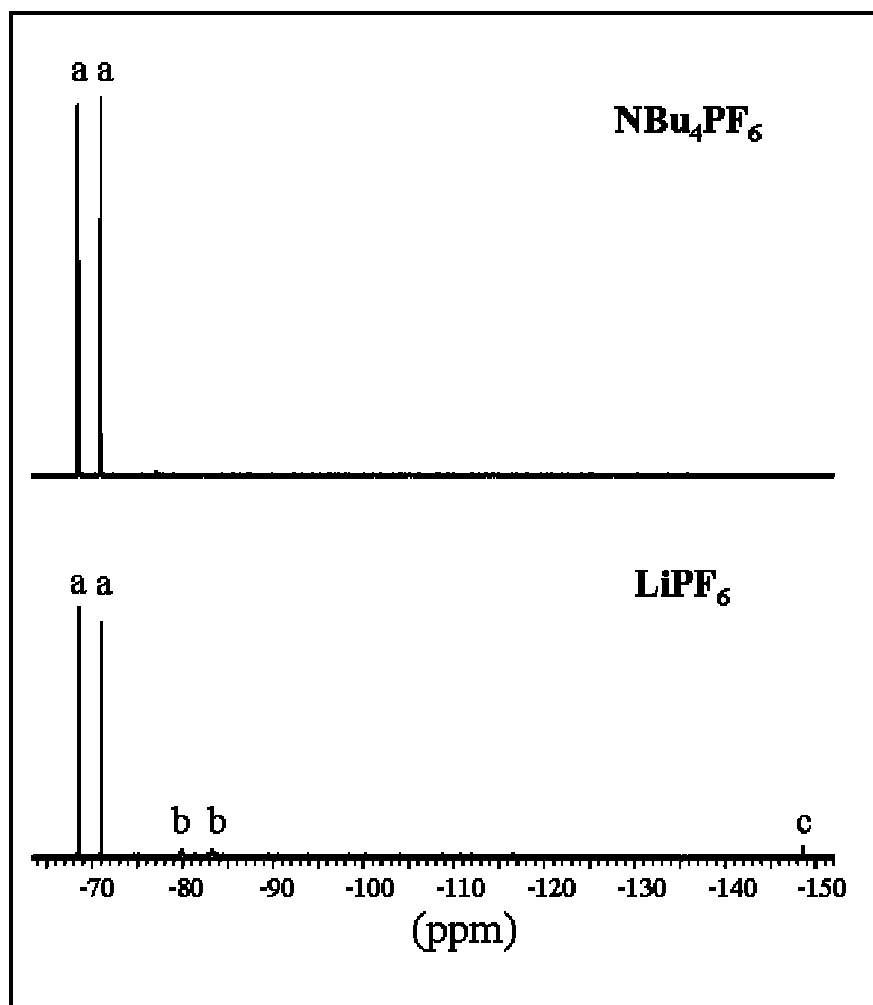


Figure 3.6. Typical ^{19}F NMR spectra of CH_3CN solution, containing 0.2 M Bu_4NPF_6 and 0.2 M LiPF_6 . Signals (a) are assigned to PF_6^- . Signals (b) and (c) belong to PO_2F_2^- and HF, respectively.

The observed anionic species ($\text{A}^- = \text{PO}_2\text{F}_2^-$ and PO_3F_2^-) can act as complexing agents,¹⁸⁶⁻¹⁹⁰ resulting in the negatively shifted redox wave (b) (Figure 3.5). The positively shifted wave (c) corresponds to the lithium salt adduct of $[\text{Fe}(\text{dapsox})(\text{CH}_3\text{CN})(\text{A})]$. This two wave behavior can be interpreted in terms of the high stability constant of the lithium salt adduct.¹⁹¹ The coordination of negatively charged A^- , affecting the overall charge of the complex, facilitates stronger Li^+ binding.

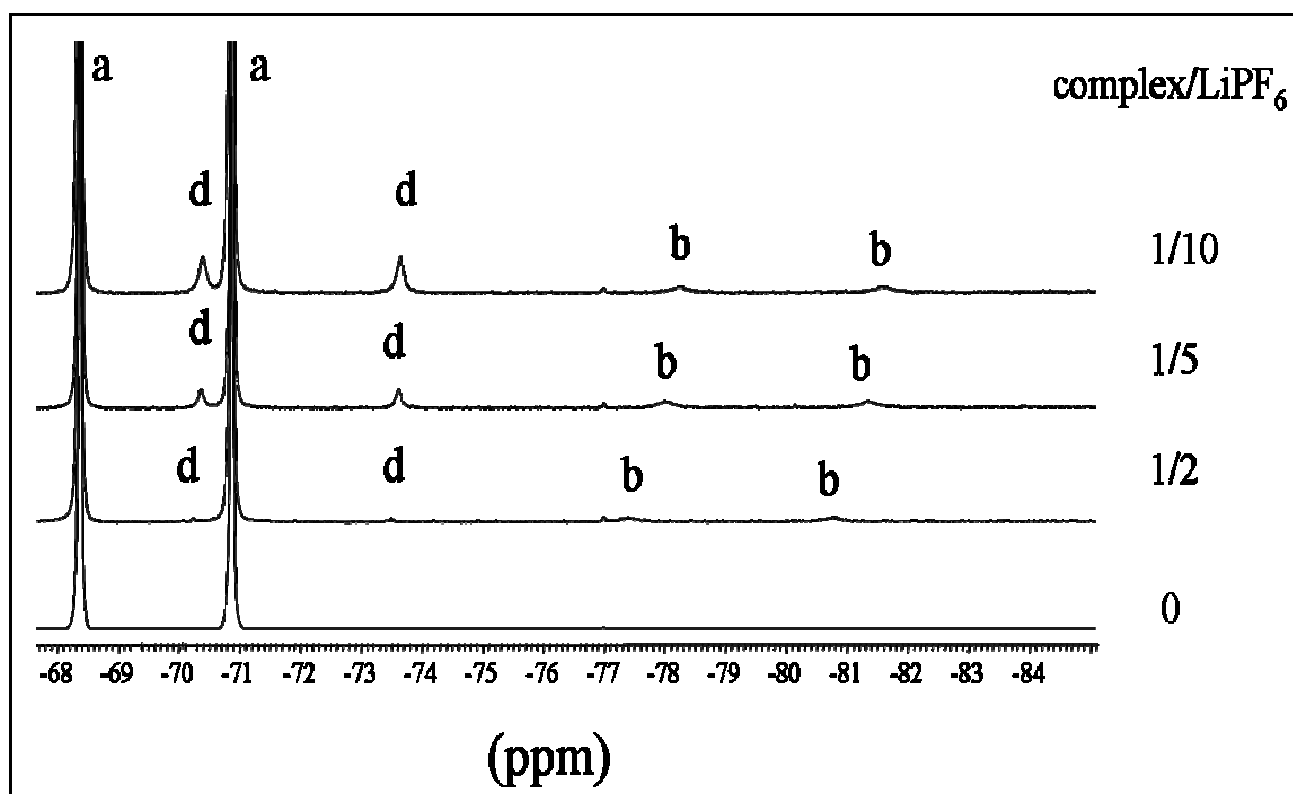


Figure 3.7. ^{19}F NMR spectra of CH_3CN solutions at 25 °C, containing constant iron complex concentration (0.5 mM) and increasing concentrations of LiPF_6 . Signals (a) and (b) are assigned to PF_6^- and $[\text{Fe}(\text{dapsox})(\text{CH}_3\text{CN})(\text{PO}_2\text{F}_2)]^-$, respectively.

Analogous to Scheme 3.2 and according to eq 3.2,^{153, 179} the $K^{\text{II}}/K^{\text{III}}$ quotient (the binding enhancement factor or the reaction coupling efficiency¹⁵³) is 52600, suggesting strong coupling between lithium binding and iron reduction. It also shows that in the Fe^{II} form the negatively charged $[\text{Fe}(\text{dapsox})(\text{CH}_3\text{CN})(\text{A})]^-$ adduct binds Li^+ very efficiently.

$$\Delta E = \frac{RT}{F} \ln \frac{K^{\text{II}}}{K^{\text{III}}} \quad (3.2)$$

At higher lithium concentrations, wave (b) vanishes whereas wave (c) becomes broader and starts to anodically shift further (wave (d) in Figure 3.5). These additional processes are most probably related to the further hydrolysis of PF_6^- -related anionic species and increase in the HF concentration, which might result in protonation of the complex.

3.4.3. ^7Li NMR Titrations

In order to better visualize the lithium ion binding to the seven-coordinate iron(III) complex, ^7Li NMR measurements were performed. Different from the electrochemical measurements, where the effects of host–guest interactions on the redox active iron center can be observed, ^7Li NMR titrations can demonstrate the complexation effect on the Li^+ cation itself. The NMR chemical shift titration has been widely used as a method for the determination of binding constants.^{151, 152, 192-194} The easily observed and sensitive ^7Li isotope has nuclear spin $I = 3/2$ and high abundance (95%), making it an attractive nucleus for NMR titrations.¹⁹⁵⁻¹⁹⁷ In the case of host–guest complexation reactions, either the concentration of guest (^7Li nucleus) or of the host is varied and the resulting change in the chemical shift is followed. If the reaction is fast on the NMR timescale, only one shift will be observed, representing a concentration-weighted average of the shifts of free and bound species.

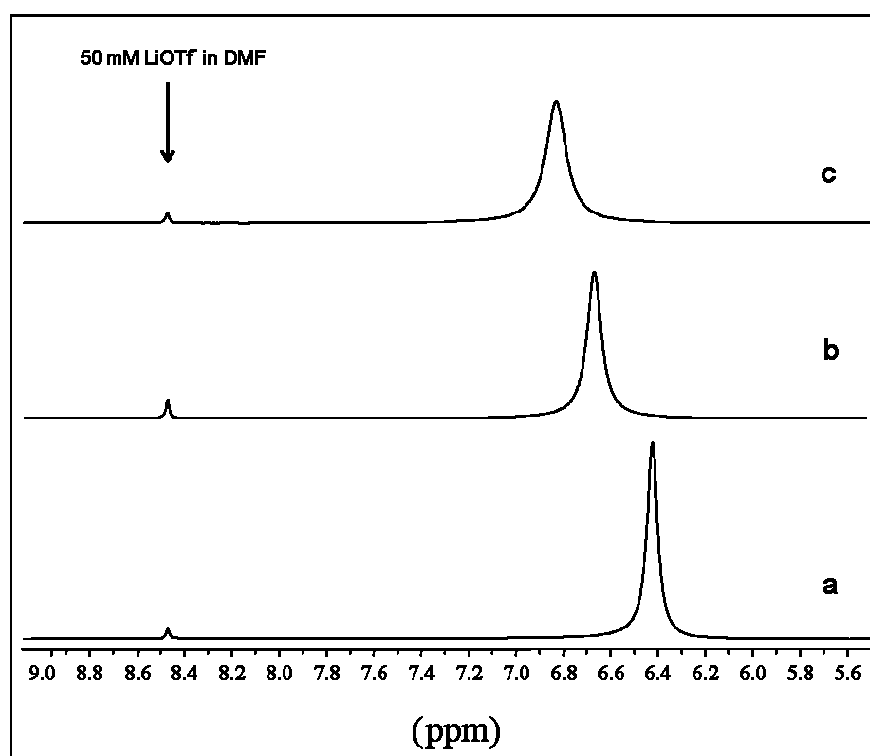


Figure 3.8. ^7Li NMR Spectra of LiOTf (0.2 M) solution in CH_3CN at 25 °C in the presence of (a) 0.5 mM, (b) 1 mM and (c) 1.5 mM $[\text{Fe}(\text{dapsox})(\text{CH}_3\text{CN})_2]^+$.

In the first set of measurements, the concentration of Li^+ (200 mM LiOTf) was kept constant. Three different probes with the iron complex concentration of 0.5, 1.0, and 1.5 mM were measured. It can be seen in Figure 3.8, that the lithium resonance peak broadens and shifts downfield (relative to the chemical shift of free Li^+ in CH_3CN with $\delta = 5.7$ ppm, see Figure 3.9), with an increase in $[\text{Fe}(\text{dapsox})\text{-(CH}_3\text{CN)}_2]^+$ concentration. The downfield resonance shift is indicative of the complexation, implying that the solvation environment around the lithium cation is perturbed upon addition of the paramagnetic ($\mu_{\text{eff}} = 5.26 \mu_{\text{B}}$)⁵³ receptor complex.

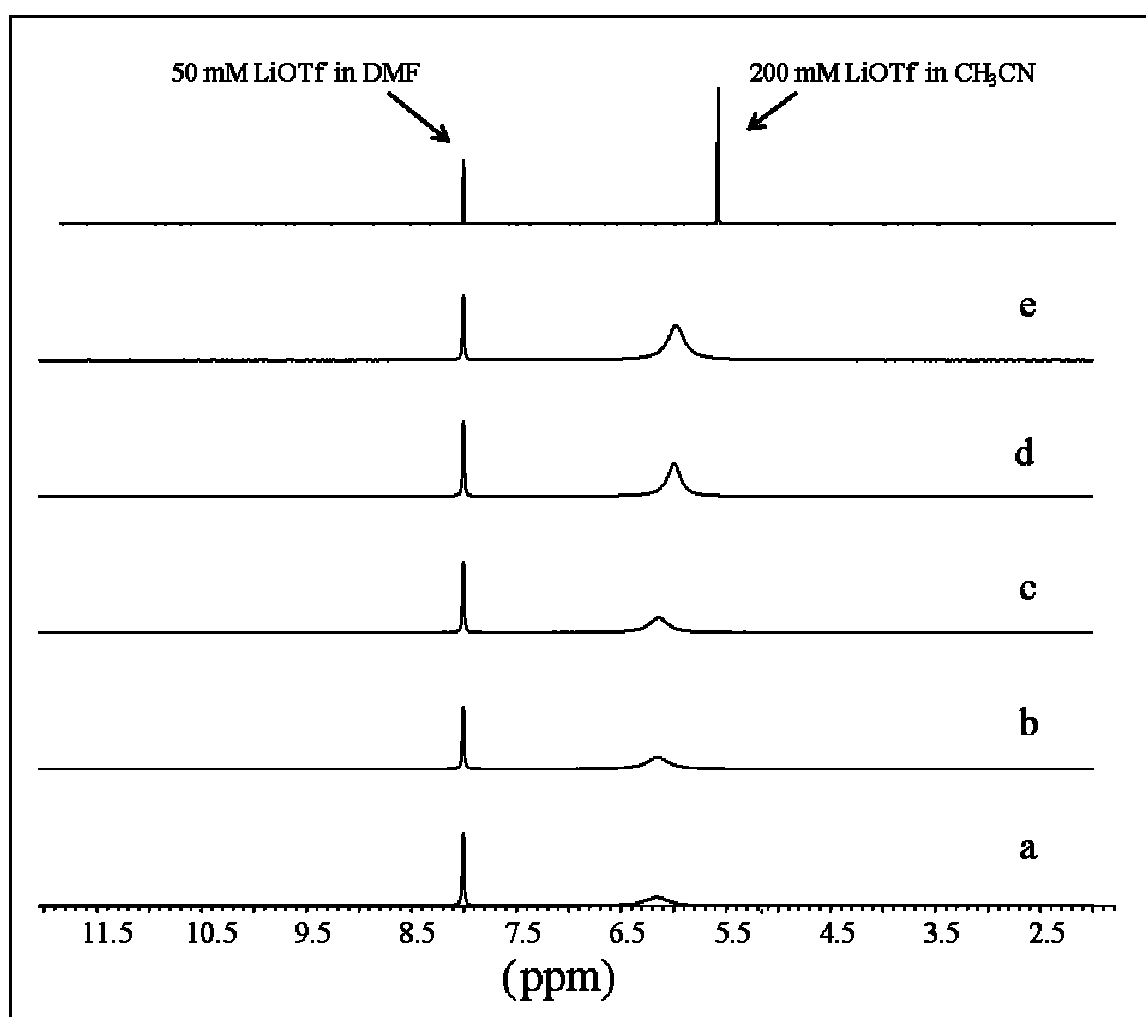


Figure 3.9. ^7Li NMR Spectra of a) 5 mM, (b) 15 mM, (c) 25mM, (d) 35 mM, and (e) 50 mM LiOTf in the presence of constant iron complex concentration (0.5 mM) in CH_3CN . Measurements were run at room temperature.

Another set of data was obtained by keeping the concentration of the iron complex constant (0.5 mM) and varying the concentration of Li^+ between 5 and 50 mM (Figure 3.9). Increase in lithium salt concentration causes an upfield shift of the ^7Li resonance towards the position of free Li^+ . This also provides qualitative evidence for the host–guest interaction.

In an attempt to quantitatively determine the apparent lithium binding constant, ^7Li NMR T_1 relaxation measurements were performed. The concentration of the seven-coordinate iron complex was held constant (0.5 mM), whereas the concentration of the lithium salts (LiOTf , LiClO_4 and LiBF_4) was varied between 5 and 50 mM (10–100-fold excess). The concentration ($[\text{Li}^+] = 500 \text{ mM}$) was used in all cases to observe relaxation time at saturation ($T_{1(\text{free})}$). Only one type of Li^+ binding site was assumed to be present, as well as monoexponential relaxation of the Li^+ nucleus (Figure 3.10) and fast exchange of Li^+ between free and bound states.¹⁹⁸

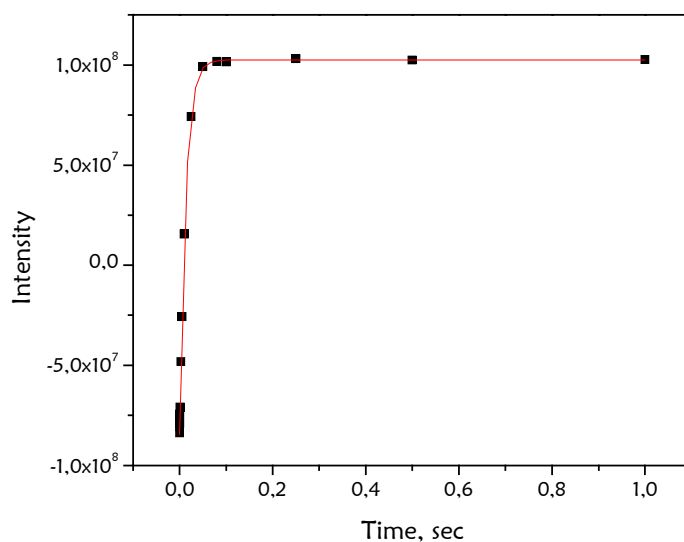


Figure 3.10. Mono-exponential relaxation of the Li^+ nucleus, obtained by using the inversion recovery pulse sequence method for the determination of T_1 relaxation time (see [Section 3.3.5.](#)). Experimental conditions: $[\text{complex}] = 0.5 \text{ mM}$, $[\text{LiOTf}] = 15 \text{ mM}$, $25 \text{ }^\circ\text{C}$.

According to these assumptions, the apparent binding constants K^{III} were calculated from James–Noggle plots of ΔR^{-1} against $[\text{Li}^+]$ according to eq 3.3, using at least five ${}^7\text{Li}$ T_1 values,^{168, 198, 199} under the experimental conditions where $[\text{Li}^+] \gg [\text{Fe}]$

$$\Delta R^{-1} = (R_{\text{obs}} - R_{\text{free}})^{-1} = (K^{\text{III}})^{-1} \{[\text{Fe}](R_{\text{bound}} - R_{\text{free}})\}^{-1} + [\text{Li}^+] \{[\text{Fe}](R_{\text{bound}} - R_{\text{free}})\}^{-1} \quad (3.3)$$

$[\text{Li}^+]$ and $[\text{Fe}]$ are the concentrations of Li^+ and iron complex, respectively. $R_{\text{obs}} = 1/T_{1(\text{obs})}$, $R_{\text{free}} = 1/T_{1(\text{free})}$, and $R_{\text{bound}} = 1/T_{1(\text{bound})}$ are the relaxation rates (or the reciprocals of the relaxation times) for the Li^+ nuclei of the observed sample (R_{obs}), with saturating Li^+ concentrations ($R_{\text{free}}(\text{LiOTf}) = 7.6 \text{ s}^{-1}$, $R_{\text{free}}(\text{LiClO}_4) = 5.6 \text{ s}^{-1}$, $R_{\text{free}}(\text{LiBF}_4) = 7.4 \text{ s}^{-1}$), or with Li^+ bound (R_{bound}), respectively (Table 3.3). This approach has the inherent approximation of using a binding model with a single type of Li^+ binding site, with a single K^{III} and R_{bound} value.

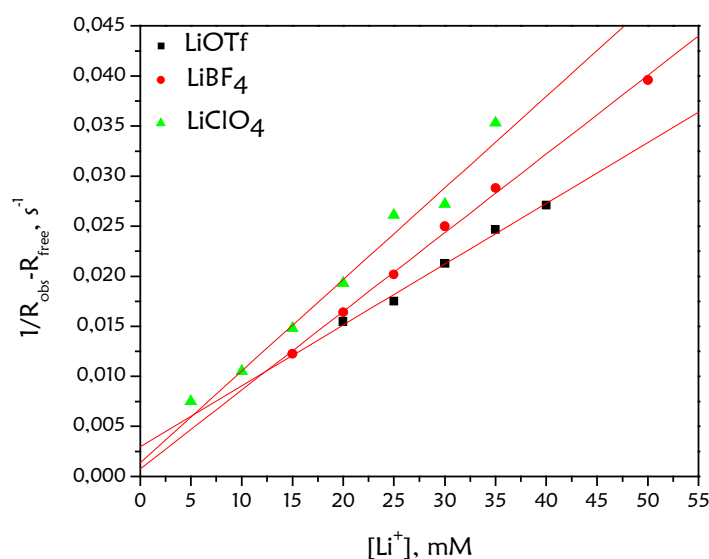


Figure 3.11. Representative James–Noggle plots for $[\text{Fe}(\text{dapsox})(\text{CH}_3\text{CN})_2]^+$ complex in the presence of (■) LiOTf, (●) LiBF₄ and (▲) LiClO₄. The x axis corresponds to the lithium salt concentrations used in the titrations of seven-coordinate iron complex, and the y axis represents $1/(R_{\text{obs}} - R_{\text{free}})$, where R_{obs} and R_{free} are the relaxation rates (or the reciprocal of the relaxation times) for the Li^+ nuclei of the observed sample ($T_{1(\text{obs})}$) and with saturating Li^+ concentrations ($T_{1(\text{free})}$), respectively (eq 3.3).

Table 3.3. The measured ${}^7\text{Li}$ NMR T_{obs} , T_{free} , R_{obs} , R_{free} and $(R_{\text{obs}}-R_{\text{free}})^{-1}$ relaxation values for LiOTf, LiClO_4 and LiBF_4 in the presence of 0.5 mM of $[\text{Fe}(\text{dapsox})(\text{CH}_3\text{CN})_2]^+$. $T = 25\text{ }^\circ\text{C}$.

A ⁻	[Li ⁺ A ⁻], mM	T_{obs} , s	T_{free} , s	R_{obs} , s ⁻¹	R_{free} , s ⁻¹	$(R_{\text{obs}}-R_{\text{free}})^{-1}$
OTf	20	0.0139 ± 0.0005		72.2 ± 2.6		0.0155 ± 0.0006
	25	0.0155 ± 0.0007		64.7 ± 2.9		0.0175 ± 0.0009
	30	0.0183 ± 0.0007		54.6 ± 2.1		0.0213 ± 0.0010
	35	0.0208 ± 0.0011		48.1 ± 2.5		0.0247 ± 0.0015
	40	0.0225 ± 0.0004		44.5 ± 0.8		0.0271 ± 0.0006
	500		0.131 ± 0.01		7.6 ± 0.6	
ClO_4^-	5	0.0072 ± 0.0001		138.9 ± 1.9		0.0075 ± 0.0001
	10	0.0099 ± 0.0001		101.0 ± 1.0		0.0105 ± 0.0001
	15	0.0137 ± 0.0001		73.0 ± 0.5		0.0148 ± 0.0001
	20	0.0175 ± 0.0003		57.1 ± 1.0		0.0194 ± 0.0004
	25	0.0228 ± 0.0014		43.9 ± 2.7		0.0261 ± 0.0020
	30	0.0236 ± 0.0021		42.4 ± 3.8		0.0272 ± 0.0028
	35	0.0296 ± 0.0024		33.8 ± 2.7		0.0355 ± 0.0034
	500		0.180 ± 0.02		5.6 ± 0.6	
BF_4^-	15	0.0112 ± 0.0003		89.1 ± 2.4		0.0122 ± 0.0004
	20	0.0146 ± 0.0008		68.4 ± 3.8		0.0164 ± 0.0010
	25	0.0175 ± 0.0008		57.0 ± 2.6		0.0202 ± 0.0011
	30	0.0211 ± 0.0023		47.4 ± 5.2		0.0250 ± 0.0033
	35	0.0238 ± 0.0012		42.1 ± 2.1		0.0288 ± 0.0017
	50	0.0306 ± 0.0017		32.7 ± 1.8		0.0396 ± 0.0028
	500		0.136 ± 0.01		7.4 ± 0.5	

In all three cases, good linear plots of ΔR^{-1} vs. $[\text{Li}^+]$ were obtained (Figure 3.11). By dividing the slopes of the linear fits (solid lines) in Figure 8 by the corresponding intercepts and multiplying the quotients by 1000, the values of the apparent binding constant K^{III} in M^{-1} could be derived (Table 3.2). However, the values obtained for

the intercepts in the case of LiClO_4 and LiBF_4 are rather small with high uncertainties, and consequently, could not be used for the quantification of K^{III} . In the case of LiOTf the K^{III} binding constant was found to be $203 \pm 68 \text{ M}^{-1}$ (Table 3.2), which is somewhat higher than the corresponding value obtained from electrochemical titration, generally in agreement with the higher ionic strength of the solutions used in electrochemical experiments.

3.4.4. Spectrophotometric Determination of K^{III}

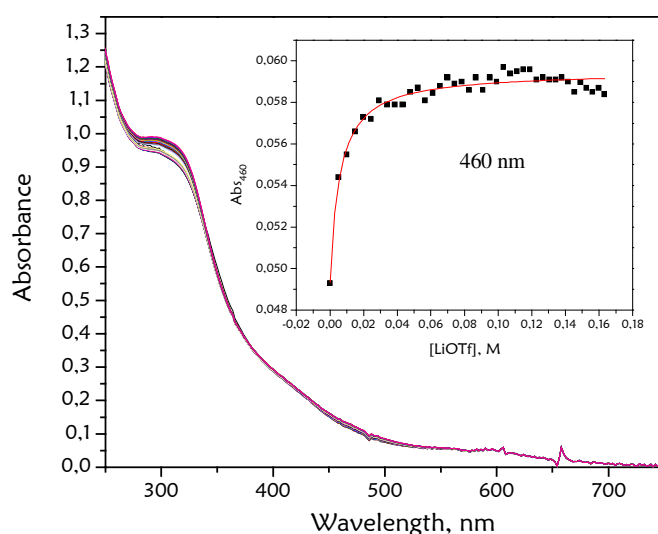


Figure 3.12. Spectral changes upon addition of LiOTf to the $5 \times 10^{-5} \text{ M}$ solution of $[\text{Fe}(\text{dapsox})(\text{CH}_3\text{CN})_2]^+$. Inset: the change in absorbance at 460 nm plotted vs. $[\text{LiOTf}]$; solid line represents nonlinear fitting curve (according to eq 3.4).

In an attempt to spectrophotometrically determine the K^{III} value, the $[\text{Fe}(\text{dapsox})(\text{CH}_3\text{CN})_2]^+$ complex was titrated with LiOTf at $25 \text{ }^\circ\text{C}$. The absorbances at 460 nm vs $[\text{LiOTf}]$ (inset in Figure 3.12) were fitted by applying eq 3.4

$$A_x = A_0 + \frac{(A_\infty - A_0)K^{\text{III}}[\text{LiOTf}]}{1 + K^{\text{III}}[\text{LiOTf}]} \quad (3.4)$$

The values of A_0 and A_∞ represent absorbance at 0 and 100% formation of complex, respectively, and A_x represents the absorbance at any given lithium triflate

concentration. The observed spectral changes upon addition of LiOTf are not so prominent (Figure 3.12), however, the resulting apparent binding constant $K^{\text{III}} = 175 \pm 19 \text{ M}^{-1}$ is in excellent agreement with the corresponding K^{III} value obtained by ^7Li NMR measurements (Table 3.2), where in both experiments no additional supporting electrolyte was present in solution (experiments under the same ionic strength).

3.4.5. Reaction with SCN^- in CH_3CN

Kinetics of the reaction between $[\text{Fe}(\text{dapsox})(\text{CH}_3\text{CN})_2]^+$ complex and thiocyanate (SCN^-) in acetonitrile was studied under pseudo-first-order conditions (a large excess of SCN^-) at $-15 \text{ }^\circ\text{C}$ and at constant ionic strength ($I = 0.2 \text{ M}$), adjusted with Bu_4NOTf and LiOTf (see below), respectively.

Spectral changes and corresponding kinetic traces (Figure 3.13) clearly showed two subsequent reaction steps over the whole SCN^- concentration range. Similar to what was found in aqueous, methanol, and ethanol solutions, the two reaction steps represent the substitution of two axially coordinated solvent molecules by SCN^- .^{55, 148} Kinetic traces were fitted to a double-exponential function that resulted in k_{obs} values for the first and second reaction steps. Plots of k_{obs} versus $[\text{SCN}^-]$ (Figure 3.14) for both reaction steps at $-15 \text{ }^\circ\text{C}$ in the presence of Bu_4NOTf , as well as LiOTf , show a linear increase in k_{obs} with increasing $[\text{SCN}^-]$ over the whole concentration range with more prominent intercepts in the case of the first reaction step. The dependence of k_{obs} on $[\text{SCN}^-]$ for both reactions can be expressed by eq 3.5, where k_1 and k_2 represent the rate constants for the forward reactions (from the slopes of the solid lines) and k_{-1} and k_{-2} represent the rate constants for the backward (from the intercepts) reactions in the presence of NBu_4OTf . For the reaction performed in the presence of LiOTf , an expression analogous to eq 3.5 can be applied for the first and second substitution with the corresponding $k_{1\text{Li}}$, $k_{2\text{Li}}$, $k_{-1\text{Li}}$, and $k_{-2\text{Li}}$ rate constants.

$$k_{\text{obs}(1,2)} = k_{1,2}[\text{SCN}^-] + k_{-1,-2} \quad (3.5)$$

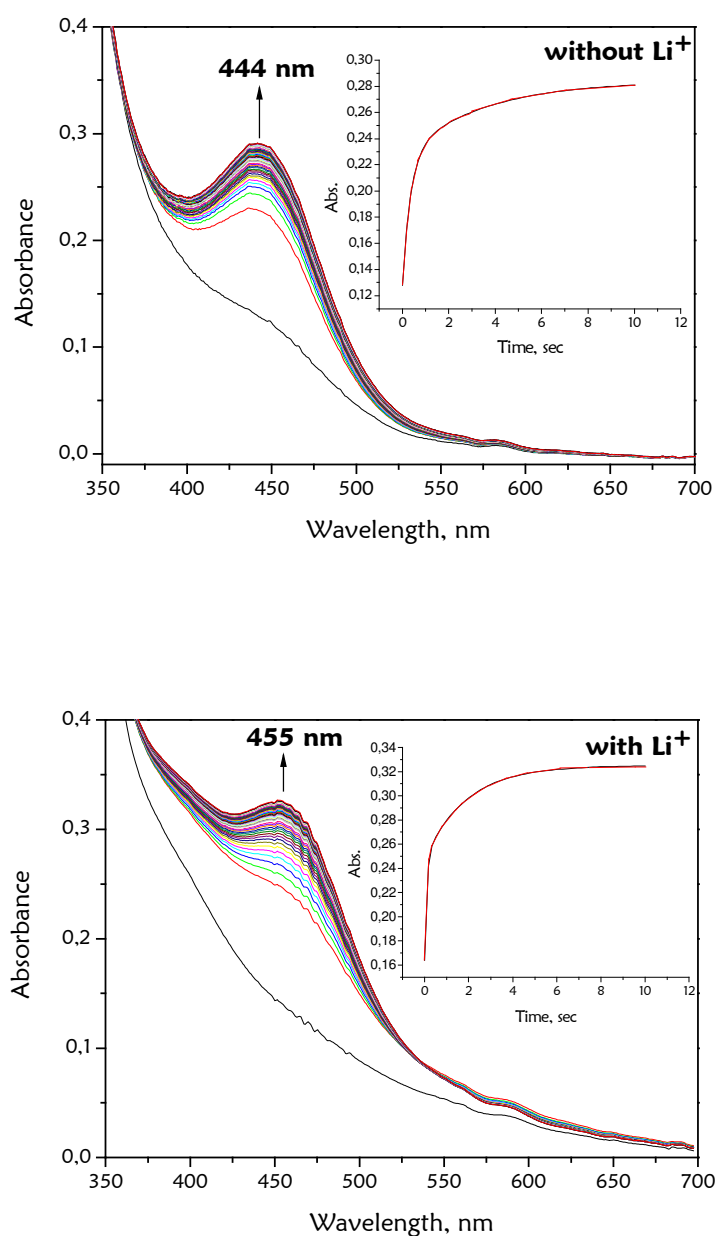


Figure 3.13. Spectral changes during the reaction of $[\text{Fe}(\text{dapsox})(\text{CH}_3\text{CN})_2]^+$ with NaSCN in the presence of (above) Bu_4NOTf and (below) LiOTf ($[\text{Fe}^{\text{III}}\text{dapsox}] = 5 \times 10^{-5} \text{ M}$, $[\text{SCN}^-] = 0.005 \text{ M}$, $I = 0.2 \text{ M}$, $-15.0 \text{ }^\circ\text{C}$). Inset: corresponding kinetic traces at 448 nm and double-exponential fits (solid lines).

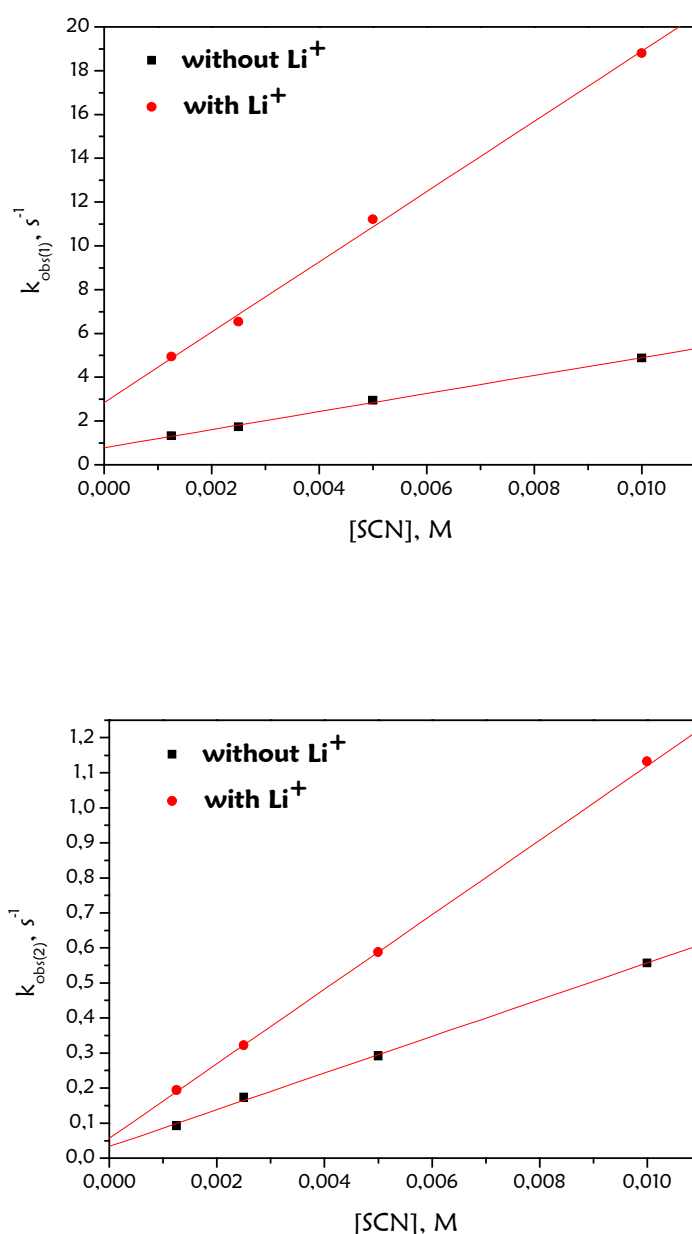
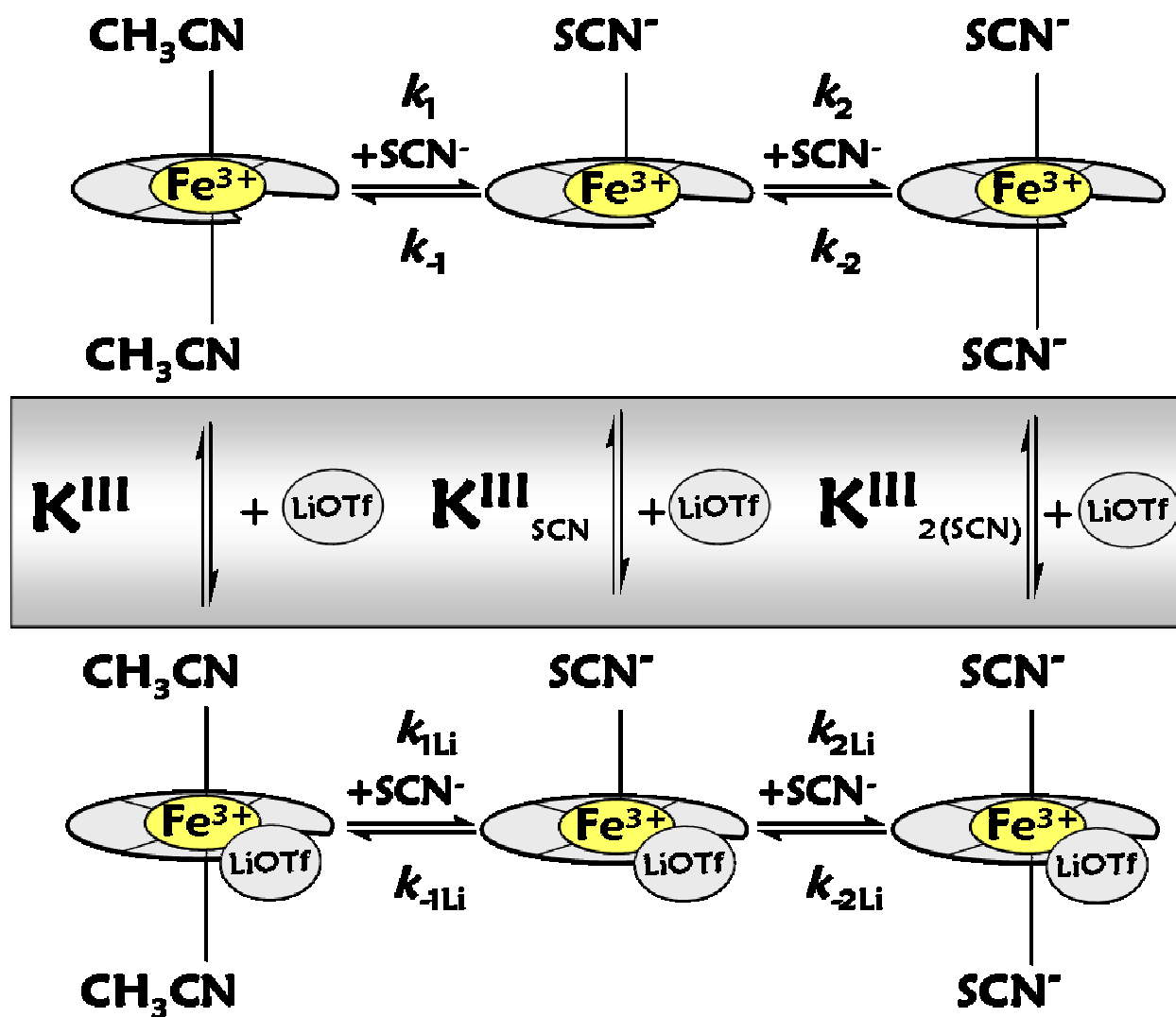


Figure 3.14. Plots of k_{obs} vs. $[\text{SCN}^-]$ for the first (above) and second (below) reaction steps in the absence (■) and in the presence (●) of LiOTf. Experimental conditions: ($[\text{Fe}^{\text{III}}\text{dapsox}] = 5 \times 10^{-5} \text{ M}$, $I = 0.2 \text{ M}$, $-15.0 \text{ }^\circ\text{C}$).

From these values, the equilibrium constants $K_1^{\text{SCN}} = k_1/k_{-1}$ and $K_2^{\text{SCN}} = k_2/k_{-2}$ for the binding of the first and second SCN^- in the presence of NBu_4OTf and LiOTf can be calculated. The reaction scheme as well as corresponding rates and equilibrium constants are summarized in Scheme 3.3 and Table 3.4, respectively.



Scheme 3.3.

Table 3.4. Kinetic Results for the Reactions of NaSCN with $[\text{Fe}(\text{dapsox})(\text{CH}_3\text{CN})_2]^+$ at -15°C and 0.2 M Ionic Strength in CH_3CN .

	0.2 M (Bu_4NOTf)		0.2 M ($\text{Bu}_4\text{NOTf}/\text{LiOTf}$)
$k_1, \text{M}^{-1} \text{s}^{-1}$	411 ± 14	$k_{1\text{Li}}, \text{M}^{-1} \text{s}^{-1}$	1605 ± 51
k_{-1}, s^{-1}	0.79 ± 0.08	$k_{-1\text{Li}}, \text{s}^{-1}$	2.8 ± 0.3
$K_1^{\text{SCN}}, \text{M}^{-1}$	$520 \pm 56^{\text{a}}$		$574 \pm 64^{\text{a}}$
	$237 \pm 53^{\text{b}}$		$727 \pm 17^{\text{b}}$
$\Delta H_1^\ddagger, \text{kJ mol}^{-1}$	9 ± 2		
$\Delta S_1^\ddagger, \text{J mol}^{-1} \text{K}^{-1}$	-159 ± 6		
$k_2, \text{M}^{-1} \text{s}^{-1}$	52 ± 1	$k_{2\text{Li}}, \text{M}^{-1} \text{s}^{-1}$	106 ± 2
k_{-2}, s^{-1}	0.033 ± 0.007	$k_{-2\text{Li}}, \text{s}^{-1}$	0.056 ± 0.004
$K_2^{\text{SCN}}, \text{M}^{-1}$	$1575 \pm 336^{\text{a}}$		$1893 \pm 140^{\text{a}}$
	$1326 \pm 468^{\text{b}}$		$1900 \pm 210^{\text{b}}$
$\Delta H_2^\ddagger, \text{kJ mol}^{-1}$	4 ± 1		
$\Delta S_2^\ddagger, \text{J mol}^{-1} \text{K}^{-1}$	-195 ± 3		
$K^{\text{III}}, \text{M}^{-1}$			$49 \pm 10^{\text{c}}$
$K^{\text{III}}_{\text{SCN}}, \text{M}^{-1}$			$152 \pm 24^{\text{c}}$
$K^{\text{III}}_{2(\text{SCN})}, \text{M}^{-1}$			$775 \pm 54^{\text{d}}$

^a calculated as $K_1^{\text{SCN}} = k_1/k_{-1}$, $K_2^{\text{SCN}} = k_2/k_{-2}$. ^b results from nonlinear fitting of the spectrophotometric titration curves of $[\text{Fe}(\text{dapsox})(\text{CH}_3\text{CN})_2]$ and $\{[\text{Fe}(\text{dapsox})(\text{CH}_3\text{CN})_2] \bullet \text{LiOTf}\}$ with NaSCN at 25°C (eq 3.6, Figure 3.15). ^c determined by

nonlinear fitting of saturation kinetic curves (eq 3.7 and 3.8, Figure 3.18). ^d results from nonlinear fitting of the spectrophotometric titration curves of $[\text{Fe}(\text{dapsox})(\text{NCS})_2]^-$ with LiOTf at 25 °C (eq 3.4, Figure 3.19)

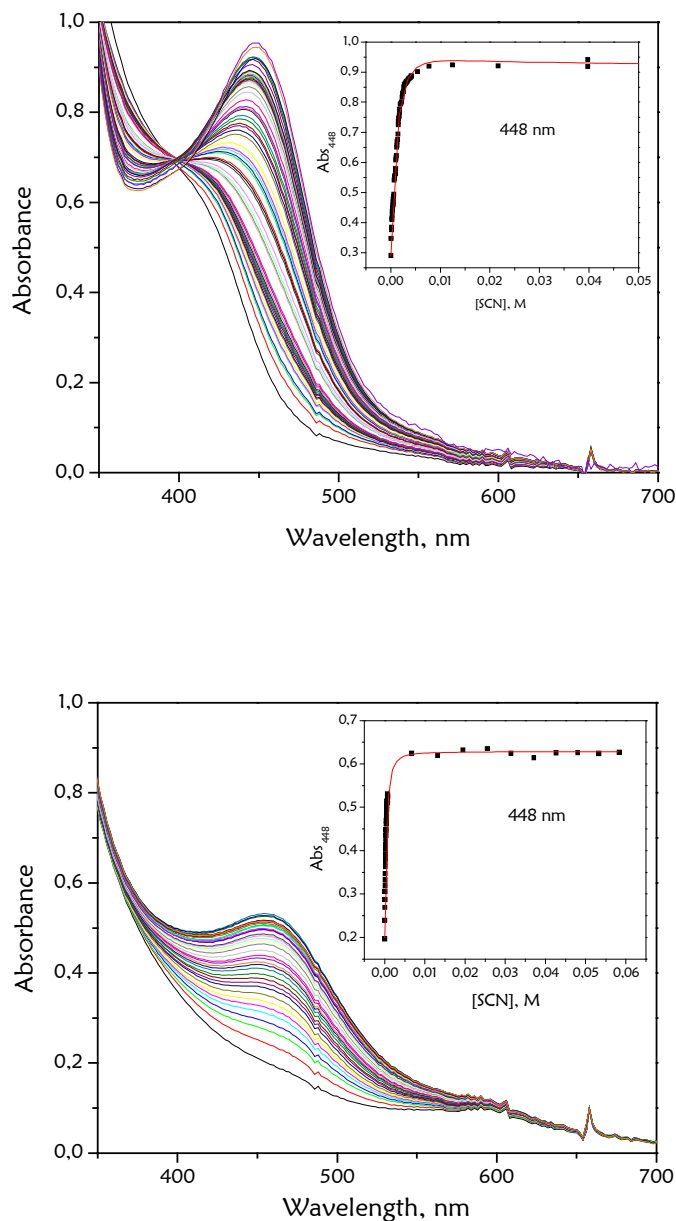


Figure 3.15. Spectral changes observed during the titration of $[\text{Fe}(\text{dapsox})(\text{CH}_3\text{CN})_2]^+$ (1×10^{-4} M) with NaSCN in the absence (above) and in the presence (below) of 0.2M LiOTf . Inset: The corresponding absorbances at 448 nm plotted vs $[\text{NaSCN}]$. Solid lines represent results of nonlinear fitting (eq 3.6).

3.4.6. Equilibrium Studies for Binding of SCN⁻

The equilibrium constants K_1^{SCN} and K_2^{SCN} were determined by spectrophotometric titrations of $[\text{Fe}(\text{dapsox})(\text{CH}_3\text{CN})_2]^+$ with NaSCN in CH_3CN solution at 25 °C. The spectral changes for the reactions with and without LiOTf ($I = 0.2 \text{ M}$) are presented in Figure 3.15. For determination of equilibrium constants, the absorbances at 448 nm vs $[\text{SCN}^-]$ (insets in Figure 3.15) were fitted, in both cases, for the first and the second equilibrium together to eq 3.6.

$$A_x = \frac{A_0 + A_1 K_1^{\text{SCN}} [\text{SCN}^-] + A_2 K_1^{\text{SCN}} K_2^{\text{SCN}} [\text{SCN}^-]^2}{1 + K_1^{\text{SCN}} [\text{SCN}^-] + K_1^{\text{SCN}} K_2^{\text{SCN}} [\text{SCN}^-]^2} \quad (3.6)$$

The values of A_0 represent the absorbance at 0 % formation of complex, A_1 and A_2 ascribe absorbances of $[\text{Fe}(\text{dapsox})(\text{CH}_3\text{CN})(\text{NCS})]$ and $[\text{Fe}(\text{dapsox})(\text{NCS})_2]^-$ species, respectively, and A_x represents the absorbance at any given thiocyanate concentration $[\text{SCN}^-]$. The average values of K_1^{SCN} and K_2^{SCN} obtained by fitting titration curves at 448 nm according to eq 3.6, as well as independently over the 200–700 nm wavelength range with Specfit/32 global analysis are summarized in Table 3.4.

3.4.7. Temperature-Dependent Kinetic Measurements

The electrochemical and NMR titrations of $[\text{Fe}(\text{dapsox})(\text{CH}_3\text{CN})_2]^+$ with LiOTf (see Sections 3.4.1 and 3.4.3) have shown that there is a host–guest interaction between the complex and lithium salt, and that in the presence of 0.2 M LiOTf the predominant species in solution is the $\{[\text{Fe}(\text{dapsox})(\text{CH}_3\text{CN})_2] \bullet \text{LiOTf}\}^+$ adduct. At the same time, our kinetic and thermodynamic data for the reactions with SCN^- show (Figure 3.14 and Table 3.4) that in the presence of 0.2 M LiOTf both reaction steps proceed with higher rate constants ($k_{1\text{Li}}$ and $k_{2\text{Li}}$) and the corresponding apparent binding constants (K_1^{SCN} and K_2^{SCN}) are also somewhat higher than in the case when instead of LiOTf, 0.2 M Bu_4NOTf was present in solution. This clearly suggests that the $\{[\text{Fe}(\text{dapsox})(\text{CH}_3\text{CN})_2] \bullet \text{LiOTf}\}^+$ adduct has a higher reactivity towards the SCN^- anion and that its mono- and bis(thiocyanato) species have higher thermodynamic

stability. To clarify mechanistically this phenomenon, temperature-dependent kinetic measurements of the reaction of $[\text{Fe}(\text{dapsox})(\text{CH}_3\text{CN})_2]^+$ with SCN^- and 0.2 M Bu_4NOTf as supporting electrolyte were performed. Plots of k_{obs} versus $[\text{SCN}^-]$ for the first and second reaction steps as a function of temperature, and the corresponding Eyring plots are presented in Figures 3.16 and 3.17. The obtained activation parameters ΔH^\ddagger and ΔS^\ddagger are also included in Table 3.4.

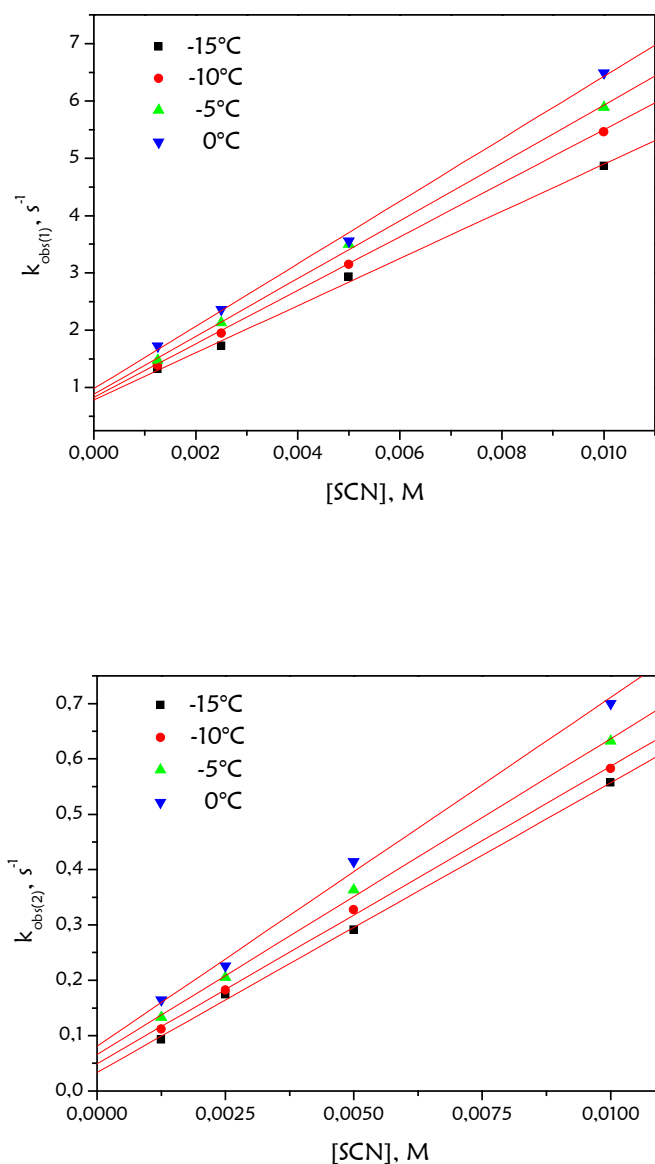


Figure 3.16. Plots of k_{obs} versus $[\text{SCN}^-]$ for the first (above) and second (below) reaction steps as a function of temperature ($[\text{complex}] = 5 \times 10^{-5}$ M, $I = 0.2$ M Bu_4NOTf).

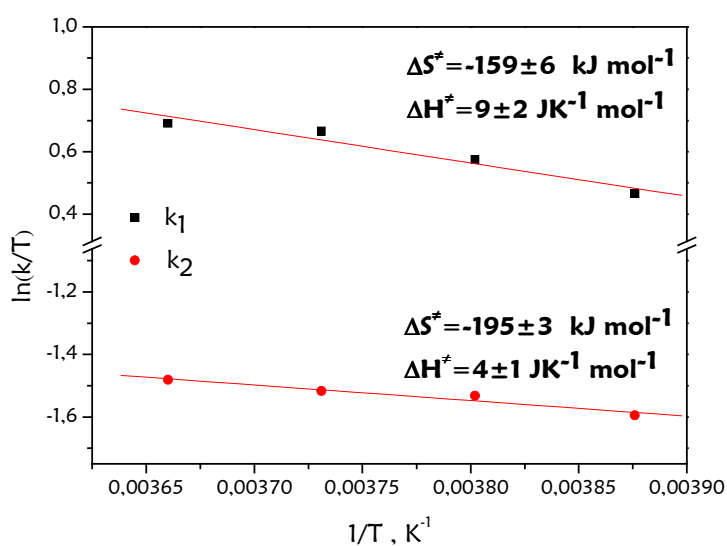


Figure 3.17. The corresponding Eyring plots (see Figure 3.16). ($[\text{complex}] = 5 \times 10^{-5} \text{ M}$, $I = 0.2 \text{ M Bu}_4\text{NOTf}$).

The very negative ΔS^\ddagger values suggest the associative nature of the rate-determining process for both substitution steps. In the case of previously studied reactions of $[\text{Fe}(\text{dapsox})(S)_2]^+$ ($S = \text{H}_2\text{O}$, MeOH , EtOH , DMSO)^{55, 148} with SCN^- in aqueous, alcoholic, and DMSO solutions, respectively, an associative interchange (I_a) mechanism (negative ΔS^\ddagger values) has been observed for the first substitution step. The second substitution step had general dissociative character (D or I_d).^{4b,c} However, $[\text{Fe}(\text{dapsox})(\text{CH}_3\text{CN})_2]^+$ shows a stronger associative character for both substitution steps, as well as higher reactivity, with k_1 and k_2 (extrapolated to 25°C) 2 and 1 order of magnitude higher than the corresponding values for the other studied $[\text{Fe}(\text{dapsox})(S)_2]^+$ complexes, respectively.^{55, 148} Increased reactivity and product stability in the case of the $\{[\text{Fe}(\text{dapsox})(\text{CH}_3\text{CN})_2] \bullet \text{LiOTf}\}^+$ adduct can also be explained in terms of an associative mechanism for the binding of SCN^- . The coordinated lithium cation close to the iron center decreases the electron density around the metal center and consequently increases its electrophilicity.

3.4.8. Lithium-Dependent Kinetic Measurements

In order to better visualize the effect of the lithium cation on the kinetic behavior of our complex, another set of measurements was performed. The reaction was followed varying $[\text{Li}^+]$ and keeping $[\text{SCN}^-]$ and ionic strength constant. Dependences of $k_{\text{obs}(1)}$ and $k_{\text{obs}(2)}$ on the lithium concentration are depicted in Figure 3.18, showing an increase of the observed rate constants for both reaction steps with increasing lithium concentration.

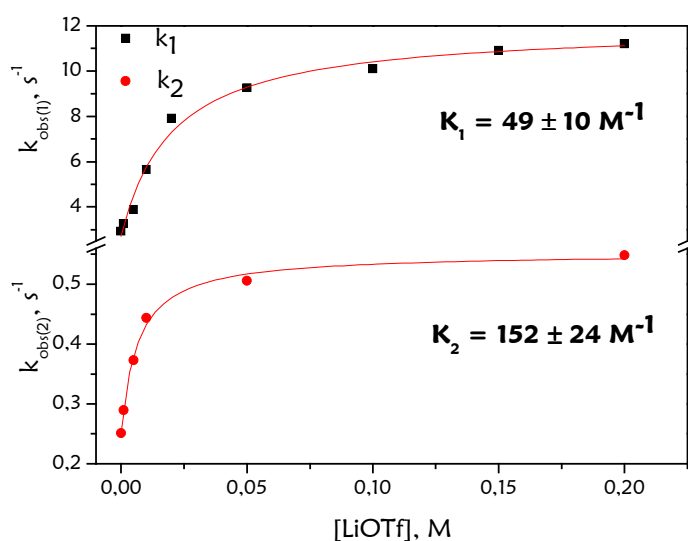


Figure 3.18. Dependences of $k_{\text{obs}(1)}$ and $k_{\text{obs}(2)}$ on the lithium concentration. Experimental conditions: ($[\text{Fe}^{\text{III}}\text{dapsox}] = 5 \times 10^{-5} \text{ M}$, $[\text{SCN}^-] = 0.005 \text{ M}$, $I = 0.2 \text{ M}$, $-15.0 \text{ }^\circ\text{C}$). Solid lines represent nonlinear fitting curves according to eq 3.7 and 3.8.

Significant curvatures are in agreement with the equilibrium between two different reactive species, $[\text{Fe}(\text{dapsox})(\text{CH}_3\text{CN})_2]^+$ (“lithium-free”) and $\{[\text{Fe}(\text{dapsox})(\text{CH}_3\text{CN})_2] \bullet \text{LiOTf}\}^+$ (“lithium-bound”) for the first, and $[\text{Fe}(\text{dapsox})(\text{NCS})]$ (“lithium-free”) and $\{[\text{Fe}(\text{dapsox})(\text{NCS})] \bullet \text{LiOTf}\}$ (“lithium-bound”) for the second reaction step. According to Scheme 3.3, the first and second reaction steps can be expressed using the somewhat simplified rate laws:

$$k_{obs(1)} = \frac{k_1 + k_{1Li} K^{III} [Li^+]}{1 + K^{III} [Li^+]} [SCN^-] + k_{-1Li} \quad (3.7)$$

$$k_{obs(2)} = \frac{k_2 + k_{2Li} K_{SCN}^{III} [Li^+]}{1 + K_{SCN}^{III} [Li^+]} [SCN^-] + k_{-2Li} \quad (3.8)$$

$k_{obs(1)}$ is the measured rate constant for the first reaction step, k_1 , k_{1Li} and k_{-1Li} are the corresponding rate constants for the “lithium-free” and “lithium-bound” forms as reactive species (Scheme 3.3), and K^{III} is the equilibrium constant for the LiOTf binding to the $[Fe(dapsox)(CH_3CN)_2]^+$ complex. Since the reverse rate constants are more prominent in the case of the “lithium-bound” forms and the corresponding K_{SCN}^{III} and $K_{2(SCN)}^{III}$ values are relatively high, the terms for the overall reverse rate constants for the first and second reaction steps in eqs 3.7 and 3.8 can be reduced to k_{-1Li} and k_{-2Li} , respectively. By analogy, $k_{obs(2)}$ is the measured rate constant for the second reaction step, k_2 , k_{2Li} and k_{-2Li} are the corresponding rate constants for the “lithium-free” and “lithium-bound” forms as reactive species (Scheme 3.3), and K_{SCN}^{III} is the equilibrium constant for the LiOTf binding to the mono(thiocyanato) $[Fe(dapsox)(NCS)]$ adduct. Although the K^{III} and K_{SCN}^{III} values are not very high, suggesting that the binding of LiOTf to the iron complex in acetonitrile is not very efficient, the interaction is strong enough to affect the kinetic behaviour. The K^{III} equilibrium constant corresponds to the constants obtained in electrochemical, and NMR experiments, respectively. The differences in the obtained values (Table 3.2) arise from the differences in experimental conditions (temperature and ionic strength).

3.4.9. Spectrophotometric Observations

Differing from the $[Fe(dapsox)(CH_3CN)_2]^+$ complex, its bis(thiocyanato) $[Fe(dapsox)(NCS)_2]^-$ adduct with a strong charge-transfer band at 440 nm shows more prominent spectral changes upon addition of LiOTf, with a shift of the absorption maximum toward longer wavelengths (~ 460 nm) as LiOTf concentration is increased (Figure 3.19). This enabled the determination of the apparent lithium

binding constant to the $[\text{Fe}(\text{dapsox})(\text{NCS})_2]^-$ species ($K_{2(\text{SCN})}^{\text{III}}$ in Table 3.4). The trend of $K^{\text{III}} < K_{\text{SCN}}^{\text{III}} < K_{2(\text{SCN})}^{\text{III}}$ (Table 3.4) is consistent with the expectation that coordinated SCN^- will increase the nucleophilicity of the complex.

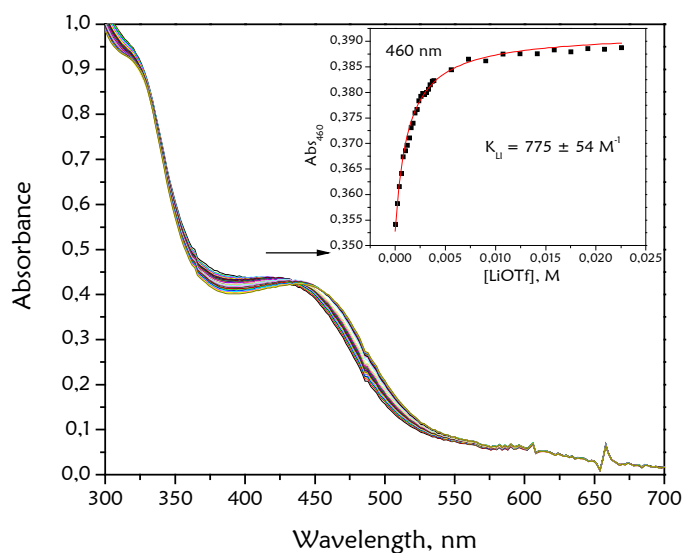


Figure 3.19. Spectral changes upon addition of LiOTf to a $5 \times 10^{-5} \text{ M}$ solution of $[\text{Fe}(\text{dapsox})(\text{NCS})_2]^-$. Inset: change in absorbance at 460 nm plotted vs $[\text{LiOTf}]$; solid line represents nonlinear fitting curve (according to eq 3.4).

Although upon addition of LiOTf to the solution of $[\text{Fe}(\text{dapsox})(\text{NCS})_2]^-$ a shift in absorption maximum is observed, it does not cause a significant color change of the solution. Similar spectral changes are observed upon addition of LiClO_4 . However, addition of LiBF_4 and LiPF_6 causes a significant change in the spectrum of $[\text{Fe}(\text{dapsox})(\text{NCS})_2]^-$, and consequently in the color of its solution. The spectral changes and the colors of the solutions, resulting from the addition of the same amount of different lithium salts (0.2 M) to $[\text{Fe}(\text{dapsox})(\text{NCS})_2]^-$ ($5 \times 10^{-5} \text{ M}$) in CH_3CN , are presented in Figure 3.20. In addition, $[\text{Fe}(\text{dapsox})(\text{NCS})_2]^-$ was titrated with LiBF_4 (Figure 3.21) and the corresponding $K_{2(\text{SCN})}^{\text{III}}$ constant was determined to be $2828 \pm 236 \text{ M}^{-1}$, showing a more prominent binding than in the case of LiOTf (Table 3.4).

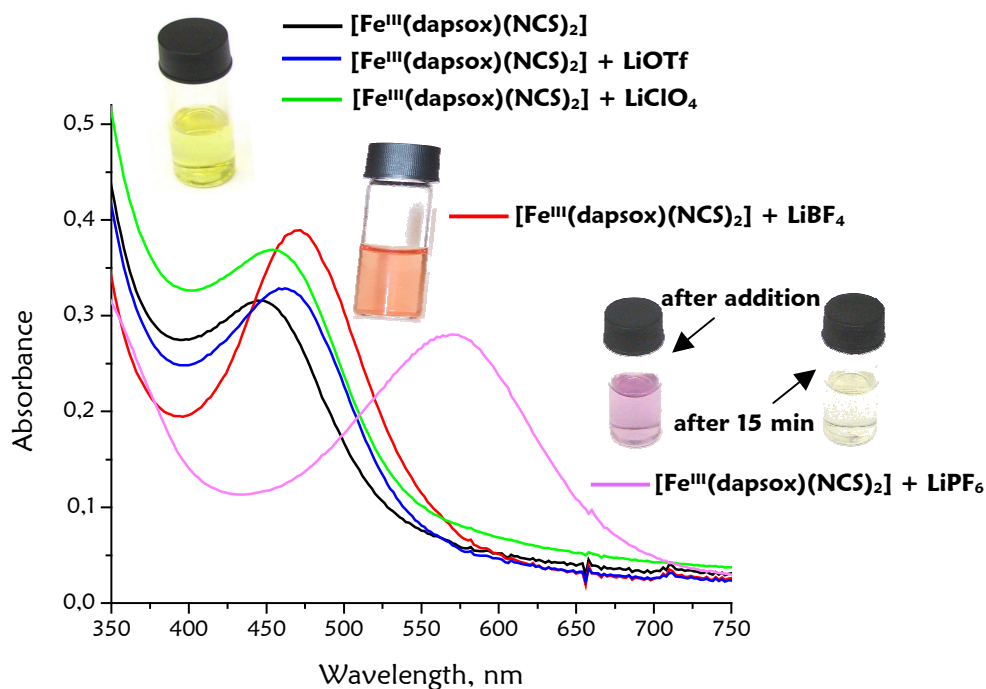


Figure 3.20. The spectra of the $[\text{Fe}(\text{dapsox})(\text{NCS})_2]^-$ solutions ($5 \times 10^{-5} \text{ M}$) measured after addition of different lithium salts (0.2 M) in CH_3CN and the change in color of corresponding product solutions.

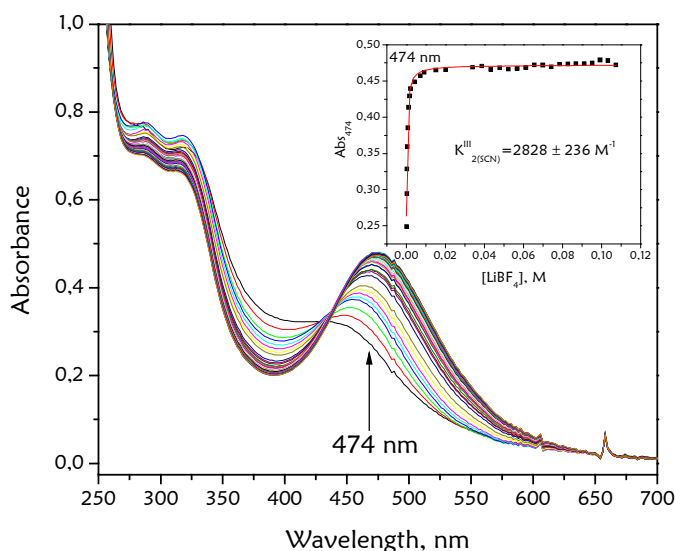


Figure 3.21. Spectral changes upon addition of LiBF_4 to the $5 \times 10^{-5} \text{ M}$ solution of $[\text{Fe}(\text{dapsox})(\text{NCS})_2]$. Inset: the change in absorbance at 474 nm plotted vs $[\text{LiBF}_4]$; solid line represents a nonlinear fitting curve (according to eq 3.4).

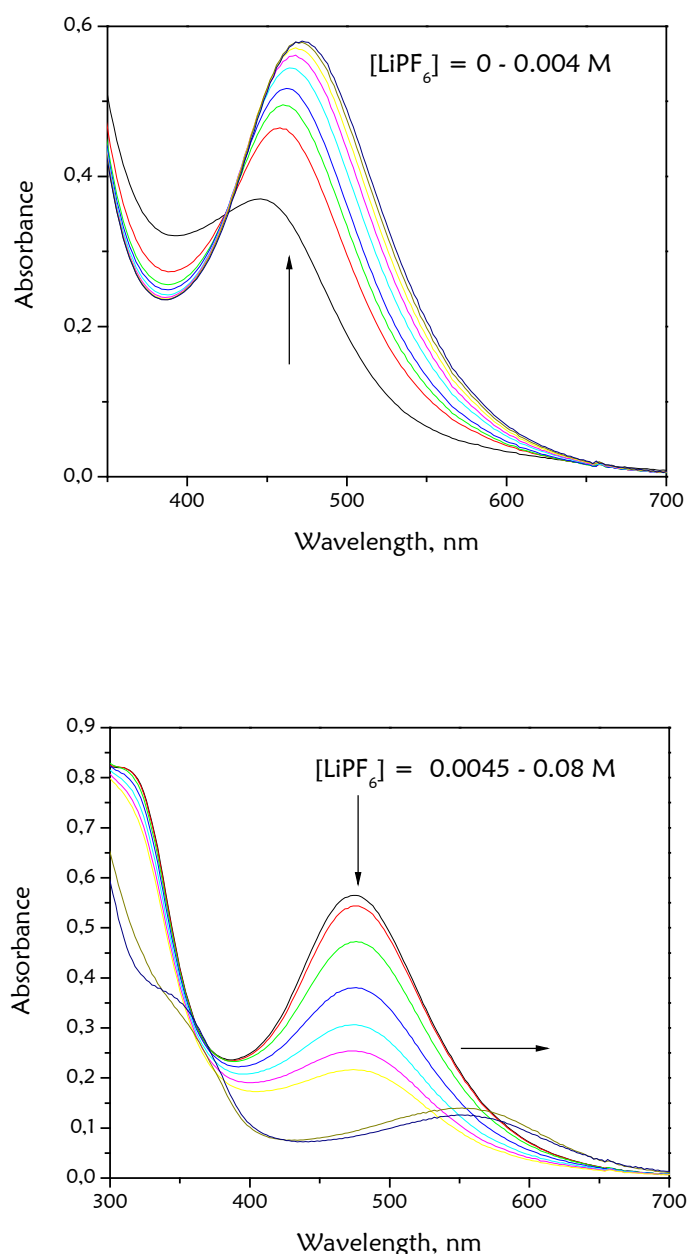


Figure 3.22. Spectral changes upon addition of LiPF_6 to the 5×10^{-5} M solution of $[\text{Fe}(\text{dapsox})(\text{NCS})_2]^-$; (above) $[\text{LiPF}_6] = 0 - 0.004 \text{ M}$, (below) $[\text{LiPF}_6] = 0.0045 - 0.08 \text{ M}$.

The product solutions in the case of LiOTf , LiClO_4 and LiBF_4 are stable, whereas the solution with LiPF_6 becomes colorless within 15 min. Interestingly, lower $[\text{LiPF}_6]$ (up to 0.004 M) cause similar spectral changes as are observed with 0.2 M LiBF_4 (Figures 3.21 and 3.22) whereas further addition of LiPF_6 leads to absorbance decrease and shift of the maximum to 570 nm (Figure 3.22). The resulting violet solution bleaches

fast. The violet color and the absorbance at 570 nm are typical for the Fe(II)–thiocyanato species, which is formed in the redox reaction between Fe^{III} and SCN⁻ in acetonitrile, and dissociates to Fe^I and thiocyanogen (SCN)₂, resulting in a colorless solution.²⁰⁰ Such complex chemistry suggests that in the presence of LiPF₆ and high [SCN⁻], dechelation of the iron(III) [Fe(dapsox)(NCS)₂]⁻ complex takes place, followed by the above-mentioned redox processes.

3.4.10. DFT Calculations

Since the attempts to crystallize the seven-coordinate Fe^{III} complex with bound lithium salt were not successful, DFT calculations were performed to provide insight into the structural characteristics of the {[Fe(dapsox)(CH₃CN)₂]•LiBF₄}⁺ adduct, with the strongest interaction between the iron complex and lithium salt (Table 3.2), and its bis(thiocyanato) {[Fe(dapsox)(NCS)₂]•LiBF₄]⁻ form (Figure 3.21). Instead of acetonitrile, hydrogen cyanide was used as a working model for the calculations. The obtained structures are shown in Figures 3.24 and 3.25.

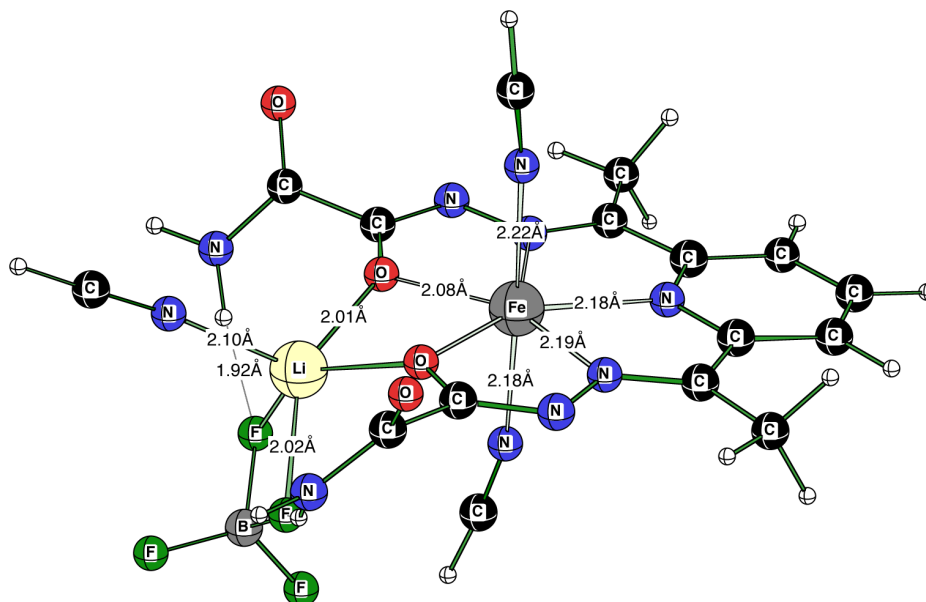


Figure 3.24. Calculated structure (B3LYP/LANL2DZp) of {[Fe(dapsox)(CH₃CN)₂]•LiBF₄}⁺.

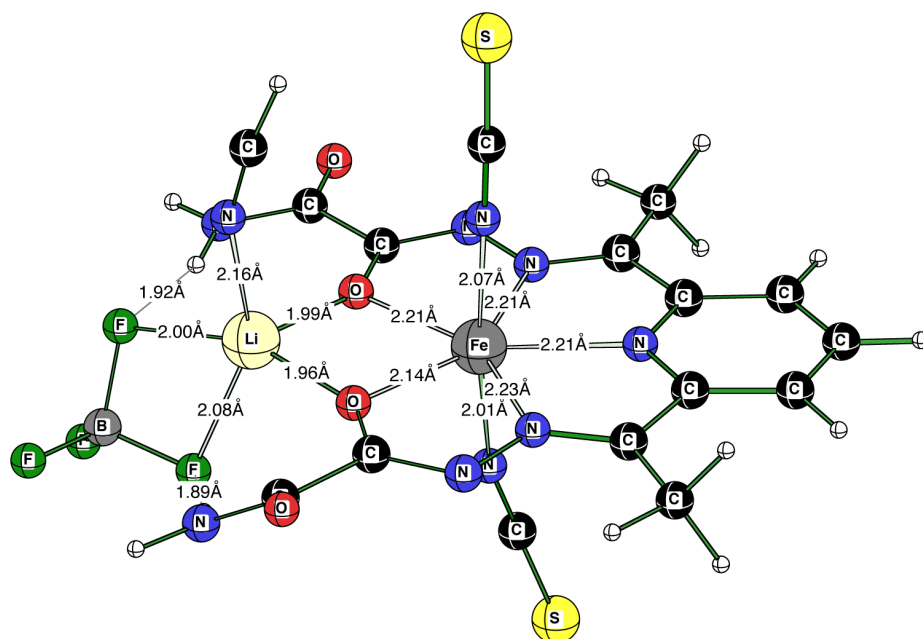


Figure 3.25. Calculated structure (B3LYP/LANL2DZp) of $\{[\text{Fe}(\text{dapsox})(\text{NCS})_2] \cdot \text{LiBF}_4\}^-$.

In the calculated structures, the BF_4^- anion interacts with the seven-coordinate iron complex by forming hydrogen bonds between the fluoride atoms and two hydrogen atoms of the pendant amide groups of the dapsox^{2-} ligand. The two amide parts of the ligand are held in a preorganized arrangement by coordination of the α -oxyazine oxygen atoms to the iron center. They, together with the bound anion, define a pocket of suitable size to host the Li^+ cation. The Li^+ cation binds to the negatively charged α -oxyazine oxygen atoms, solvent molecule and the two fluoride atoms of BF_4^- which closes the tweezerlike pocket.

The F–N bond lengths in the equatorial plane are in excellent agreement with that found in the crystal structure of $[\text{Fe}(\text{dapsox})(\text{H}_2\text{O})_2]\text{ClO}_4$.⁵³ As expected, upon Li^+ coordination, the Fe–O⁻ bonds become longer (2.08 Å, Figure 3.24) than those observed in the crystal structure of $[\text{Fe}(\text{dapsox})(\text{H}_2\text{O})_2]\text{ClO}_4$ (2.046(3) and 2.066(3) Å), due to the partial neutralization of the negative charge of the α -oxyazine oxygen donor atoms. Negative charge of the bridged α -oxyazine oxygen atoms results in somewhat shorter Li–O⁻ bonds (2.01 Å, Figure 3.24) than the ones calculated for $[\text{Li}(\text{H}_2\text{O})_5]^+$ (average $d(\text{Li}-\text{O}) = 2.07 \text{ \AA}$).²⁰¹

The coordination of two SCN^- to the iron center causes elongation of the equatorial Fe–ligand bonds, whereas the elongation of Fe–O⁻ bonds is more prominent than that of the Fe–N bonds. At the same time an increase in electron density upon SCN^- coordination results in somewhat shorter Li–O bonds (Figure 3.25). This is in agreement with the apparently higher LiOTf binding constant for $[\text{Fe}(\text{dapsox})(\text{NCS})_2]^-$, $K^{\text{III}}_{2\text{SCN}}$, than for $[\text{Fe}(\text{dapsox})(\text{CH}_3\text{CN})_2]^+$, K^{III} (Table 3.4). The N–H \cdots F hydrogen bonds are not affected by the changes in the coordination sphere of the more distant iron center.

3.5. Conclusion

It was demonstrated by electrochemical, NMR, kinetic, thermodynamic, spectrophotometric, and DFT studies that the seven-coordinate $[\text{Fe}(\text{dapsox})(\text{CH}_3\text{CN})_2]^+$ complex behaves as a ditopic receptor for lithium salts in acetonitrile (Figure 3.26). The observed apparent binding constants increase in the order $\text{LiOTf} < \text{LiClO}_4 < \text{LiBF}_4$. In the case of LiPF_6 , the solution chemistry is more complex due to the lithium catalyzed PF_6^- hydrolysis processes. However, the electrochemical measurements with LiPF_6 show that the coordination of anionic species (in that case PO_2F_2^- or PO_3F_2^-) to the iron center strongly increases the interactions between the complex and lithium salt and the coupling between the lithium binding and iron reduction. From the kinetic and thermodynamic studies of the reaction between $[\text{Fe}(\text{dapsox})(\text{CH}_3\text{CN})_2]^+$ and SCN^- in the presence of Bu_4NOTf and LiOTf , respectively, it has also been concluded that the increase in the electron density around the iron center upon anion coordination facilitates lithium binding. These experiments show that in nonaqueous medium lithium salts cannot be simply used as supporting electrolytes, since they can affect the kinetic behavior of the studied complex. Mechanistic studies have revealed that the $[\text{Fe}(\text{dapsox})(\text{CH}_3\text{CN})_2]^+$ complex and its mono(thiocyanato) adduct undergo substitution processes according to an associative (A) mechanism. This can be interpreted in terms of the poor donor ability of CH_3CN , where the Fe–NCCH₃ bonds are so labilized that the rate-

determining step has almost only Fe–NCS⁻ bond making character. The higher reactivity of the lithium adduct of the complex also speaks in favor of an associative character of the rate-determining step in the substitution mechanism.

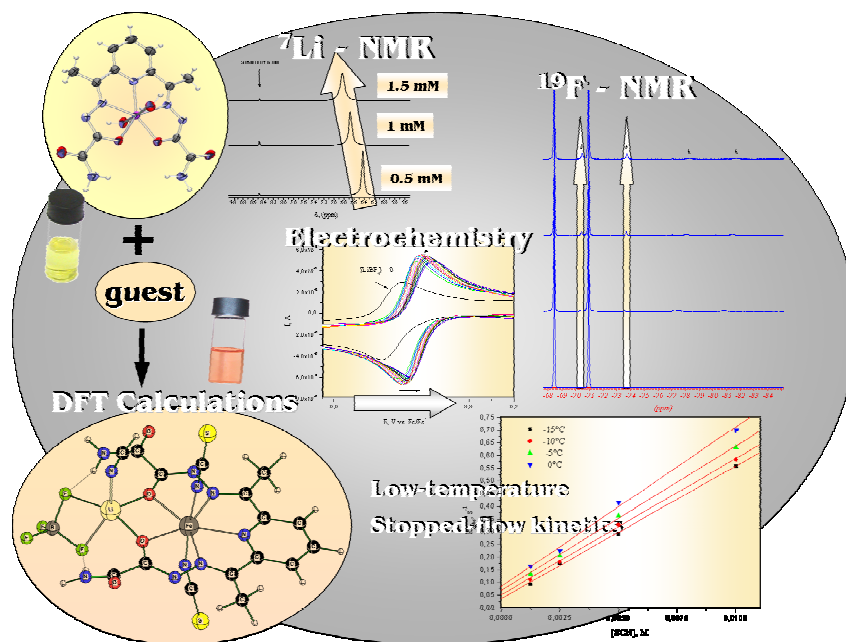


Figure 3.26. The schematic overview of used methods and relevant results.

In conclusion, the seven-coordinate $[\text{Fe}(\text{dapsox})(\text{CH}_3\text{CN})_2]^+$ complex in its Fe^{III} , Fe^{II} , and anion-substituted forms having a shape of “charged tweezers”, is able to intimately associate with lithium salts by means of shape recognition, hydrogen-bond complementarity, and charge assistance. The simulation of an enzymatic active site, which could bind small metal cations and in that way enhance binding of superoxide, could undoubtedly be a desired feature of SOD Mimetics.

4. Summary

The objective of the present work was to study seven-coordinate Fe^{II} and Fe^{III} complexes of acyclic and rigid pentadentate H₂dapsox [H₂dapsox = 2,6-diacetylpyridine-bis(semioxamazide)] ligands in aqueous and nonaqueous media. Since these complexes were proven to be outstanding catalysts for SOD disproportionation, the clarification of the following aspects was of importance:

- ❖ investigations of pressure effects on the thermodynamics of proton-coupled electron-transfer reactions of different complex species in aqueous solution ([Section 2.1](#))
- ❖ establishment of the reaction mechanism over a wide pH range: whether electrons and protons (1H⁺/1e⁻ or 2H⁺/1e⁻) are transferred in one kinetic step (concerted transfer) or separately in a stepwise manner ([Section 2.2](#))
- ❖ studies on the host–guest interactions between the Fe^{II/III}dapsox system and small ions: SOD mimetic as a ditopic receptor in aprotic medium ([Section 3](#))

All listed aspects play an important role in terms of the reactivity of these complexes as synthetic SOD enzymes towards the superoxide anion (see [Section 1](#)).

In [Section 2.1](#), the effect of pressure on proton-coupled electron-transfer reactions of two selected similar seven-coordinate Fe^{III/II}(H₂L)(H₂O)₂ systems [where H₂L = 2,6-diacetylpyridine-bis(semicarbazone) and 2,6-diacetylpyridine-bis(semioxamazide), respectively] was examined for the first time.

The acid–base equilibria of these Fe^{III/II} systems were investigated in detail by spectrophotometric, potentiometric and electrochemical titrations, and the speciation over a wide pH range could be resolved. On the basis of the obtained species distributions, the pH intervals in which the different protonated forms of the two studied systems exist, were defined. In different pH ranges, a different number

of protons (from 0 to 3 protons per electron) can be transferred during the redox process, which affects the change in the overall charge on the complexes.

For all the different protonation forms of the studied complexes, the change in the redox potentials with pressure was measured and the redox reaction volume was obtained by applying high-pressure cyclic voltammetry. This is the first time that the effect of pressure on the redox potential of proton-coupled electron-transfer processes has been studied. The results show that in the case of proton-coupled electron transfer, the reaction volume of the neutralization of protons contributes to the overall reaction volume.

A linear correlation between Δz^2 (change in the square of the charge) and the overall reaction volume of the complexes upon reduction, $\Delta V_{\text{complex}}^0$, was found. The average value of the intrinsic volume change for the selected seven-coordinate iron complexes was estimated from the intercept of the plot of $\Delta V_{\text{complex}}^0$ versus Δz^2 to be $9.2 \pm 0.7 \text{ cm}^3 \text{ mol}^{-1}$. Interestingly, previously reported linear correlations found between Δz^2 and the redox reaction volumes and the neutralization reaction volumes for different types of transition metal complexes, were also observed in the present study in which the two processes were combined. Consequently, the change in overall charge is not only caused by the change in the oxidation state of the metal center but also by protonation/deprotonation of the pentadentate chelate or the coordinated water ligand. Thus, the approximately linear dependence of the reaction volume on Δz^2 seems to have general application and was shown to be valid for proton-coupled electron transfer as well.

In [Section 2.2](#), the insight into the mechanism of the elementary reaction steps over the pH range 1–12 in buffered and unbuffered media was provided. Since the ability of the seven-coordinate Fe^{II} and Fe^{III} complexes of pentadentate H_2dapsox to catalytically decompose the superoxide radical was recently demonstrated, it was important for us to show how the intimate connection between the acid-base equilibria and redox processes can be revealed.

For the first time, all proton-transfer, electron-transfer, and proton-coupled electron transfer steps over a wide pH range were experimentally determined and analyzed. The results of temperature-dependent cyclic voltammetric measurements were used to determine the driving force for the discrete ET as well as PCET elementary steps. Temperature-dependent potentiometric titrations were carried out to clarify the thermodynamics of all PT steps. Results showed that the thermodynamic bias towards the concerted proton-electron transfer is unambiguously established.

Since a major manifestation of the concerted proton-electron transfer is the existence of the deuterium kinetic isotope effect (KIE), the measured heterogeneous rate constants (k_{et}) for the electrode reactions in H_2O and D_2O for the respective complex species were compared. The occurrence of a high isotope effect was detected at a pH where two protons are taken upon electrochemical reduction, hence, the concerted pathway for this process can be considered. If the measurements were performed in buffer, an inverse kinetic isotope effect appeared. The reason for this unusual effect can be caused by the pre-equilibrium between the buffer components and complex species at certain pHs. The understanding of the influence of buffer on such systems requires further investigations.

Relying on the latest evidence that the concerted proton-electron transfer processes might occur in the natural SOD enzymes, the experimentally gained results for their mimetics in this section were analyzed mechanistically to make progress in discarding other possible reaction pathways. The results are important in terms of the action mechanism in superoxide dismutase mimetics.

In [Section 3](#), the host-guest interactions between the seven-coordinate tweezerlike $[Fe(dapsox)(H_2O)_2]ClO_4$ complex with different lithium salts ($LiOTf$, $LiClO_4$, $LiBF_4$ and $LiPF_6$) in CH_3CN have been investigated by 7Li - and ^{19}F NMR spectroscopy as well as by electrochemical, spectrophotometric, kinetic and DFT methods.

It has been demonstrated that this complex acts as ditopic receptor, showing spectral and electrochemical ion pair-sensing capability for different lithium salts. In general,

the apparent binding constants for lithium salts increase in the order $\text{LiOTf} < \text{LiClO}_4 < \text{LiBF}_4$. From the electrochemical measurements the apparent lithium salt binding constants for the Fe^{III} and Fe^{II} forms of the complex have been obtained suggesting a stronger host-guest interaction with the reduced form of the complex.

In the presence of LiPF_6 the solution chemistry is more complex because of the lithium catalyzed hydrolysis of PF_6^- . However, the electrochemical measurements with LiPF_6 show that the coordination of anionic species (in that case PO_2F_2^- or PO_3F_2^-) to the iron center strongly increases the interactions between the complex and lithium salt and the coupling between the lithium binding and iron reduction.

The kinetics of the complexation of $[\text{Fe}(\text{dapsox})(\text{CH}_3\text{CN})_2]^+$ by thiocyanate at $-15\text{ }^\circ\text{C}$ in acetonitrile in the presence of $0.2\text{ M NBU}_4\text{OTf}$ shows two steps with the following rate constants and activation parameters: $k_1 = 411 \pm 14\text{ M}^{-1}\text{ s}^{-1}$; $\Delta H_1^\ddagger = 9 \pm 2\text{ kJ mol}^{-1}$; $\Delta S_1^\ddagger = -159 \pm 6\text{ J K}^{-1}\text{ mol}^{-1}$; $k_2 = 52 \pm 1\text{ M}^{-1}\text{ s}^{-1}$; $\Delta H_2^\ddagger = 4 \pm 1\text{ kJ mol}^{-1}$; $\Delta S_2^\ddagger = -195 \pm 3\text{ J K}^{-1}\text{ mol}^{-1}$. It has been concluded that the increase in the electron density around the iron center upon anion coordination facilitates lithium binding. The very negative ΔS^\ddagger values are consistent with an associative (A) mechanism. Under the same conditions but with 0.2 M LiOTf , $k_{1\text{Li}}$ and $k_{2\text{Li}}$ are $1605 \pm 51\text{ M}^{-1}\text{ s}^{-1}$ and $106 \pm 2\text{ M}^{-1}\text{ s}^{-1}$, respectively. The increased rate constants for the $\{[\text{Fe}(\text{dapsox})(\text{CH}_3\text{CN})_2] \bullet \text{LiOTf}\}^+$ adduct are in agreement with an associative mechanism. This can be interpreted in terms of the poor donor ability of CH_3CN , where the $\text{Fe}-\text{NCCH}_3$ bonds are so labilized that the rate determining step has almost only $\text{Fe}-\text{NCS}^-$ bond making character. The higher reactivity of the lithium adduct of the complex also speaks in favor of an associative character of the rate-determining step in the substitution mechanism.

Kinetic and spectrophotometric titration measurements show stronger interaction between the lithium salt and the anion substituted forms, $[\text{Fe}(\text{dapsox})(\text{CH}_3\text{CN})(\text{NCS})]$ and $[\text{Fe}(\text{dapsox})(\text{NCS})_2]^-$, of the complex. These experiments demonstrate that in nonaqueous medium lithium salts cannot simply be

used as supporting electrolytes, since they can affect the kinetic behavior of the studied complex.

DFT calculations revealed that the negatively charged α -oxyazine oxygen atoms are responsible for cation binding (electrostatic interactions), whereas the two terminal amide groups bind the anion via hydrogen bonding.

In conclusion, the seven-coordinate $[\text{Fe}(\text{dapsox})(\text{CH}_3\text{CN})_2]^+$ complex, in its Fe^{III} , Fe^{II} and anion-substituted forms, having a shape of “charged tweezers”, is able to intimately associate with the lithium salts by means of shape recognition, hydrogen-bond complementarity and charge assistance. The simulation of an enzymatic active site, which could bind small metal cations and in that way enhance binding of superoxide, could undoubtedly be a desired feature of SOD Mimetics.

5. Zusammenfassung

Superoxidradikale ($O_2^{\bullet-}$) entstehen bei der Reduktion molekularen Sauerstoffs in den Mitochondrien, den sogenannten “Kraftwerken” der Zelle, in denen in der Atmungskette ständig sauerstoffhaltige Nährstoffe verbrannt werden. Als Nebenprodukte der Zellatmung entstehen verschiedene reaktive Sauerstoffspezies wie Hydroxylradikale (OH^\bullet), Wasserstoffperoxid (H_2O_2), Ozon (O_3), Hypochlorige Säure (OCl^-) und angeregte Sauerstoffmoleküle (Singulett-Sauerstoff 1O_2). Zwar verfügt der Körper über Mechanismen, um diese aggressiven Spezies abzufangen oder entstandene Schäden zu reparieren, mit der Zeit werden diese Abwehrkräfte jedoch schwächer, und die von den Superoxidradikalen verursachten Schäden nehmen allmählich zu. Mitochondrien sind schon deshalb so gefährdet, weil sie zwar über eigenes Erbgut, aber nicht über die dazugehörigen Reparatursysteme verfügen, weshalb sie im Laufe des Lebens zunehmend absterben. Haben die Superoxoverbindungen einmal die DNA verändert, steigt bereits die Wahrscheinlichkeit an altersbedingten Krankheiten wie Krebs, Arthritis, der Alzheimer-Krankheit und Herzkrankheiten zu leiden. Zur Abwehr gegen den oxidativen Abbau setzt der Körper Schutzenzyme ein.

Somit kommt das Enzym Superoxiddismutase (fortan SOD genannt) in nahezu allen Zellen vor und katalysiert die Umwandlung von Superoxidradikalen zu Sauerstoff (O_2) und Wasserstoffperoxid (H_2O_2). Es handelt sich hierbei um eine Disproportionierungsreaktion. Die in Bakterien lokalisierte SOD enthält im katalytischen Zentrum ein Eisen- oder ein Manganatom. Es sind auch andere Formen von SOD bekannt, welche anstelle von Eisen und Mangan, Kupfer und Zink (Cytoplasma von Eukaryoten) enthalten. Die Fe- und Mn-SOD-Enzyme verfügen über eine trigonal-pyramidale Geometrie und besitzen ähnliche Struktureigenschaften.

Protonen spielen eine wichtige Rolle im vollständigen katalytischen SOD Zyklus. Fe- und Mn-SOD sind imstande, bei der Reduktion von Fe^{III} zu Fe^{II} ein Proton

aufzunehmen, und zwar über den ganzen pH-Bereich verteilt, in dem sie aktiv sind. Das redoxgekoppelte Proton wird dabei vom Metallion abgespalten und ist somit für die reduzierte Form des Substrats zugänglich. So gesehen kann die Reduktion des Substrats als protonengekoppelter (PCET) Redoxprozess bezeichnet werden. Diese Prozesse werfen eine interessante Fragestellung auf, die theoretische wie experimentelle Wissenschaftler gleichermaßen zu verschiedenen Hypothesen anregt: Werden die Protonen und Elektronen während der Redoxreaktion gleichzeitig übertragen oder nacheinander in einzelnen (PT und ET) Schritten?

Seit Ende der 90er Jahre gelten die siebenfach koordinierten Eisen- und Mangankomplexe als hocheffektive SOD-Katalysatoren. Als bessere SOD-Mimetika erwiesen sich dabei die Mn^{II}-Komplexe makrozyklischer Liganden. Es wurde darüber hinaus postuliert, dass ausschließlich siebenfach koordinierte Komplexe makrozyklischer Liganden mit konformativer Flexibilität SOD-Aktivität aufweisen können. Ungeachtet dieser Postulate wurde in einem vor kurzem veröffentlichten Bericht gezeigt, dass die Eisenkomplexe des azyklischen und starren Liganden H₂dapsox [H₂dapsox=2,6-diacetylpyridin-bis(semioxamazid)] Superoxid dismutieren können bzw. Konformationsflexibilität der Komplexe bei der katalytischen SOD-Aktivität keine Rolle spielt. Da die katalytische Disproportionierung von Superoxid Redoxreaktionen zwischen dem Komplex und Superoxid erfordert, ist das detaillierte Verständnis des Redoxverhaltens und der Substitutionsreaktionen von fundamentaler Bedeutung.

Es war von besonderer Wichtigkeit, folgende Aspekte in der vorliegenden Dissertation zu erläutern:

- ❖ Wie ist der Einfluss von Druck auf die Thermodynamik protonengekoppelter Elektronentransferreaktionen verschiedener Komplexspezies in wässrigen Lösungen? (Abschnitt 2.1)

- ❖ Die Aufklärung des Mechanismus elementarer Reaktionsschritte innerhalb eines großen pH-Bereichs: Werden Protonen und Elektronen als separate Teilchen oder in einem Reaktionsschritt übertragen? (Abschnitt 2.2)
- ❖ Die Wirt–Gast Wechselwirkungen zwischen dem Fe^{II/III}dapsox System und kleinen Metallionen: Ist das SOD-Mimetikum ein ditopischer Rezeptor? (Abschnitt 3).

Die Klärung der grundlegenden Prozesse und Wechselwirkungen, in denen die siebenfach koordinierten Komplexe eine Rolle spielen, kann zum Verständnis des SOD Katalyseprozesses beitragen und ein Licht auf die funktionellen Details der effizienten Mimetika werfen.

Im Abschnitt 2.1 wird erstmalig über den Einfluss von Druck auf protonengekoppelte Elektronentransferreaktionen der zwei ausgewählten strukturell ähnlichen siebenfach-koordinierten Fe^{III/II}(H₂L)(H₂O)₂-Komplexe [H₂L = 2,6-Diacetylpyridin-bis(semicarbazon) und 2,6-Diacetylpyridin-bis(semioxamazid)] berichtet.

Die Untersuchung der Säure–Base-Gleichgewichte dieser Fe^{III/II} Systeme mittels spektrophotometrischer, potentiometrischer und elektrochemischer Titrations ermöglichte die Speziesverteilung im pH-Bereich 1–12 zu bestimmen. Basierend auf der Speziesverteilung wurden die pH-Intervalle festgelegt, in denen die verschiedenen protonierten Formen der untersuchten Komplexe in der Lösung vorlagen. Abhängig vom pH-Wert der Lösung können bis zu 3 Protonen pro übertragenes Elektron während der Redoxreaktion übertragen werden, was sich in der unterschiedlichen Gesamtladung der Komplexspezies niederschlägt.

Mithilfe von Elektrochemie (zyklische Voltammetrie) unter erhöhtem Druck war es möglich nicht nur die Änderung der Redoxpotentiale zu verfolgen, sondern auch erstmalig die Reaktionsvolumina unterschiedlich protonierter Komplexspezies zu bestimmen. Die Ergebnisse zeigten, dass der Effekt von hohem Druck auf den Protonentransfer im gesamten protonengekoppelten Prozess dominierte.

Die Ergebnisse zeigten, dass eine lineare Abhängigkeit zwischen der Differenz der Ladungsquadrate ($\Delta z^2 = z_{\text{oxid}}^2 - z_{\text{red}}^2$) und der Änderung des Reaktionsvolumens der Komplexe während der elektrochemischen Reduktion ($\Delta V_{\text{komplex}}^0$) vorliegt. Der Durchschnittswert der Änderung des intrinsischen Volumens ausgewählter siebenfach koordinierter Eisenkomplexe ($9.2 \pm 0.7 \text{ cm}^3 \text{ mol}^{-1}$) ist über die Steigung der $\Delta V_{\text{komplex}}^0$ gegen Δz^2 Korrelation ermittelt worden. Interessanterweise wurde über ähnliche lineare Abhängigkeiten zwischen Δz^2 und den Volumina diskreter Redoxreaktionen sowie den der Neutralisationsreaktionen verschiedener Arten von Übergangsmetalkomplexen berichtet. Da in unserem Fall die Redox- und Neutralisationsprozesse gleichzeitig stattfinden, ist die Änderung der Gesamtladung nicht nur auf die Änderung der Oxidationsstufe des Metallzentrums zurückzuführen, sondern auch auf eine Protonierung bzw. Deprotonierung des Pentadentats oder des koordinierten Wassermoleküls. Somit kann die nahezu lineare Abhängigkeit zwischen dem Reaktionsvolumen und Δz^2 siebenfach koordinierter Eisenkomplexe auf protonengekoppelten Elektronentransferreaktionen verallgemeinert werden.

Im Abschnitt 2.2 wurde der Mechanismus der einzelnen elementaren Reaktionsschritte im pH-Intervall 1-12 in Anwesenheit bzw. Abwesenheit des Puffers aufgeklärt. Da die siebenfach koordinierten Fe^{II} und Fe^{III} Komplexe des H_2dapsox -Pentadentats in der Lage sind, Superoxid katalytisch zu dismutieren, worüber erst kürzlich berichtet wurde, war es von vorwiegender Wichtigkeit zu demonstrieren, wie die Säure–Base-Gleichgewichte das Redoxverhalten beeinflussen können.

Erstmals war es möglich, alle Schritte der Protonentransfer-, Elektronentransfer- und protonengekoppelten Elektronentransferreaktionen in einem großen pH-Bereich experimentell zu verfolgen und anschließend zu analysieren. Während die Ergebnisse der temperaturabhängigen zykelvoltammetrischen Messungen zur Bestimmung der Triebkraft der einzelnen ET- und PCET-Reaktionsschritte herangezogen wurden, lieferten die temperaturabhängigen potentiometrischen Titrations Informationen über die Triebkraft jedes einzelnen PT-Schrittes. Basierend auf den erhaltenen

thermochemischen Parametern liess sich eine Tendenz gegen den konzertierten Transfer der Protonen und Elektronen eindeutig erkennen.

Das zusätzliche Auftreten des kinetischen Isotopeneffektes, welcher sich aus dem Quotienten der heterogenen Reaktionsgeschwindigkeiten (k_{el}) in H_2O und D_2O errechnen lässt, unterstützt diese Tendenz. Denn der deutlich hohe Wert des Isotopeneffekts für die Übertragung von zwei Protonen während der Redoxreaktion zeigt unmissverständlich, dass Elektronen und Protonen in einem Reaktionsschritt simultan übertragen werden.

In Anwesenheit des Puffers wurde ein *inverser* kinetischer Isotopeneffekt beobachtet. Dieser Effekt könnte aufgrund eines zwischen den Pufferkomponenten und der Reaktionsspezies vorgelagerten Gleichgewichts auftreten. Für ein tieferes Verständnis der Puffereinflüsse auf protonengekoppelte Elektronentransferreaktionen wären allerdings weitere gezielte Untersuchungen nötig. Nichtsdestotrotz zeigen die beobachteten Isotopeneffekte zusammen mit den thermodynamischen Parametern, dass die PCET-Prozesse im Falle unserer siebenfach koordinierten Komplexe konzertiert ablaufen, und nicht stufenweise. Das sind sehr interessante Ergebnisse, die nahe legen, dass ein konzertierter PCET eine effiziente SOD-Katalyse unterstützt. Basierend auf dieser Beobachtung können wir die Existenz eines konzertierten PCET-Mechanismus im Katalysezyklus der SOD-Enzyme postulieren.

Im Abschnitt 3 wurden die Wirt–Gast-Wechselwirkungen zwischen dem siebenfach koordinierten pinzettenartigen $[Fe(dapsox)(H_2O)_2]ClO_4$ -Komplex mit verschiedenen Lithiumsalzen ($LiOTf$, $LiClO_4$, $LiBF_4$ and $LiPF_6$) in Acetonitril mittels 7Li - und ^{19}F NMR-Spektroskopie, sowie weiterer elektrochemischer, spektrophotometrischer, kinetischer und DFT Methoden untersucht.

Der Komplex demonstrierte spektrale und elektrochemische Fähigkeiten zur Erkennung verschiedener Ionenpaare und wies somit Eigenschaften eines ditopischen Rezeptors auf. Generell stiegen die Werte der Bindungskonstanten in der Reihenfolge $LiOTf < LiClO_4 < LiBF_4$ an. Elektrochemische Messungen lieferten die

Bindungskonstanten für die Fe^{III}- und Fe^{II}-Formen des Komplexes. Dabei wurden die stärkeren Wechselwirkungen zwischen den Lithiumsalzen und der reduzierten Form veranschaulicht.

Die Zugabe von LiPF₆ zur Komplexlösung führte zur Hydrolyse des PF₆⁻ Anions, katalysiert durch das Lithiumkation. Dennoch zeigten die elektrochemischen Messungen, dass die Koordination der anionischen Spezies (PO₂F₂⁻ oder PO₃F₂⁻) zum Metallzentrum die Wechselwirkungen zwischen dem Komplex und den Lithiumsalzen erhöht. Ausserdem wird dadurch die Kopplung zwischen der Bindung des Lithiumkations und der Reduktion des Eisens verstärkt.

Die Kinetik der Komplexierung des [Fe(dapsox)(CH₃CN)₂]⁺ Komplexes mit Thiocyanat wurde bei -15 °C in Acetonitril verfolgt. In Anwesenheit von 0.2 M Bu₄NOTf wurden zwei Reaktionsschritte beobachtet und die folgenden Geschwindigkeitskonstanten sowie die Aktivierungsparameter bestimmt: $k_1 = 411 \pm 14 \text{ M}^{-1}\text{s}^{-1}$; $\Delta H_1^\ddagger = 9 \pm 2 \text{ kJ mol}^{-1}$; $\Delta S_1^\ddagger = -159 \pm 6 \text{ J K}^{-1} \text{ mol}^{-1}$; $k_2 = 52 \pm 1 \text{ M}^{-1}\text{s}^{-1}$; $\Delta H_2^\ddagger = 4 \pm 1 \text{ kJ mol}^{-1}$; $\Delta S_2^\ddagger = -195 \pm 3 \text{ J K}^{-1} \text{ mol}^{-1}$. Die stark negativen Werte für ΔS^\ddagger deuten auf einen Substitutionsmechanismus assoziativer (A) Natur hin.

Zwar unter den gleichen Bedingungen, aber mit 0.2 M LiOTf wurden folgende Geschwindigkeitskonstanten ermittelt: $k_{\text{Li}} = 1605 \pm 51 \text{ M}^{-1}\text{s}^{-1}$ und $k_{2\text{Li}} = 106 \pm 2 \text{ M}^{-1}\text{s}^{-1}$. Die höheren Geschwindigkeitskonstanten für das {[Fe(dapsox)(CH₃CN)₂]•LiOTf}⁺-Addukt stimmen mit dem assoziativen Mechanismus überein. Das nahe dem Eisenzentrum gebundene Lithiumkation senkt die Elektronendichte am Metallzentrum und steigert folglich seine Elektrophilie und Reaktivität gegenüber anionischen Spezies.

Aus den Ergebnissen der kinetischen und spektrophotometrischen Titrationsen ging hervor, dass die Wechselwirkungen zwischen dem Lithiumsalz und der durch das NCS⁻ Anion substituierten [Fe(dapsox)(CH₃CN)(NCS)]⁻ und [Fe(dapsox)(NCS)₂]⁻-Komplexspezies stärker wurden. Daher wäre es nicht empfehlenswert, lithiumhaltige

Salze als Leitsalze in nichtwässrigen Lösungen zu benutzen, da deren Anwesenheit das kinetische Verhalten der untersuchten Metallkomplexe beeinflusst.

DFT-Rechnungen bestätigten, dass das Lithiumkation aufgrund elektrostatischer Wechselwirkungen zu den negativ geladenen α -Oxyazin-Sauerstoffatomen an diese gebunden wurde. Zugleich knüpften zwei amidische NH_2 -Gruppen Wasserstoffbrückenbindungen zum Anion.

Somit wurde klar, dass sich unsere Fe^{III} -, Fe^{II} - und die durch das NCS^- -Anion substituierten Komplexspezies in Acetonitril als Lithiumrezeptoren verhalten, die durch selektive Erkennung der Gestalt, Wasserstoffbrückenbindungen und ladungsunterstützte Steuerung eine enge Assoziierung mit den Lithiumsalzen ermöglichen. Die Simulation eines enzymatischen aktiven Zentrums, das fähig ist, kleine Metallkationen zu binden und so die Bindungsfähigkeit von Superoxid zu erhöhen, wäre zweifellos ein gewünschtes Merkmal eines SOD Mimetikums.

6. References

- (1) Fridovich, I., *J. Biol. Chem.* **1989**, 264, 7761-7764.
- (2) Fridovich, I., *Ann. Rev. of Biochem.* **1995**, 64, 97-112.
- (3) Fridovich, I., *Ann. N. Y. Acad. Sci.* **1999**, 893, 13-18.
- (4) Flint, D. H.; Tuminello, J. F.; Emptage, M. H., *J. Biol. Chem.* **1993**, 268, 22369-22376.
- (5) Das, U. N., *Eur. J. Clin. Nutr.* **2004**, 58, 195-203.
- (6) Janero, D. R.; Burghardt, B., *Lipids.* **1989**, 24, 125-131.
- (7) Chan, P. H.; Fishman, R. A., *J. Neurochem.* **1980**, 35, 1004- 1007.
- (8) Flyunt, R.; Makogon, O.; Naumov, S.; Schoeneich, C.; Asmus, K.-D., *J. Phys. Chem. A.* **2007**, 111, 11618-11625.
- (9) Yanagisawa, H.; Sato, M.; Nodera, M.; Wada, O., *J. Hypertens.* **2004**, 22, 543-550.
- (10) Sato, M.; Yanagisawa, H.; Nojima, Y.; Tamura, J.; Wada, O., *Clin. Exp. Hypertens.* **2002**, 24, 355-370.
- (11) Kurzelewski, M.; Czarnowska, E.; Beresewicz, A., *J. Physiol. and Pharmacol.* **2005**, 56, 163-178.
- (12) Kocaturk, P. A.; Akbostanci, M. C.; Tan, F.; Kavas, G. O., *Pathophysiology.* **2000**, 7, 63-67.
- (13) Ihara, Y.; Chuda, M.; Kuroda, S.; Hayabara, T., *J. Neur. Scis.* **1999**, 170, 90-95.
- (14) De Leo, M. E.; Borrello, S.; Passantino, M.; Palazzotti, B.; Mordente, A.; Daniele, A.; Filippini, V.; Galeotti, T.; Masullo, C., *Neurosci. Lett.* **1998**, 250, 173-176.
- (15) Marklund, S. L.; Adolfsson, R.; Gottfries, C. G.; Winblad, B., *J. Neurol. Sci.* **1985**, 67, 319-325.
- (16) Toh, Y.; Kuninaka, S.; Mori, M.; Oshiro, T.; Ikeda, Y.; Nakashima, H.; Baba, H.; Kohnoe, S.; Okamura, T.; Sugimachi, K., *Oncology.* **2000**, 59, 223-228.
- (17) Burdon, R. H., *Free Radical Biol. Med.* **1995**, 18, 775-794.

- (18) Oxidative Stress - Technical Overview.
http://www.merckbiosciences.co.uk/html/cbc/oxidative_stress.htm
- (19) Adams, M. W. W.; Jenney, F. E., Jr.; Clay, M. D.; Johnson, M. K., *JBIC.* **2002**, *7*, 647-652.
- (20) Auchere, F.; Rusnak, F., *JBIC.* **2002**, *7*, 664-667.
- (21) Miller, A.-F., *Curr. Opin.Chem.Biol.* **2004**, *8*, 162-168.
- (22) Niviere, V.; Fontecave, M., *JBIC.* **2004**, *9*, 119-123.
- (23) Kurtz, D. M., Jr., *Acc. Chem. Res.* **2004**, *37*, 902-908.
- (24) Kurtz, D. M., *J. of Inorg. Biochem.* **2006**, *100*, 679-693.
- (25) Miller, A.-F., *Handbook of Metalloproteins.* **2001**, *1*, 668-682.
- (26) Wuerges, J.; Lee, J.-W.; Yim, Y.-I.; Yim, H.-S.; Kang, S.-O.; Carugo, K. D., *PNAS.* **2004**, *101*, 8569-8574.
- (27) Jackson, T. A.; Brunold, T. C., *Acc. Chem. Res.* **2004**, *37*, 461- 470.
- (28) Yikilmaz, E.; Porta, J.; Grove, L. E.; Vahedi-Faridi, A.; Bronshteyn, Y.; Brunold, T. C.; Borgstahl, G. E. O.; Miller, A.-F., *J. Am. Chem. Soc.* **2007**, *129*, 9927-9940.
- (29) Superoxide Dismutase (SOD) and Oxidative Stress.
http://www.sigmaaldrich.com/Area_of_Interest/Biochemicals/Enzyme_Explorer/Cell_Signaling_Enzymes/Superoxide_Dismutase.html
- (30) Vance, C. K.; Miller, A.-F., *Biochemistry.* **2001**, *40*, 13079-13087.
- (31) Vance, C. K.; Miller, A. F., *J. Am. Chem. Soc.* **1998**, *120*, 461-467.
- (32) Cocco, D.; Calabrese, L.; Finazzi-Agro, A.; Rotilio, G., *Biochim. Biophys. Acta.* **1983**, *746*, 61-64.
- (33) Zaric, S. D.; Popovic, D. M.; Knapp, E.-W., *Chem.--Eur. J.* **2000**, *6*, 3935-3942.
- (34) Zhou, Y.-H.; Fu, H.; Zhao, W.-X.; Chen, W.-L.; Su, C.-Y.; Sun, H.; Ji, L.-N.; Mao, Z.-W., *Inorg. Chem.* **2007**, *46*, 734-739.
- (35) Miller, A.-F.; Padmakumar, K.; Sorkin, D. L.; Karapetian, A.; Vance, C. K., *J. Inorg. Biochem.* **2003**, *93*, 71-83.
- (36) Bull, C.; Fee, J. A., *J. Am. Chem. Soc.* **1985**, *107*, 3295-3304.

- (37) Roth, J. P.; Yoder, J. C.; Won, T.-J.; Mayer, J. M., *Science*. **2001**, *294*, 2524-2526.
- (38) Tommos, C.; Babcock, G. T., *Biochim. Biophys. Acta*. **2000**, *1458*, 199-219.
- (39) Huynh, M. H. V.; Meyer, T. J., *Chemical Reviews (Washington, DC, United States)*. **2007**, *107*, 5004-5064.
- (40) Cukier, R. I.; Nocera, D. G., *Annu. Rev. Phys. Chem.* **1998**, *49*, 337-369.
- (41) Ferguson-Miller, S.; Babcock, G. T., *Chem. Rev.* **1996**, *96*, 2889-2907.
- (42) Hoganson, C. W.; Tabcock, G. T., *Science*. **1997**, *277*, 1953-1956.
- (43) Carrasco, R.; Morgenstern-Badarau, I.; Cano, J., *Inorg. Chim. Acta*. **2007**, *360*, 91-101.
- (44) Liochev, S. I.; Fridovich, I., *IUBMB Life*. **1999**, *48*, 157-161.
- (45) Salvemini, D.; Riley, D. P.; Cuzzocrea, S., *Nat. Rev. Drug Discovery*. **2002**, *1*, 367-374.
- (46) Muscoli, C.; Cuzzocrea, S.; Riley, D. P.; Zweier, J. L.; Thiemermann, C.; Wang, Z.-Q.; Salvemini, D., *Br. J. of Pharmacol.* **2003**, *140*, 445-460.
- (47) Riley, D. P., *Chem. Rev.* **1999**, *99*, 2573-2587.
- (48) Aston, K.; Rath, N.; Naik, A.; Slomczynska, U.; Schall, O. F.; Riley, D. P., *Inorg. Chem.* **2001**, *40*, 1779-1789.
- (49) Riley, D. P.; Lennon, P. J.; Neumann, W. L.; Weiss, R. H., *J. Am. Chem. Soc.* **1997**, *119*, 6522-6528.
- (50) Zhang, D.; Busch, D. H.; Lennon, P. L.; Weiss, R. H.; Neumann, W. L.; Riley, D. P., *Inorg. Chem.* **1998**, *37*, 956-963.
- (51) Riley, D. P., *Adv. Inorg. Chem.* **2007**, *59*, 233-263.
- (52) Liu, G.-F.; Filipovic, M.; Heinemann, F. W.; Ivanović-Burmazović, I., *Inorg. Chem.* **2007**, *46*, 8825-8835.
- (53) Andjelkovic, K.; Bacchi, A.; Pelizzi, G.; Jeremic, D.; Ivanović-Burmazović, I., *J. Coord. Chem.* **2002**, *55*, 1385-1392.
- (54) Sarauli, D.; Meier, R.; Liu, G.-F.; Ivanović-Burmazović, I.; Van Eldik, R., *Inorg. Chem.* **2005**, *44*, 7624-7633.

- (55) Ivanović-Burmazović, I.; Hamza, M. S. A.; van Eldik, R., *Inorg. Chem.* **2002**, *41*, 5150-5161.
- (56) Chang, C. J.; Chang, M. C. Y.; Damrauer, N. H.; Nocera, D. G., *Biochim. Biophys. Acta.* **2004**, *1655*, 13-28.
- (57) Babcock, G. T.; Wikstrom, M., *Nature.* **1992**, *356*, 301-309.
- (58) Faller, P.; Goussias, C.; Rutherford, A. W.; Un, S., *PNAS.* **2003**, *100*, 8732-8735.
- (59) Roth, J. P.; Lovell, S.; Mayer, J. M., *J. Am. Chem. Soc.* **2000**, *122*, 5486-5498.
- (60) Malmstroem, B. G., *Acc. Chem. Res.* **1993**, *26*, 332-338.
- (61) Brewer, C.; Brewer, G.; Lockett, C.; Marbury, G. S.; Viragh, C.; Beatty, A. M.; Scheidt, W. R., *Inorg. Chem.* **2004**, *43*, 2402-2415.
- (62) Lambert, F.; Policar, C.; Durot, S.; Cesario, M.; Yuwei, L.; Korri-Youssoufi, H.; Keita, B.; Nadjjo, L., *Inorg. Chem.* **2004**, *43*, 4178-4188.
- (63) Ivanović-Burmazović, I.; Andjelkovic, K., *Advances in Inorg. Chem.* **2004**, *55*, 315-360.
- (64) Palenik, G. J.; Wester, D. W.; Rychlewska, U.; Palenik, R. C., *Inorg. Chem.* **1976**, *15*, 1814-1819.
- (65) Bino, A.; Frim, R.; Van Genderen, M., *Inorg. Chim. Acta.* **1987**, *127*, 95-101.
- (66) Hills, G. J.; Hsieh, S., *Chem. Ing. Tech.* **1972**, *44*, 216-218.
- (67) Swaddle, T. W.; Tregloan, P. A., *Coord. Chem. Rev.* **1999**, *187*, 255-289.
- (68) Drude, P.; Nernst, W., *Z. Phys. Chem.* **1894**, *15*, 79.
- (69) Tran, D.; Hunt, J. P.; Wherland, S., *Inorg. Chem.* **1992**, *31*, 2460-2464.
- (70) Matsumoto, M.; Swaddle, T. W., *Inorg. Chem.* **2004**, *43*, 2724-2735.
- (71) Sachinidis, J. I.; Shalders, R. D.; Tregloan, P. A., *Inorg. Chem.* **1996**, *35*, 2497-2503.
- (72) Sachinidis, J. I.; Shalders, R. D.; Tregloan, P. A., *Inorg. Chem.* **1994**, *33*, 6180-6186.
- (73) Bajaj, H. C.; Tregloan, P. A.; van Eldik, R., *Inorg. Chem.* **2004**, *43*, 1429-1435.

- (74) Macpherson, B. P.; Alzoubi, B. M.; Bernhardt, P. V.; Martinez, M.; Tregloan, P. A.; van Eldik, R., *Dalton Trans.* **2005**, 1459-1467.
- (75) Kitamura, Y.; Van Eldik, R., *Ber. Buns.Ges.* **1984**, 88, 418-422.
- (76) Britton, H. T. S.; Robinson, R. A., *J. Chem. Soc.* **1931**, 1456-1462.
- (77) Gran, G., *Analyst.* **1952**, 77, 661-671.
- (78) Gran, G., *Anal. Chim. Acta.* **1988**, 206, 111-123.
- (79) Zuberbuehler, A. D.; Kaden, T. A., *Talanta.* **1982**, 29, 201-206.
- (80) Slattery, S. J.; Blaho, J. K.; Lehnes, J.; Goldsby, K. A., *Coord. Chem.Rev.* **1998**, 174, 391-416.
- (81) Meier, R., *EFIT - A General Program for Evaluation of Metal Complex Equilibrium Constants from Redox Potential Data*. Berlin, 1999.
- (82) Kitamura, Y.; Itoh, T., *J. Sol. Chem.* **1987**, 16, 715-725.
- (83) *GPES: General Purpose Electrochemical System for Windows*, Version 4.9; Utrecht, The Netherlands, 2001.
- (84) Fu, Y.; Swaddle, T. W., *J. Am. Chem. Soc.* **1997**, 119, 7137-7144.
- (85) Huheey, J. E., *Inorg. Chem. 3rd Ed.* 1983; p 936 pp.
- (86) Sun, J.; Wishart, J. F.; van Eldik, R.; Shalders, R. D.; Swaddle, T. W., *J. Am. Chem. Soc.* **1995**, 117, 2600-2605.
- (87) Millero, F. J., *Water and Aqueous Solutions; Structure, Thermodynamics and Transport Properties*. Wiley-Interscience: New York, 1972.
- (88) Millero, F. J.; Hoff, E. V.; Kahn, L., *J. Sol.Chem.* **1972**, 1, 309-327.
- (89) Stokes, R. H.; Robinson, R. A., *Trans. Faraday Soc.* **1957**, 53, 301-304.
- (90) Li, J.; Fisher, C. L.; Chen, J. L.; Bashford, D.; Noodleman, L., *Inorg. Chem.* **1996**, 35, 4694-4702.
- (91) Palenik, G. J.; Wester, D. W., *Inorg. Chem.* **1978**, 17, 864-870.
- (92) Sommerer, S. O.; Baker, J. D.; Zerner, M. C.; Palenik, G. J., *Inorg. Chem.* **1992**, 32, 563-567.
- (93) Jackson, T. A.; Karapetian, A.; Miller, A.-F.; Brunold, T. C., *J. Am. Chem. Soc.* **2004**, 126, 12477-12491.
- (94) Sawyer, D. T.; Valentine, J. S., *Acc. Chem. Res.* **1981**, 14, 393- 400.

- (95) Bernat, G.; Morvaridi, F.; Feyziyev, Y.; Styring, S., *Biochemistry*. **2002**, *41*, 5830-5843.
- (96) Westphal, K. L.; Lydakis-Simantiris, N.; Cukier, R. I.; Babcock, G. T., *Biochemistry*. **2000**, *39*, 16220-16229.
- (97) Jiang, S.; Liu, J.; Shi, Y.; Wang, Z.; Aakermark, B.; Sun, L., *Dalt. Trans.* **2007**, 896-902.
- (98) Styring, S.; Feyziyev, Y.; Mamedov, F.; Hillier, W.; Babcock, G. T., *Biochemistry*. **2003**, *42*, 6185-6192.
- (99) Hammarstrom, L., *Curr. Opin. Chem. Biol.* **2003**, *7*, 666-673.
- (100) Cukier, R. I., *J. Phys. Chem. B.* **2002**, *106*, 1746-1757.
- (101) Soper, J. D.; Mayer, J. M., *J. Am. Chem. Soc.* **2003**, *125*, 12217-12229.
- (102) Mayer, J. M.; Rhile, I. J., *Biochim. Biophys. Acta.* **2004**, *1655*, 51-58.
- (103) Shan, X.; Que, L., Jr., *PNAS.* **2005**, *102*, 5340-5345.
- (104) Belevich, I.; Verkhovsky, M. I.; Wikstroem, M., *Nature.* **2006**, *440*, 829-832.
- (105) Song, Y.; Michonova-Alexova, E.; Gunner, M. R., *Biochemistry.* **2006**, *45*, 7959-7975.
- (106) Song, Y.; Mao, J.; Gunner, M. R., *Biochemistry.* **2006**, *45*, 7949-7958.
- (107) Saveant, J.-M., *J. Phys. Chem. C.* **2007**, *111*, 2819-2822.
- (108) Costentin, C.; Robert, M.; Saveant, J.-M., *J. Am. Chem. Soc.* **2007**, *129*, 5870-5879.
- (109) Costentin, C.; Robert, M.; Saveant, J.-M., *J. Am. Chem. Soc.* **2007**, *129*, 9953-9963.
- (110) Costentin, C.; Robert, M.; Saveant, J.-M., *J. Am. Chem. Soc.* **2006**, *128*, 4552-4553.
- (111) Lomoth, R.; Magnuson, A.; Sjoedin, M.; Huang, P.; Styring, S.; Hammarstroem, L., *Photosynth. Res.* **2006**, *87*, 25-40.
- (112) Rhile, I. J.; Markle, T. F.; Nagao, H.; DiPasquale, A. G.; Lam, O. P.; Lockwood, M. A.; Rotter, K.; Mayer, J. M., *J. Am. Chem. Soc.* **2006**, *128*, 6075-6088.

- (113) Sjoedin, M.; Irebo, T.; Utas, J. E.; Lind, J.; Merenyi, G.; Aakermark, B.; Hammarstroem, L., *J. Am. Chem. Soc.* **2006**, *128*, 13076-13083.
- (114) Concepcion, J. J.; Brennaman, M. K.; Deyton, J. R.; Lebedeva, N. V.; Forbes, M. D. E.; Papanikolas, J. M.; Meyer, T. J., *J. Am. Chem. Soc.* **2007**, *129*, 6968-6969.
- (115) Matasovic, B.; Bonifacic, M., *J. Phys. Chem. A* **2007**, *111*, 8622-8628.
- (116) Cowley, R. E.; Bontchev, R. P.; Sorrell, J.; Sarracino, O.; Feng, Y.; Wang, H.; Smith, J. M., *J. Am. Chem. Soc.* **2007**, *129*, 2424-2425.
- (117) Narvaez, A. J.; Voevodskaya, N.; Thelander, L.; Graeslund, A., *J. Biol. Chem.* **2006**, *281*, 26022-26028.
- (118) Shearer, J.; Zhang, C. X.; Zakharov, L. N.; Rheingold, A. L.; Karlin, K. D., *J. Am. Chem. Soc.* **2005**, *127*, 5469-5483.
- (119) Maliekal, J.; Karapetian, A.; Vance, C.; Yikilmaz, E.; Wu, Q.; Jackson, T.; Brunold, T. C.; Spiro, T. G.; Miller, A.-F., *J. Am. Chem. Soc.* **2002**, *124*, 15064-15075.
- (120) Mayer, J. M.; *Annu. Rev. Phys. Chem.* **2004**, *55*, 363-390.
- (121) Shafirovich, V. Y.; Courtney, S. H.; Ya, N.; Geacintov, N. E., *J. Am. Chem. Soc.* **1995**, *117*, 4920-4929.
- (122) Ishikita, H.; Soudackov, A. V.; Hammes-Schiffer, S., *J. Am. Chem. Soc.* **2007**, *129*, 11146-11152.
- (123) Meyer, T. J.; Huynh, M. H. V.; Thorp, H. H., *Angew. Chem., Int. Ed.* **2007**, *46*, 5284-5304.
- (124) Irebo, T.; Reece, S. Y.; Sjoedin, M.; Nocera, D. G.; Hammarstroem, L., *J. Am. Chem. Soc.* **2007**, *129*, 15462-15464.
- (125) Fecenko, C. J.; Thorp, H. H.; Meyer, T. J., *J. Am. Chem. Society.* **2007**, *129*, 15098-15099.
- (126) Costentin, C.; Robert, M.; Saveant, J.-M., *J. Electroanal. Chem.* **2006**, *588*, 197-206.
- (127) Costentin, C.; Evans, D. H.; Robert, M.; Saveant, J.-M.; Singh, P. S., *J. Am. Chem. Soc.* **2005**, *127*, 12490-12491.

- (128) Haddox, R. M.; Finklea, H. O., *J. Phys.Chem. B.* **2004**, *108*, 1694-1700.
- (129) Lehmann, M. W.; Evans, D. H., *J. Phys.Chem. B.* **2001**, *105*, 8877-8884.
- (130) Makarycheva-Mikhailova, A. V.; Stanbury, D. M.; McKee, M. L., *J. Phys. Chem. B.* **2007**, *111*, 6942-6948.
- (131) Costentin, C.; Robert, M.; Saveant, J.-M., *J. Am.Chem. Soc.* **2006**, *128*, 8726-8727.
- (132) Perrin, D. D.; Dempsey, B., *Buffers for pH and Metal Ion Control*. Chapman and Hall: New York, 1974.
- (133) Laviron, E., *J. Electroanal. Chem.* **1981**, *124*, 1-7.
- (134) Laviron, E., *J. Electroanal. Chem.* **1981**, *124*, 9-17.
- (135) Constable, E. C., *Metals and ligand reactivity*. 1990; p 246 pp.
- (136) Fukada, H.; Takahashi, K., *Proteins: Struct., Funct., Genet.* **1998**, *33*, 159-166.
- (137) Goldberg, R. N.; Kishore, N.; Lennen, R. M., *J. Phys. Chem. Ref. Data.* **2002**, *31*, 231-370.
- (138) Nicholson, R. S., *Anal. Chem.* **1965**, *37*, 1351-1355.
- (139) Swaddle, T. W., *Chem. Rev.* **2005**, *105*, 2573-2608.
- (140) Schmitz, J. E. J.; Van der Linden, J. G. M., *Anal. Chem.* **1982**, *54*, 1879-1880.
- (141) Uhrhammer, D.; Schultz, F. A., *Inorg. Chem.* **2004**, *43*, 7389-7395.
- (142) Ford, D. M., *J. Am. Chem. Soc.* **2005**, *127*, 16167-16170.
- (143) Hunter, C. A.; Tomas, S., *Chem. Biol.* **2003**, *10*, 1023-1032.
- (144) Liu, L.; Guo, Q.-X., *Chem. Rev.* **2001**, *101*, 673-695.
- (145) Lumry, R., *Biophys. Chem.* **2003**, *105*, 545-557.
- (146) Starikov, E. B.; Norden, B., *J. Phys. Chem. B. ACS ASAP*.
- (147) Sarauli, D.; Popova, V.; Zahl, A.; Puchta, R.; Ivanović-Burmazović, I., *Inorg. Chem.* **2007**, *46*, 7848-7860.
- (148) Ivanović-Burmazović, I.; Hamza, M. S. A.; Van Eldik, R., *Inorg. Chem.* **2006**, *45*, 1575-1584.
- (149) McClune, G. J. *Iron catalyzed superoxide dismutation*; University of Michigan: Ann Arbor, MI, 1979, From: *Diss. Abstr. Int. B.* *40*, 2175.

- (150) Duerr, K.; Macpherson, B. P.; Warratz, R.; Hampel, F.; Tuczec, F.; Helmreich, M.; Jux, N.; Ivanović-Burmazović, I., *J. Am. Chem. Society.* **2007**, *129*, 4217-4228.
- (151) Grigoriev, V. A.; Cheng, D.; Hill, C. L.; Weinstock, I. A., *J. Am. Chem. Soc.* **2001**, *123*, 5292-5307.
- (152) Curtis, J. C.; Inagaki, M.; Chun, S. J.; Eskandari, V.; Luo, X.; Pan, Z. N.; Sankararaman, U.; Pengra, G. E.; Zhou, J.; Hailey, P.; Laurent, J.; Utalan, D., *Chem. Phys.* **2006**, *326*, 43-53.
- (153) Beer, P. D.; Gale, P. A.; Chen, G. Z., *J. Chem. Soc., Dalton Trans: Inorg. Chem.* **1999**, 1897-1910.
- (154) Bu, J.; Lilienthal, N. D.; Woods, J. E.; Nohrden, C. E.; Hoang, K. T.; Truong, D.; Smith, D. K., *J. Am. Chem. Soc.* **2005**, *127*, 6423-6429.
- (155) Prins, L. J.; Reinhoudt, D. N.; Timmerman, P., *Angew. Chem. Int. Ed.* **2001**, *40*, 2382-2426.
- (156) Rudner, M. S.; Jeremic, S.; Petterson, K. A.; Kent, D. R.; Brown, K. A.; Drake, M. D.; Goddard, W. A., III; Roberts, J. D., *J. Phys. Chem. A.* **2005**, *109*, 9076-9082.
- (157) Corbett, P. T.; Leclaire, J.; Vial, L.; West, K. R.; Wietor, J.-L.; Sanders, J. K. M.; Otto, S., *Chem. Rev.* **2006**, *106*, 3652-3711.
- (158) Evans, A. J.; Beer, P. D., *Dalton Trans.* **2003**, 4451-4456.
- (159) Mahoney, J. M.; Beatty, A. M.; Smith, B. D., *Inorg. Chem.* **2004**, *43*, 7617-7621.
- (160) Mahoney, J. M.; Stucker, K. A.; Jiang, H.; Carmichael, I.; Brinkmann, N. R.; Beatty, A. M.; Noll, B. C.; Smith, B. D., *J. Am. Chem. Society.* **2005**, *127*, 2922-2928.
- (161) Lankshear, M. D.; Cowley, A. R.; Beer, P. D., *Chem. Comm.* **2006**, 612-614.
- (162) Cousins, G. R. L.; Furlan, R. L. E.; Ng, Y.-F.; Redman, J. E.; Sanders, J. K. M., *Angew. Chem., Int. Ed.* **2001**, *40*, 423-428.
- (163) Guo, D.; Han, G.; Duan, C.-y.; Pang, K.-l.; Meng, Q.-j., *Chem. Comm.* **2002**, 1096-1097.

- (164) Furlan, R. L. E.; Ng, Y.-F.; Otto, S.; Sanders, J. K. M., *J. Am. Chem. Soc.* **2001**, *123*, 8876-8877.
- (165) Christian, G. D., *J. Pharm. Biomed. Analysis.* **1996**, *14*, 899-908.
- (166) Christian, G. D., *Sensors.* **2002**, *2*, 432-435.
- (167) Srinivasan, C.; Toon, J.; Amari, L.; Abukhdeir, A. M.; Hamm, H.; Geraldles, C. F. G. C.; Ho, Y.-K.; Mota de Freitas, D., *J. Inorg. Biochem.* **2004**, *98*, 691-701.
- (168) Layden, B. T.; Abukhdeir, A. M.; Malarkey, C.; Oriti, L. A.; Salah, W.; Stigler, C.; Geraldles, C. F. G. C.; Mota de Freitas, D., *Biochim. Biophys. Acta.* **2005**, *1741*, 339-349.
- (169) Sastre, E.; Nicolay, A.; Bruguerolle, B.; Portugal, H., *Life Sci.* **2005**, *77*, 758-767.
- (170) Parker, M. S.; Parker, S. L.; Kane, J. K., *Regul. Pept.* **2004**, *118*, 67-74.
- (171) Dees, A.; Zahl, A.; Puchta, R.; van Eikema Hommes, N. J. R.; Heinemann, F. W.; Ivanović-Burmazović, I., *Inorg. Chem.* **2007**, *46*, 2459-2470.
- (172) Summa, N.; Maigut, J.; Puchta, R.; van Eldik, R., *Inorg. Chem.* **2007**, *46*, 2094-2104.
- (173) Summa, N.; Schiessl, W.; Puchta, R.; van Eikema Hommes, N.; van Eldik, R., *Inorg. Chem.* **2006**, *45*, 2948-2959.
- (174) Puchta, R.; Meier, R.; van Eikema Hommes, N. J. R.; van Eldik, R., *Eur. J. Inorg. Chem.* **2006**, 4063-4067.
- (175) Puchta, R.; van Eikema Hommes, N.; Meier, R.; van Eldik, R., *Dalton Trans.* **2006**, 3392-3395.
- (176) Illner, P.; Zahl, A.; Puchta, R.; van Eikema Hommes, N.; Wasserscheid, P.; van Eldik, R., *J. Organomet. Chem.* **2005**, *690*, 3567-3576.
- (177) M. J. Frisch, G. W. T., H. B. Schlegel, G. E. Scuseria, M. A. Robb, J. R. Cheeseman, J. A. Montgomery, Jr., T. Vreven, K. N. Kudin, J. C. Burant, J. M. Millam, S. S. Iyengar, J. Tomasi, V. Barone, B. Mennucci, M. Cossi, G. Scalmani, N. Rega, G. A. Petersson, H. Nakatsuji, M. Hada, M. Ehara, K. Toyota, R. Fukuda, J. Hasegawa, M. Ishida, T. Nakajima, Y. Honda, O. Kitao, H. Nakai, M. Klene, X. Li, J. E. Knox, H. P. Hratchian, J. B. Cross, C.

- Adamo, J. Jaramillo, R. Gomperts, R. E. Stratmann, O. Yazyev, A. J. Austin, R. Cammi, C. Pomelli, J. W. Ochterski, P. Y. Ayala, K. Morokuma, G. A. Voth, P. Salvador, J. J. Dannenberg, V. G. Zakrzewski, S. Dapprich, A. D. Daniels, M. C. Strain, O. Farkas, D. K. Malick, A. D. Rabuck, K. Raghavachari, J. B. Foresman, J. V. Ortiz, Q. Cui, A. G. Baboul, S. Clifford, J. Cioslowski, B. B. Stefanov, G. Liu, A. Liashenko, P. Piskorz, I. Komaromi, R. L. Martin, D. J. Fox, T. Keith, M. A. Al-Laham, C. Y. Peng, A. Nanayakkara, M. Challacombe, P. M. W. Gill, B. Johnson, W. Chen, M. W. Wong, C. Gonzalez, and J. A. Pople, *Gaussian, Inc.: Wallingford CT*. **2004**.
- (178) Butler, J. N., *Ionic Equilibrium: Solubility and pH Calculations*. 1998; p 474 pp.
- (179) Bernhardt, P. V.; Moore, E. G., *Aust. J. Chem.* **2003**, *56*, 239-258.
- (180) Bernhardt, P. V.; Hayes, E. J., *Inorg. Chem.* **2002**, *41*, 2892-2902.
- (181) Moutet, J. C.; Saint-Aman, E.; Ungureanu, E. M.; Arion, V.; Gerbeleu, N.; Revenco, M., *Electrochim. Acta*. **2001**, *46*, 2733-2740.
- (182) Plenio, H.; Diodone, R., *Inorg. Chem.* **1995**, *34*, 3964-3972.
- (183) Beer, P. D.; Gale, P. A., *Angew. Chem., Int. Ed.* **2001**, *40*, 486-516.
- (184) Severin, K., *Coord. Chem. Rev.* **2003**, *245*, 3-10.
- (185) Plakhotnyk, A. V.; Ernst, L.; Schmutzler, R., *J. Fluorine Chem.* **2005**, *126*, 27-31.
- (186) Akbayeva, D. N.; Di Vaira, M.; Seniori Costantini, S.; Peruzzini, M.; Stoppioni, P., *Dalton Trans.* **2006**, 389-395.
- (187) Fernandez-Galan, R.; Manzano, B. R.; Otero, A., *J. Organomet. Chem.* **1999**, *577*, 271-282.
- (188) Fernandez-Galan, R.; Manzano, B. R.; Otero, A.; Lanfranchi, M.; Pellinghelli, M. A., *Inorg. Chem.* **1994**, *33*, 2309-2312.
- (189) White, C.; Thompson, S. J.; Maitlis, P. M., *J. Organomet. Chem.* **1977**, *134*, 319-325.
- (190) Wimmer, F. L.; Snow, M. R., *Aust. J. Chem.* **1978**, *31*, 267-278.
- (191) Miller, S. R.; Gustowski, D. A.; Chen, Z. H.; Gokel, G. W.; Echegoyen, L.; Kaifer, A. E., *Anal. Chem.* **1988**, *60*, 2021-2024.

- (192) Masiker, M. C.; Mayne, C. L.; Eyring, E. M., *Magn. Reson. Chem.* **2006**, *44*, 220-229.
- (193) Popov, K.; Lajunen, L. H. J.; Popov, A.; Ronkkomaki, H.; Hannu-Kuure, M.; Vendilo, A., *Inorg. Chem. Comm.* **2002**, *5*, 223-225.
- (194) Shamsipur, M.; Madrakian, T., *J. Coord. Chem.* **2000**, *52*, 139-149.
- (195) Suzuki, M.; Koyama, H.; Noyori, R., *Tetrahedron.* **2004**, *60*, 1571-1579.
- (196) Mueller, A.; Rehder, D.; Haupt, E. T. K.; Merca, A.; Boegge, H.; Schmidtman, M.; Heinze-Brueckner, G., *Angew. Chem., Int. Ed.* **2004**, *43*, 4466-4470.
- (197) Reich, H. J.; Borst, J. P.; Dykstra, R. R.; Green, P. D., *J. Am. Chem. Soc.* **1993**, *115*, 8728-8741.
- (198) Connors, K. A., *Binding Constants: The Measurements of Molecular Complex Stability*. 1987; p 350 pp.
- (199) James, T. L.; Noggle, J. H., *PNAS.* **1969**, *62*, 644-649.
- (200) Kratochvil, B.; Long, R., *Anal. Chem.* **1970**, *42*, 43-46.
- (201) Puchta, R.; Galle, M.; van Eikema Hommes, N.; Pasgreta, E.; van Eldik, R., *Inorg. Chem.* **2004**, *43*, 8227-8229.

Lebenslauf

Persönliche Daten

Name	David Sarauli
Geburtsdatum	01.09.1975
Geburtsort	Tiflis, Georgien
Staatsangehörigkeit	georgisch
Familienstand	verheiratet

Bildungsweg und Abschlüsse

09/1981 – 06/1992	Grund- und Oberschule in Tiflis, Georgien; Abitur Juni 1992
09/1992 – 06/1996	Bachelor Studium (Schwerpunkt Physik) an der Universität Tiflis, Georgien, mit überdurchschnittlichem Abschluss
09/1996 - 06/1998	Master Studium (Schwerpunkt Biophysik) an der Universität Tiflis, Georgien. Abschluss 1998 (Note: 1,0). Thema der Masterarbeit: <i>Hydrodynamische Untersuchung der DNS Reptation aus dem Kapsid eines C_p – Bakteriophagen</i>
09/1998 – 06/2001	Wissenschaftlicher Mitarbeiter am Institut für Molekularbiologie und Biophysik, Tiflis, Georgien.
10/2001 – 07/2002	Forschungsaufenthalt am Institut für Physikalische und Theoretische Chemie, Universität Regensburg (im Rahmen eines Jahresstipendiums vom Deutschen Akademischen Austauschdienst)

- 11/2002 – 12/2002 Gastwissenschaftler am Department Chemie und Pharmazie (Lehrstuhl für Anorganische und Analytische Chemie) bei Prof. Dr. Dr. h.c. mult. Rudi van Eldik, Universität Erlangen-Nürnberg
- seit 01/2003 Beginn der Doktorarbeit am Department Chemie und Pharmazie (Lehrstuhl für Anorganische und Analytische Chemie) bei Prof. Dr. Dr. h.c. mult. Rudi van Eldik, Universität Erlangen-Nürnberg.